Terahertz Time-Domain Spectroscopy of Poorly Soluble Pharmaceuticals

Dissertation

zur

Erlangung des Doktorgrades

der Naturwissenschaften

(Dr. rer. nat.)

dem

Fachbereich Physik

der Philipps-Universität Marburg

vorgelegt von

Jan Ornik

aus Celje

Marburg, 2023

Vom Fachbereich Physik der Philipps-Universität Marburg
als Dissertation angenommen am: 16.11.2022

Erstgutachter: Prof. Dr. Martin Koch
Zweitgutachterin: Prof. Dr. Cornelia M. Keck

Tag der mündlichen Prüfung: 19.12.2022
Hochschulkennziffer: 1180

Acknowledgments

A great part of the results presented in this work are an outcome of fruitful collaborations, in particular with the group of Prof. Cornelia M. Keck. I am grateful to all people who were directly involved in the scientific process leading to the results presented here. Their scientific contributions are acknowledged at the end of this work after the bibliography. This dissertation, however, includes only part of the work done during my doctoral time. This also means that many more people indirectly contributed to and had an influence on this work, for which I am very grateful.

I am thankful to Prof. Martin Koch for accepting me into his group and encouraging me to begin with the doctoral degree in the first place. Moreover, I am grateful for his support, guidance, and optimism combined with his enthusiasm about research and academia, which was especially relevant at times when things were not running smoothly. I thank Prof. Cornelia M. Keck for introducing the topic of poorly soluble pharmaceuticals to me and for being the second examiner of this work. I would also like to thank Prof. Martin Hofmann and Prof. Peter Lenz for agreeing to examine this work.

After joining the group of Prof. Martin Koch and in the early stage of my doctoral time, I had the pleasure of working with Prof. Jan C. Balzer, Dr. Stefan Busch, Dr. Amin Soltani, Dr. David Jahn, Dr. Stefan Sommer, Dr. Marco Reuter, Arno Rehn, and Dr. Eva-Maria Stübling. I thank them for sharing their knowledge and experience about terahertz time-domain spectroscopy, terahertz systems in the labs, and data analysis. This made things at the beginning much easier. I am grateful to Dr. Stefan Sommer and Dr. Eva-Maria Stübling for staying in touch and for being ready to help also after leaving the group.

I am also grateful to Mikhail Mikerov, Alexander Jäckel, Cornelius Mach, Srumika Konde, and Lara Heidrich, who I had the opportunity to supervise during their bachelor's and/or master's studies in the group. The symbiotic work relationship more often than not led to notable results and provided me with new valuable experience and knowledge. Remarkably they all decided to start their doctoral studies.

A special thank you to Lara Heidrich who was interested in the topic of poorly soluble pharmaceuticals and significantly contributed to this work. It was a pleasure working together. A warm thank you to Prof. Enrique Castro-Camus for his contributions to this work, for sharing his experience and knowledge, and for providing a second opinion, often with a new perspective, whenever needed.

I am grateful to Jochen Taiber, Julia Prume, Dr. Johnny Nguyen, Jan Helminiak, Fatima Taleb, Goretti Hernandez, and Caroline Sommer for contributing to the nice atmosphere in the group on the Lahnberge over the years as well as for many discussions, team-efforts, and many interesting and fun moments. The same goes for all other students who spent time in the group, guests who visited and stayed with the group, and group members at Renthof. I would like to thank Philipp Richter for the pleasant time while shortly working together on the Lahnberge and sharing valuable experience about the system alignment and for many discussions. I am thankful to Maya Strobel for her patience and help when it comes to the university bureaucracy and to Rüdiger Rink for his help with the design and fabrication of many

Marburg, October 2022   *Jan Ornik*

Table of contents

List of abbreviations

Abbreviation	Whole term
AIMD	*ab initio* molecular dynamics
APG	apigenin
API	active pharmaceutical ingredient
ASOPS	asynchronous optical sampling
ATR	attenuated total reflection
AZM	azithromycin
BCS	biopharmaceutics classification system
CAF	caffeine
CBZ	carbamazepine
CUR	curcumin
DEX	D-(+)-glucose
DFT	density functional theory
DSC	differential scanning colometry
ECOPS	electronically controlled optical sampling
EMA	European Medicines Agency
FC	fenoprofen calcium dihydrate
FDA	Food and Drug Administration
FDS	freqeuncy-domain spectroscopy
FFT	fast Fourier transform
FP	Fabry-Perot
FT-IR	Fourier-transform infrared spectroscopy
GI	gastrointestinal
HPMC	hydroxypropyl methylcellulose
HPMCAS	hydroxypropyl methylcellulose acetate succinate
HSD	hesperidin
HST	hesperetin
IBU	ibuprofen
IM	indomethacin
LTA	L-(+)-tartaric acid
MCC	microcrystalline cellulose
MGS	magnesium stearate
NAP	naproxen
NIF	nifedipine
NOR	norfloxacin
OAPM	off-axis parabolic mirror
OCT	optical coherence tomography
PAT	process analytical technology
PCA	photoconductive antenna
PEG	polyethylene glycol
PEG 4000	polyethylene glycol 4000
PVP	polyvinylpyrrolidone
QRT	quercetin
SNR	signal-to-noise ratio

SUC	D-(+)-sucrose
TDS	time-domain spectroscopy
THz	terahertz
TPI	terahertz pulsed imaging
USP	United States Pharmacopeia
VDOS	vibrational density of states
WHO	World Health Organization
XRD	x-ray diffractometry
α-LAC	α-lactose monohydrate

1 Introduction

Illnesses or other health-related problems that people experience in the course of their lives are often treated with pharmaceuticals. During the treatment drugs can be administered to patients in different ways, whereby oral administration of solid dosage forms is the most common one [1–3]. A key aspect of the oral administration is the sufficient body intake of the active pharmaceutical ingredient (API) after the administration of the drug. This requires sufficient solubility of the drug in the gastrointestinal (GI) tract. Only then the molecules can permeate into the systemic circulation and be delivered onto the site of action [4]. The majority of newly developed drugs and drug candidates are poorly soluble in aqueous media, which limits their bioavailability and therefore their potential for the patient treatment [5,6]. Therefore, different strategies are being considered and tested to improve the solubility of poorly soluble pharmaceuticals. One such strategy is to transform drugs from their stable crystalline state into the amorphous state, which results in the improved solubility [7]. A novel approach for improvement of solubility involving amorphous drugs are smartFilms®. SmartFilms are prepared by applying a solution containing an API onto a conventional paper. After the solvent evaporates, the API remains in the paper matrix of the smartFilms in its amorphous state [8,9]. However, the expected solubility advantage due to the amorphousness of the loaded drug comes at a cost of the potential instability of such formulations due to the possible recrystallization of the amorphous drug. Therefore, analytical methods are needed to inspect and monitor the solid state of an API in a formulation, preferably in a non-destructive way.

A wide variety of spectroscopic methods based on light-matter interaction exists and can be used to obtain different information about a sample under investigation. How electromagnetic waves interact with matter depends on the frequency and wavelength of the electromagnetic radiation. For example, liquid water is transparent in the visible part of the electromagnetic spectrum but strongly absorbing in the infrared region. Another example is human tissue, which is opaque for the visible light but transparent for x-rays. Terahertz (THz) refers to the part of electromagnetic spectrum ranging from 0.1 to 10 THz [10]. THz waves are non-ionizing and can penetrate through many materials, which are opaque in the optical range and highly absorbing in the IR range such as fabric, wood, ceramics, plastics, paper, and many pharmaceuticals. Besides, the wavelength of the THz waves ranges from 30 µm to 3 mm, which means that objects exceeding several mm in size can be directly investigated in the far-field. This makes spectroscopy in the THz range an attractive tool for non-destructive testing and inspection of many different materials and products including poorly soluble pharmaceuticals.

Many crystalline pharmaceuticals show distinct absorption spectra with pronounced absorption features in the THz range. The absorption spectra depend both on the molecular as well as the crystalline structure [11–14] This allows for straightforward discrimination and identification of different substances and polymorphs of the same substance [15–19]. Furthermore, since amorphous materials generally show featureless absorption spectra in the THz frequency range [20], THz spectroscopy has the potential for the detection and quantification of potential crystalline components in the amorphous pharmaceutical formulations. The focus of this work lies on exploiting and exploring the

1

potential of THz time-domain spectroscopy (TDS) for the inspection of the solid state of APIs loaded into smartFilms® and of tablets made from them. In the remaining part of this introduction the structure of this work with a brief overview of the individual chapters is provided.

In chapter 2 the basics of THz spectroscopy are discussed. In the first section the principle of operation of THz TDS systems based on photoconductive antennas (PCAs) is presented. This includes signal acquisition and processing, and investigation of samples in transmission and reflection geometry. The evaluation of THz TDS transmission measurements is discussed in more detail since the results presented in this work were obtained in the transmission mode. In the second section of this chapter the pharmaceutical applications of THz TDS are presented. These are subdivided into the investigation of the solid state of the APIs, of tablet coatings, and of tablet porosity.

Chapter 3 focuses on the solubility and bioavailability of pharmaceuticals. First the problem of poorly soluble pharmaceuticals for the pharmaceutical industry is elaborated. This is followed by the description of dissolution, solubility and absorption, and dissolution rate, which are important concepts affecting the bioavailability of the drugs. In the final section of this chapter an overview of solubility improvement strategies with the focus on solid-state engineering, solid dispersions, and smartFilms is provided.

The first results involving THz TDS of smartFilms and tablets made from them are discussed in chapter 4. This proof of principle study focuses on the applicability of THz TDS for the inspection the solid state of APIs in smartFilms. SmartFilms containing different amounts of L-(+)-tartaric acid (LTA) were prepared and analyzed to evaluate the extent to which smartFilms can maintain LTA amorphous. The results of the preliminary investigation are presented in the first section of this chapter. In the second section the results of the main investigation are presented.

To further explore the applicability of THz TDS for the investigation of poorly soluble pharmaceuticals, a set of samples including crystalline APIs and excipients were investigated. Their absorption coefficients are presented in chapter 5. The key aspect of this chapter is to identify pharmaceuticals with pronounced absorption features. Pronounced absorption features are crucial for the identification of crystalline pharmaceuticals. Furthermore, properties of the identified absorption peaks in terms of their amplitude, frequency position and width were extracted and compared in the final section of this chapter. The extraction of peak parameters is important for the quantification of crystallinity of APIs in the samples.

Indomethacin (IM), a poorly soluble API, was selected as a model drug for the study focusing on the assessment of crystallinity and amorphousness of APIs in tablets made from smartFilms. In the first section of chapter 6 the analysis of two IM polymorphs and amorphous IM is presented. In the second section, a novel approach for quantification of crystallinity of IM based on the analysis of THz absorption spectra of tablets made from smartFilms and physical mixtures with different IM content is presented.

Chapter 7 focuses on the investigation of nifedipine (NIF) dispersed in a cellulose matrix. NIF is also a poorly soluble API. In the first section of this chapter the preparation and investigation of NIF samples including crystalline and amorphous NIF as well as physical

mixtures of crystalline NIF and cellulose are presented. The investigation of conventional smartFilms containing NIF and modified smartFilms containing an additional carrier and NIF is discussed in the second section. Based on the THz TDS investigation of the samples the ability of the two sample types to maintain NIF amorphous is compared. In the final section of this chapter the investigation of samples prepared by loading NIF directly into the tablets made from cellulose is discussed.

Chapter 8 contains a summary of the work and provides an outlook about the open questions, challenges, and possibilities of THz TDS of poorly soluble pharmaceuticals that remain to be addressed in the future. A German version of the summary is provided in chapter 9.

2   Terahertz spectroscopy

The term THz spectroscopy refers to spectroscopic investigations in the so-called THz range of the electromagnetic spectrum. Similarly, terms such as THz radiation or THz waves refer to the electromagnetic radiation in the THz range, which lies between the microwave and infrared range and is loosely defined as the frequency range between 0.1 and 10 THz [10]. This frequency range corresponds to the wavelength range of 3 mm to 30 µm and the wavenumber range between 3.33 and 333 cm^{-1}. The corresponding photon energy of the THz radiation lies between 0.4 and 40 meV, which makes THz radiation non-ionizing.

The existence of THz science and technology as a sort of a distinct scientific field and community has its historical reasons. Until the 1980s efficient way of generation and detection of the THz radiation did not exist, since the electronic as well as photonic devices face technical and physical limitations in this range, which led to the so called THz gap [21]. In the end of 1980s this gap was successfully filled by combining femtosecond-lasers and photoconductive switches at the Bell labs [22]. This enabled the development of THz TDS, which was first applied for spectroscopic investigation of water vapor [23]. Throughout the historical development, different names were also in use such as the far-infrared referring to the THz range as well as T-rays referring to the THz waves.

There are several different ways to generate THz radiation. For example, depending on the temperature of a black body, a certain part of its radiation is emitted in the THz range. On the one hand, this can be used in some Fourier transform infrared spectroscopy (FT-IR) systems to probe samples also in the THz range. On the other hand, depending on the type of detection scheme, potential thermal background radiation can also interfere with the measurement. Nevertheless, when discussing THz generation, ways different from black body radiation are typically considered. These can be divided into four groups: free electron vacuum devices (e.g., free electron lasers, gyrotrons), solid-state electron devices (e.g., Gunn diodes, frequency multipliers), lasers (e.g., quantum cascade lasers), and laser driven THz emitters (e.g., photoconductive switches or antennas) [21,24]. Free electron vacuum devices can generate high power (> kW) THz radiation, however, this comes at a price of a large size [25] and costs or operation typically limited to the lower THz range (< 1 THz) [26]. Modern solid-state electron devices are pure electronic sources, which can operate at a single frequency or cover a broader band of frequencies. Frequencies as high as 3 THz can be reached by frequency multipliers [27]. THz lasers cover a part of the THz spectrum only at discrete frequencies. First developed THz lasers were gas lasers typically pumped with a CO_2 laser [28]. Recently the development of quantum cascade lasers gained a lot of attention with the focus on increasing their temperature of operation towards room temperature [24]. The principle of operation of laser driven THz emitters is the frequency down-conversion of the laser light to the THz range. This down-conversion can be achieved from femtosecond-laser pulses by optical rectification in non-linear crystals (e.g., $LiNbO_3$) or by using photoconductive switches [29]. In both cases the femtosecond-laser pulses are converted into narrow THz pulses in the time domain corresponding to a broad THz emission spectrum ranging from 0.1 THz and exceeding 4 THz [30] or even 30 THz [31,32].

THz spectroscopy can be further classified into two types: time-domain spectroscopy (TDS) and frequency-domain spectroscopy (FDS). In the former case, which is discussed in more detail in the following section, the signal is recorded in the time domain and can be subsequently transformed into the frequency domain by performing the discrete Fourier transformation. In the latter case, also known as continuous wave spectroscopy, PCAs are driven by two lasers both emitting continuously at a single, but different frequency. If the frequency difference lies in the THz range, a monochromatic THz radiation at this difference frequency is generated. This process is often referred to as photomixing and the antennas used as photomixers [33,34]. By tuning the frequency of one of the two lasers and using a second photomixer for the signal detection, the THz-radiation can be coherently detected directly in the frequency domain. Modern photomixing setups work in a broad part of the THz spectrum typically ranging from 0.05 to 3 THz with a high frequency resolution (<5MHz) [35]. Finally, both approaches, TDS and FDS can be realized using PCAs, which typically generate THz radiation with power ranging from few µW up to approximately 100 µW [36]. Such low power of the emitted THz radiation means that the heating of the sample or the environment during system operation is of no concern. Furthermore, modern systems based on PCAs can be fully fiber-coupled and achieve over 90 dB dynamic range [30]. The use of fully fiber-coupled systems simplifies compliance with laser-safety regulations. Furthermore, considering the non-ionizing nature of the THz radiation and the low power of the emitted radiation, THz spectroscopy is an attractive tool for safe and non-destructive applications.

In this work, all THz measurements were performed using THz TDS systems employing femtosecond lasers and PCAs. In the following section the principle of operation of THz TDS as well as signal processing and evaluation of the acquired time-domain data is explained in more detail. This is followed by an overview of THz TDS applications in the pharmaceutical field.

2.1 Terahertz time-domain spectroscopy

At the beginning of this section the principle of operation of THz TDS systems based on using photoconductive antennas is presented. This is followed by a subsection focusing on signal acquisition, its processing and quality. In the subsequent subsections transmission and reflection measurements and their evaluation are discussed in more detail.

A sketch of an emitter PCA consisting of a spherical lens attached to a photoconductive substrate with a metallized dipole antenna structure on its surface is shown in Figure 1. In the case of an emitter antenna, a bias voltage is applied to the antenna structure and a femtosecond laser beam is focused onto the antenna gap. Once a femtosecond optical pulse (pulse duration shorter than 1 ps) with sufficient photon energy is absorbed by the photoconductive material, the short-lived charge carriers (i.e., electrons and holes) are generated and accelerated by the applied bias field. At first, the moving charge carriers give a quick rise to the photocurrent. After a short while, the charge carriers recombine, due to their short lifetime in the sub-picosecond range [37], which causes a decrease in the photocurrent. This leads to an emission of a pulse-shaped electromagnetic radiation from the emitter antenna, which is proportional to the time derivative of the induced photocurrent [29]. The silicon lens facilitates outcoupling and collimation of the generated

THz radiation [38]. The polarization of the emitted THz radiation depends strongly on the antenna structure in use. In the case of commonly used strip-line or dipole antenna structures, which were also used for measurements presented later in this work, the emitted THz radiation is strongly linearly polarized [39].
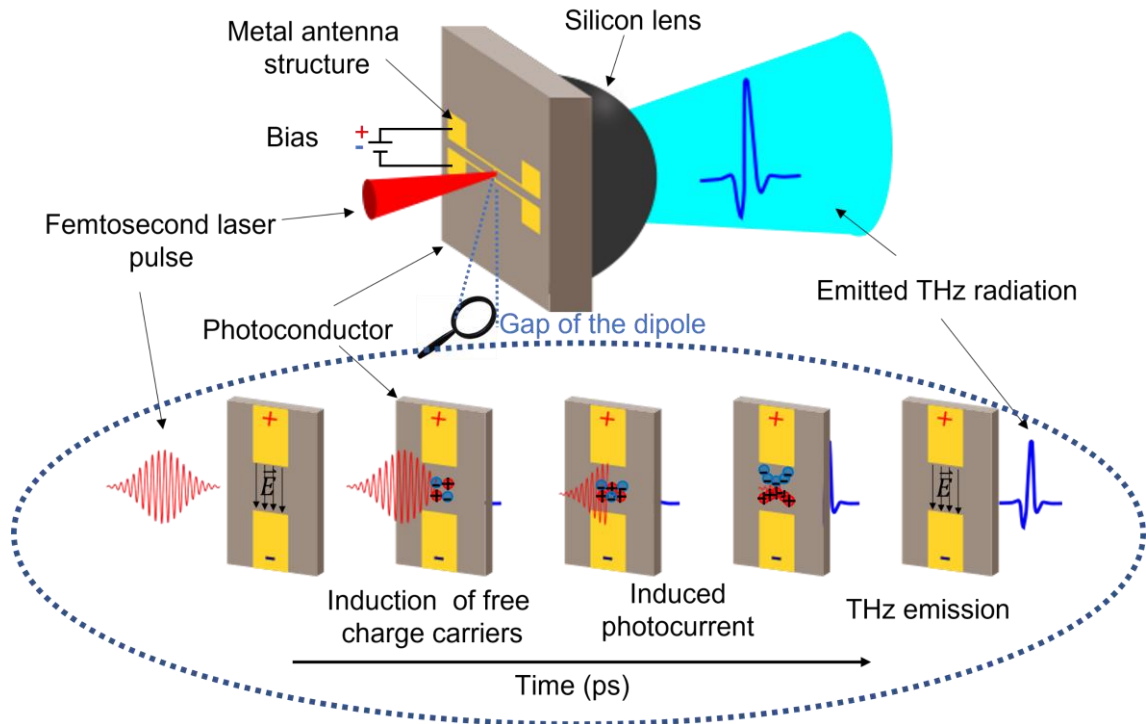
Figure 1. Sketch of a photoconductive emitter antenna consisting of a photoconductive substrate, metallized antenna structure, and a truncated spherical lens typically made from high resistivity silicon. In the bottom part of the sketch the process of THz generation in the gap of the antenna structure is schematically depicted. The femtosecond laser pulse propagates into the photoconductor and gets absorbed which leads to generation of the broadband pulse-shaped THz radiation. Note that the depicted movement and distribution of the induced charge carriers between the electrodes is simplified in this figure. More information about the charge carrier dynamics can be found in [40–42].

For the detection of THz radiation, another PCA acting as a detector can be used in a combination with an emitter PCA, a femtosecond laser, and a delay line as shown in a schematic of a THz TDS system in Figure 2: The laser beam first passes a beam splitter where it is split into two parts of an equal intensity. One part is guided using mirrors to the emitter antenna where a lens is used to focus the beam onto the gap of the antenna. After the femtosecond laser pulse reaches the emitter antenna, the pulse-shaped THz radiation is emitted as described above and guided by a set of 4 off-axis parabolic mirrors (OAPMs) towards the detector. The first OAPM collimates the THz beam, then a pair of OAPMs is used to focus and again collimate the THz beam. The last OAPM focuses the THz beam onto the detector antenna. Alternatively, the THz beam can be guided in a similar manner using lenses as shown in the inset of Figure 2.

The other part of the laser beam is guided to the detector antenna over a mechanical delay line and focused onto the gap of the detector antenna. Once the femtosecond pulse reaches the detector antenna the short-lived charge carriers are also induced and

the antenna becomes conductive for a short time (i.e., much shorter than the duration of the THz pulse). Instead of applying external voltage to the contacts of the detector antenna, a current flowing through the antenna is measured. If the THz beam is polarized across the gap of the detector antenna, a transient voltage proportional to the electric field of the THz pulse is induced across the antenna dipole. Now, if a part of the incident THz pulse reaches the receiver antenna when it is still conductive, an electric current proportional to the electric field of that part of the THz pulse is induced. By moving the optical delay line, the time when the femtosecond laser pulse reaches the detector (i.e., the time when the detector is conductive) with respect to the incident THz pulse can be changed. This way a time-dependent THz waveform can be obtained by measuring the electric current induced in the detector antenna with respect to the position of the delay line, which can be easily converted into the time delay. Such a coherent detection scheme leads to a high signal-to-noise ratio since the effects of THz radiation originating from different sources than the emitter antenna (e.g., black body radiation) are strongly reduced [43].
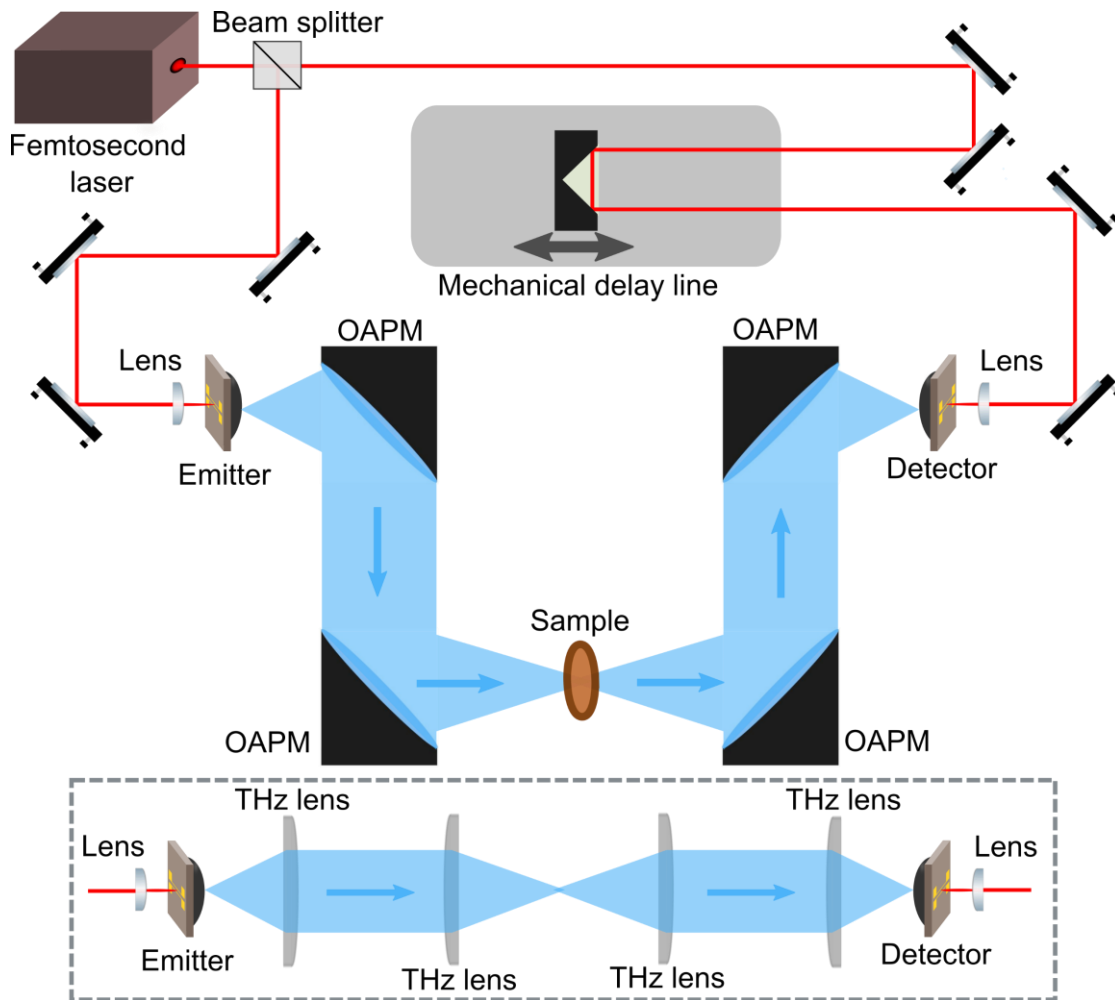
Figure 2. A sketch of a THz TDS free-space setup based on PCAs and a mechanical delay line. The four OAPMs are used to guide the beam from the emitter to the detector. The sample is typically inserted into the focal plane between the second and third OAPM. Alternatively, THz lenses can be used to form the THz beam path as shown in the inset. By omitting the second and third THz lens, a collimated setup without an intermediate focus can be obtained. Similar can be achieved by using only two OAPMs [44,45].

Observing the sample shown in the THz beam path in Figure 2 an important concept of THz imaging by raster scanning a sample can be introduced. Raster imaging is performed by placing a sample in the focal plane and moving it within the focal plane. The THz signal is recorded for chosen positions of the sample. Since the THz beam is focused, it propagates only through a small part of the sample and the recorded signal contains information only about that small, illuminated area of the sample. The size of the probed area within a single measurement depends on the beam size in the focal plane, which inherently limits the imaging resolution. By extracting a value of interest (e.g., intensity of transmitted radiation at a certain frequency) from the recorded THz signals for all measured positions on the sample, a so-called false color image of a sample is achieved, which reveals spatially distributed information about the sample. In a similar manner, imaging can be performed in a reflection geometry.

The principle of operation of THz TDS system was explained exemplarily for a so-called free-space setup (see Figure 2). Such a setup is typically built on an optical table in a lab environment while considering the laser safety requirements. The presented concept employing a mechanical delay line stayed mostly unchanged since the first demonstration [23] and is still in use. Nevertheless, since the first demonstration, great progress in the development of THz TDS has been made. For example, systems based on asynchronous optical sampling (ASOPS) [46] or on electronically controlled optical sampling (ECOPS) [47] have been developed. Such systems do not require a mechanical delay line, which enables higher acquisition rates. Another example, is the development and optimization of new photoconductive materials for PCA [37,48,49] in combination with fiber lasers used also in the telecommunication industry. This improved the performance of the systems as well as reduced their price and size. Furthermore, development of fiber-coupled PCA modules omitted the need for the laser light to propagate to the antennas through free space. This led to the development of commercially available, compact, and transportable fiber-coupled THz TDS systems [30,47], which can be easily used also outside of a laboratory environment. Despite many variations in technical construction of different THz TDS systems, they all have in common that the sampling of the signal is performed in the time domain. This also means, that the same data processing and the same algorithms to extract the sample properties can be applied to all of them. Furthermore, the system performance can be compared based on the recorded signal quality.

In the next subsection typical parameters of signal acquisition, its transformation into the frequency domain and ways to quantify the system performance are discussed. This is followed by subsections describing principles of sample characterization in reflection and transmission geometry.

2.1.1 Signal acquisition, processing, and quality

Most used THz TDS systems employ a mechanical delay line. For such systems, a typical time-domain measurement is performed by moving the delay line continuously at a constant speed and the signal is recorded at equidistant points until the desired time window is scanned, which typically ranges from several 10 ps and up to a few 100 ps. The maximum time range is limited by the length (L) of the mechanical delay line as $c/2L$, where c is speed of light. The time it takes to perform a single time-domain measurement is system dependent and increases with the length of the measured time

window. Typical acquisition times, therefore, vary based on the chosen settings. The chosen settings also influence the quality and usefulness of the recorded signal. When high signal quality in terms of signal-to-noise ratio (SNR) and dynamic range is preferred, typically longer acquisition times are required due to a more extensive averaging of the recorded signal. This reduces the effect of random noise on the recorded signal as it will be shown later in this subsection. Depending on the system and selected settings, the acquisition times range from below 100 ms to up to a few minutes per single recorded time-domain signal.

The evaluation of the recorded signals is commonly performed in the frequency domain. This requires conversion of the recorded time-domain signal ($E(t)$) into the frequency domain by means of Fourier-Transformation, typically by using a fast Fourier transform (FFT) algorithm ($\tilde{E}(v) = \mathrm{FFT}(E(t))$). The result of the transformation is the complex spectrum ($\tilde{E}(v)$), which can be separated into amplitude ($\left|\tilde{E}(v)\right|$) and phase ($\varphi(v)$) parts according to the polar form of a complex number as:

$$\tilde{E}(v) = \left|\tilde{E}(v)\right|e^{i\varphi(v)}\,, \hspace{4cm} 2.1$$

where v is the frequency. The resulting frequency resolution (Δv) depends on the length of the time-domain signal (T) as $\Delta v = 1/T$ and the maximum resolvable frequency (v_{max}, i.e., Nyquist frequency) depends on the time spacing (Δt_{sam}) between the recorded signal values in the time domain as $v_{max} = 1/(2\Delta t_{sam})$. By increasing the length of the recorded time-domain signal, the frequency resolution can be increased. Similarly, by increasing the sampling frequency ($v_{sam} = 1/\Delta t_{sam}$, i.e., by reducing the time spacing (Δt_{sam}) between the recorded values), the maximum frequency, which can be resolved, is also increased. However, in reality the frequency resolution of the converted signals cannot be arbitrarily increased by simply increasing the length of the measured time-domain signal. The reason for this is that the amplitude of the signal reduces after the main pulse and the value of the SNR approaches value of one [50,51]. Furthermore, the useful frequency range of a typical THz TDS system based on PCAs, in which the recorded signal exceeds the noise, is limited as presented later in this subsection (see Figure 4). This means that for higher frequencies no signal and only noise is detected, even though potential signal at these higher frequencies can be resolved according to the chosen sampling frequency of the time-domain measurement. Finally, the time-domain data is often additionally processed in terms of correcting signal offset, windowing and zero-padding the signal before performing the FFT, which affects the result of the transformation into the frequency domain. An example of such processing of the time-domain data is shown in Figure 3.
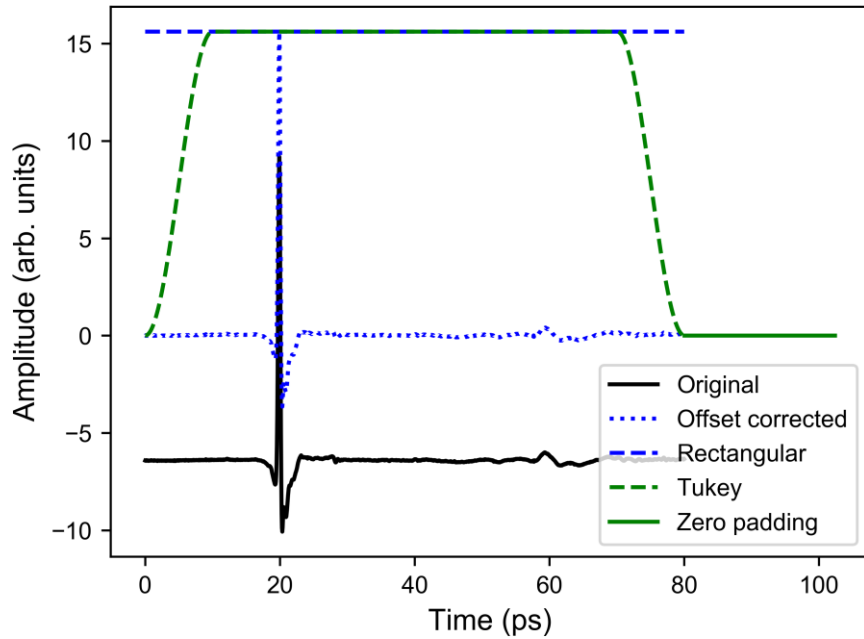
Figure 3. Time-domain signal (i.e., measured amplitude as a function of the delay time) recorded without any post-measurement data processing (original). The signal offset correction was performed by subtracting the mean value of the first 3 ps of the original signal (offset corrected). Rectangular and Tukey ($\alpha = 0.25$) windows are shown as two windowing function examples. Zero padding of the signal is shown as signal extension with zero values. The values of the two window functions were scaled to the maximum value of the signal for clearer representation. The original signal length is 200 ps. Here only the first 80 ps are shown for clarity. The measurement was performed under nitrogen atmosphere without a sample in the beam path.

Correcting the offset of a THz time-domain signal can be described as vertically shifting the whole signal (see Figure 3), which means that the DC component of the signal is changed. Considering the way THz radiation is generated and detected using PCAs, no electric current should be detected (i.e., the signal should equal to zero) before the arrival of the THz pulse. Therefore, offset is often corrected by subtracting the mean value of the first part of the signal prior to the first THz pulse. This step is also necessary before performing zero padding or windowing to avoid inducing artefacts when transforming the signal into the frequency domain.

Windowing of the time-domain data cannot be avoided due to the finite length of the acquired THz time-domain signals. This means that without applying any specific windowing function to the acquired time-domain signal is equivalent to applying a rectangular window. Applying a rectangular window basically means multiplying the time-domain signal with a constant function of unity (i.e., with a vector of the same length as the signal with all values equal to one). An important consequence of transforming finite time-domain signals into the frequency domain is spectral leakage [52]. There are many different, well-defined and broadly used windowing functions in signal processing [52], which affect the spectral leakage and have a different effect on the transformation of the signal into the frequency domain. Furthermore, they can also affect the frequency position and amplitude of the observed spectral features [53].

Zero padding of a THz time-domain signal can be understood as extending the signal by adding zero values at the beginning or the end of the original signal. This way the length of the signal is extended, which increases the apparent frequency resolution of the transformed data. However, this increase of the frequency resolution can be understood as mere interpolation of the signal in the frequency-domain. One further reason why to perform zero padding is, that some FFT algorithms are more time-efficient if the signal length (i.e., number of values the measured signal consists of) equals two to the power of a natural number (e.g., 32, 64, 1024). Zero padding might sometimes be useful, if problems are encountered when unwrapping the phase of the signal in the frequency domain. The phase unwrapping is discussed in the next subsection.

In Figure 4 the amplitude spectrum corresponding to the offset corrected time-domain signal is shown in Figure 3 (no zero padding, rectangular window). The signal amplitude is highest in the low THz region (i.e., between 0.25 THz and 0.7 THz). Towards higher frequencies the amplitude gradually rolls off and reaches the noise floor at around 4 THz. For frequencies lower than 0.25 THz the amplitude also strongly decreases. Such spectral shape is characteristic for signals acquired using THz TDS based on PCAs. The useful spectral range or bandwidth of a system, which ranges in this case approximately from 0.2 THz and exceeds 4 THz, is an important characteristic of the system performance. Another important characteristic of a system is its dynamic range. It describes the maximum signal change, which can still be quantified [54]. It is defined as the ratio between the maximum signal amplitude and root-mean-square of the noise floor. Since the noise floor is frequency independent [55,56], the dynamic range can be evaluated directly from a single reference measurement (i.e., no sample in the beam path for transmission geometry). Since the amplitude is strongly frequency dependent, this also means that the dynamic range of the system is frequency dependent. Nevertheless, it is common practice in the THz community to report the dynamic range of a system as a single value in terms of the maximum dynamic range (i.e., peak dynamic range) [51]. For the system used to perform the measurement shown in Figure 4 the peak dynamic range of the measured amplitude exceeds two orders of magnitude. It is important to note that the dynamic range of a system is often reported in terms of spectral power and not amplitude. There is a simple relation between the two since the power of the electromagnetic radiation is proportional to the square of its amplitude and the same holds for the dynamic range. This means that dynamic range shown in Figure 4 would exceed 4 orders of magnitude considering the power spectrum. The dynamic range is also often reported in dB [30]. In the case of data presented in Figure 4, the dynamic range would exceed 20 dB and 40 dB in terms of amplitude and power, respectively.

Another important characteristic of a THz TDS system is its SNR. SNR denotes the minimum signal change, which can still be detected by the system [54] and as such it limits the uncertainty of determined absorption of the investigated sample. The SNR is defined as the ration between the mean amplitude and standard deviation of the amplitude. Therefore, SNR cannot be determined from a single measurement as in the case of dynamic range. SNR calculated from ten measurement repetitions is shown in Figure 5.
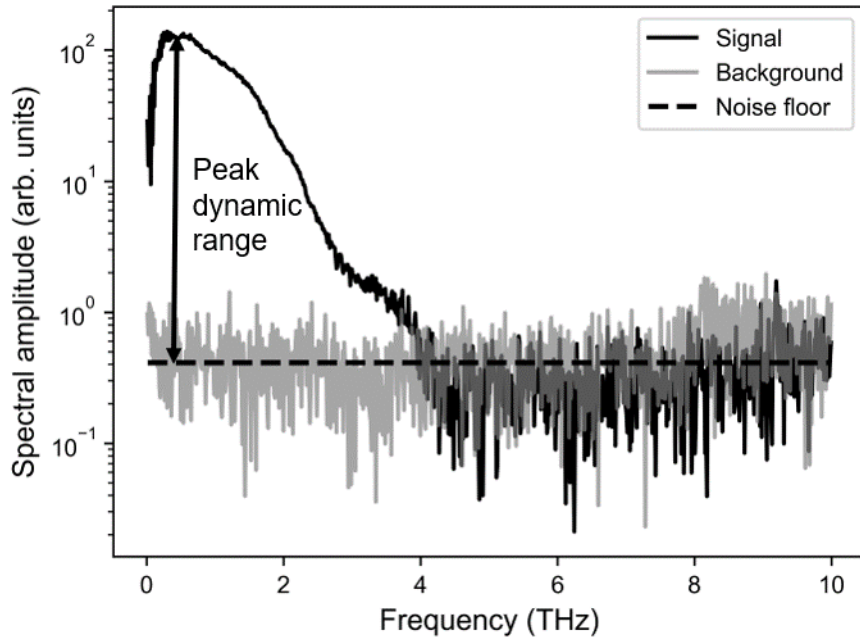
Figure 4. Amplitude spectrum of a single recorded signal. The background measurement was recorded by blocking the THz beam path with a metal object. The noise floor was determined as the root-mean-square (rms) value of the amplitude at frequencies higher than 5 THz. The signals were offset-corrected before the FFT (see offset corrected signal in Figure 3). The measurements were performed under nitrogen atmosphere.
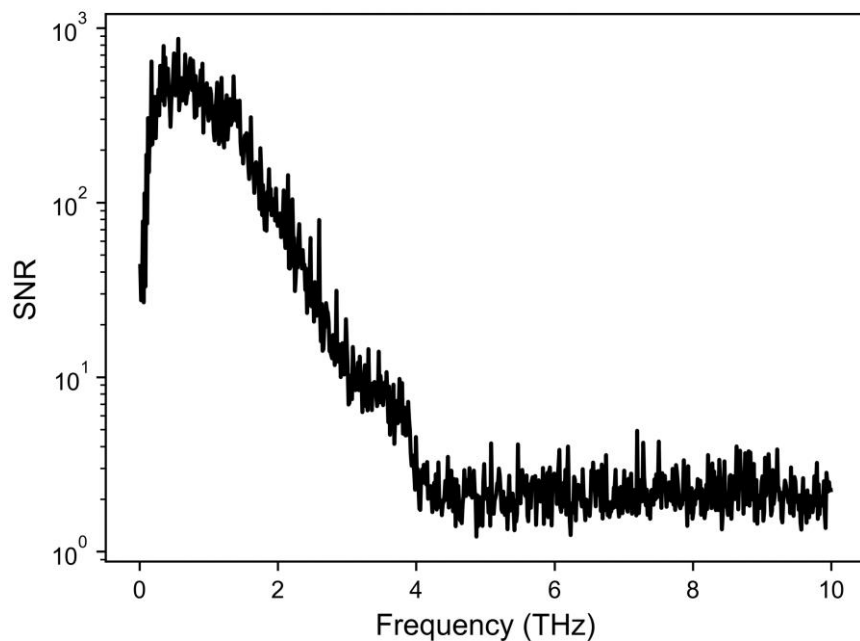
Figure 5.The signal-to-noise ratio (SNR) calculated out of ten repeated single measurements as mean amplitude divided by the standard deviation of the amplitude.

SNR is also frequency dependent and can vary substantially between neighboring frequencies. Like the dynamic range, SNR reduces with increasing frequency and reaches values close to one for frequencies for which the noise floor in the amplitude

spectrum (Figure 4) could be observed. This is expected since for these frequencies only noise is acquired. Despite the values and frequency dependency of SNR in the shown example seem similar to the dynamic range values and its frequency dependency, they can, in general, substantially vary and should therefore not be confused [54]. It is also important to note, that the SNR and dynamic range of the system depend on settings chosen in the time domain in terms of window length and averaging as shown in Figure 6.
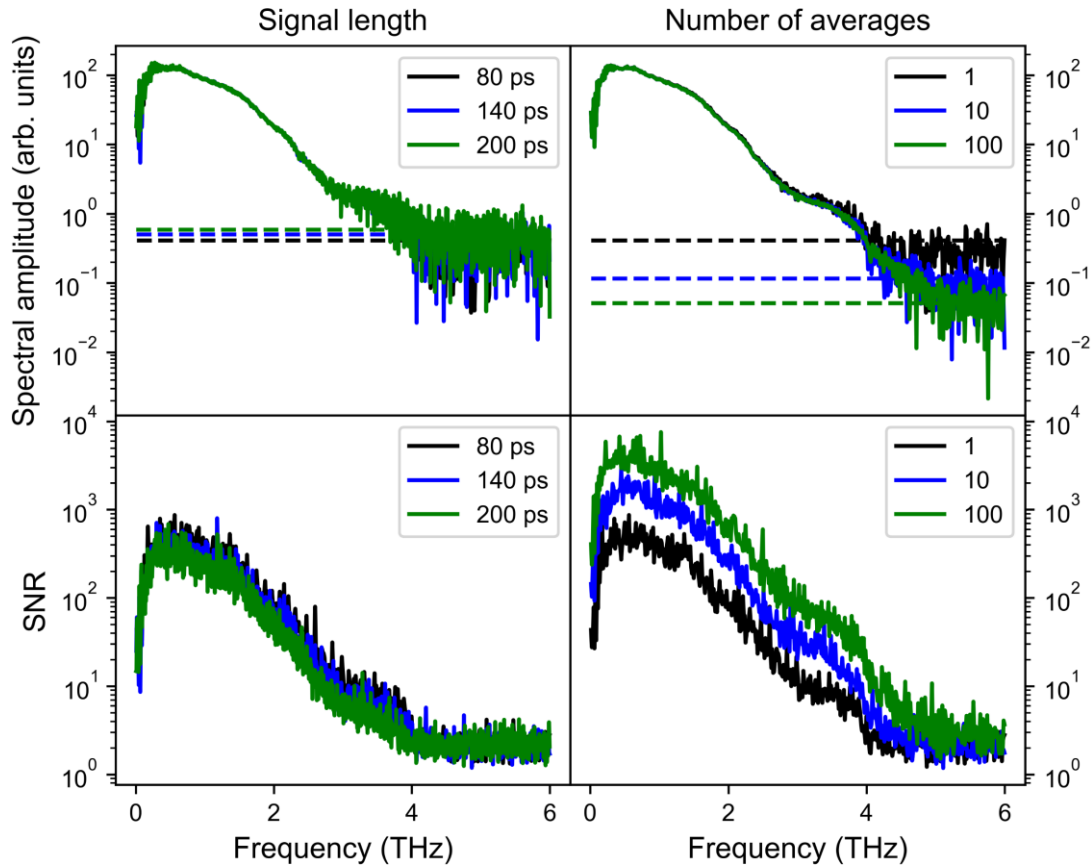
Figure 6. The effect of signal length (left half) and signal averaging (right half) on the dynamic range (upper half) and SNR (lower half) of the recorded signals. Signal lengths of 80 ps, 140 ps, and 200 ps were considered to demonstrate the effect of window length. To demonstrate the effect of signal averaging, a single measurement, a ten-times averaged signal, and a 100-times averaged signal are shown. The SNR was calculated from ten measurement repetitions. The effect of signal length is shown for single measurements (number of averages was one). For the effect of signal averaging an 80 ps signal length was chosen.

Increasing the number of times, the time-domain signal is recorded and averaged reduces the effect of random noise sampled in the signal, which can be observed as lowering the amplitude of the noise floor in the spectrum. Similarly, the SNR increases with averaging. Signal averaging is commonly employed when using relatively fast systems, which can acquire more than a single waveform per second. However, the measurement time is proportionally extended with the number of averages.

The effect of window length is somewhat different. With increasing window length, the noise floor increases and thus the SNR decreases. Therefore, it is important to provide

14

all relevant sampling parameters when providing values of the dynamic range and SNR for correct comparison of the system performance.

To summarize this subsection, the system performance can be expressed in terms of acquisition time, maximum acquisition range (i.e., length of the time domain data), useful spectral range or bandwidth, dynamic range, and SNR. Furthermore, the dynamic range and SNR are commonly presented and reported in the frequency domain. This requires transformation of the recorded time-domain signal into the frequency domain by means of FFT. The time-domain signals can be further processed before the transformation (e.g., offset correction, windowing, and zero padding). Furthermore, averaging and even selection of signal length can affect the SNR and the dynamic range of the system. With all this in mind, the concept of measurements and sample properties evaluation in the transmission geometry is discussed in more detail.

2.1.2 Transmission geometry

Sample characterization using THz TDS is commonly performed in the transmission geometry. For successful characterization, proper preparation of samples before the measurement must be considered. One crucial parameter is the sample thickness through which the radiation propagates. If the sample is made too thick, it might completely attenuate the propagating radiation, which means that no signal (i.e., only noise) is detected, and the sample characterization cannot be performed. However, if the sample is made too thin, the effect of the sample on the recorded signal might be undetectable. Typically, sample thickness ranges from few 100 µm to few mm. It is also important to consider the shape of the sample. Usually, a biplanar sample is considered. Furthermore, when characterizing a sample, it is typically assumed that the illuminated part of the sample is homogenous. In the case of anisotropic samples, one must consider that sample properties depend on the sample orientation with respect to the polarization of the THz radiation. THz radiation incident under zero-degree angle (normal incidence) on a dielectric sample of biplanar shape is schematically presented in Figure 7.
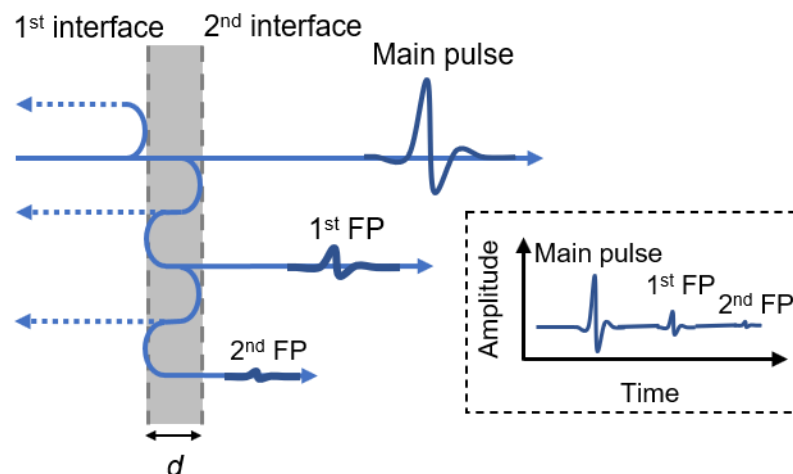

Figure 7. Schematic representation of THz radiation propagating from left to right through a biplanar single-layered sample. The reflected radiation (dashed arrows) is not detected. The inset shows a signal consisting of the main and two Fabry-Perot (FP) pulses corresponding to the schematic of the radiation propagation through the sample.

At the first interface (air-sample), part of the incident THz radiation is reflected towards the emitter and part of the radiation is transmitted into the sample. The proportions of the reflected and emitted radiation are described by the Fresnel coefficients. In the case of a moderately absorbing sample, the radiation transmitted into the sample is partially absorbed during the propagation through the sample. When it reaches the second interface (sample-air) a part of the radiation is again reflected and a part is transmitted towards the detector, where the corresponding signal is recorded. The reflected part propagates again through the sample until it reaches the first interface (sample-air), where it is again partially reflected and transmitted. The reflected part then propagates again through the sample towards the second interface (sample-air) where the transmitted part continues towards the detector and the reflected part propagates again through the sample. This continues until the radiation "bouncing back and forth" within the sample diminishes due to the transmission "losses" on every interface and absorption within the sample. This bouncing of the radiation within the sample results in additional pulses appearing after the main pulse in the time-domain signal of a sample measurement as schematically shown in the inset of Figure 7. These pulses are often referred to as Fabry-Perot (FP) pulses or peaks.

In the following, the basic concept of THz TDS data evaluation will be discussed on an example of a silicon wafer with resistivity greater than 1000 Ωcm used as a sample. First the data analysis in the time domain is presented. This is followed by a more comprehensive description of the analysis in the frequency domain.

Time-domain analysis

The time-domain signal obtained from a silicon wafer measured in transmission geometry is shown in Figure 8. Silicon is often considered to be non-absorbing in the THz region with a relatively high refractive index of 3.42 [51,57]. Due to these properties, multiple pronounced FP pulses can be clearly observed in the time-domain data. Therefore, silicon is a material of choice to demonstrate the potential use and effect of FP pulses on the evaluation of the data acquired with THz TDS in the transmission geometry.

In Figure 8 a reference measurement and a measurement of an approximately 530 μm thick silicon wafer are shown. The reference measurement was performed without the wafer in the beam path. This means that air was considered as a reference material, which is the most common practice for THz transmission measurements. It is typically considered that the refractive index of air equals unity and that it is non-absorbing (i.e., imaginary part of refractive index or extinction coefficient equals zero). Furthermore, the two measurements were performed under nitrogen atmosphere to suppress the absorption of water vapor present in ambient air [23], which can make spectroscopic investigation troublesome. The nitrogen atmosphere is achieved by placing the THz beam path inside a box into which nitrogen is pumped until the ambient air is replaced. Alternatively, the air can be dehumidified, or sometimes measurements are performed in vacuum. Furthermore, numerical approaches for post-measurement removal of the water vapor effects on the measured signals exist [58,59]. However, removal of water vapor from the air before performing the measurement is still preferred, especially in the lab environment.
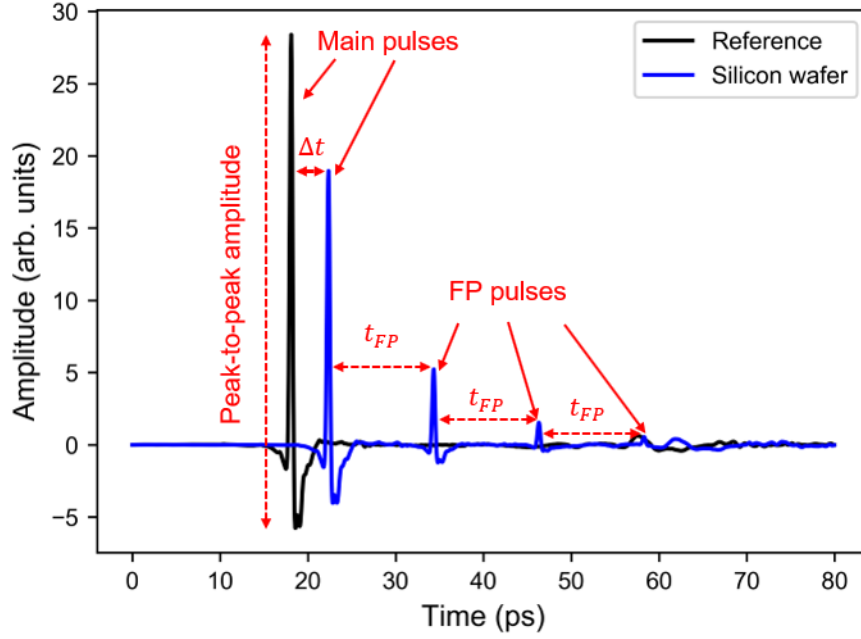
Figure 8. Time-domain signal of the reference and sample (silicon wafer) measurement. Note that the main pulse of the sample measurement is delayed (Δt) with respect to the main pulse of the reference measurement. Three additional FP pulses can be clearly resolved from the sample measurement. The first FP pulse is delayed (t_{FP}) with respect to the main pulse. All subsequent FP pulses are additionally delayed for the same time (t_{FP}) with respect to the previous.

For both, sample and reference measurement, the main THz pulse can be easily identified. In the case of the reference measurement, it arrives earlier in time compared to the sample measurement since it takes longer for the radiation to propagate through the sample due to the lower propagation speed of light in the sample, which is associated with the refractive index of the sample. This means, that by knowing the sample thickness (d), the dielectric properties of the reference material (i.e., air) and by determining the time difference between the time-of-arrival of the sample and reference main THz pulse (Δt, see Figure 8), the refractive index (n) of the sample can be calculated according to the following expression:

$$n = 1 + \frac{c\,\Delta t}{d},$$
2.2

Where c is speed of light and the refractive index of reference material (i.e., air) is one. Accordingly, the calculation of the refractive index of the silicon wafer from the measurement shown in Figure 8 and the measurement of the thickness (d) results in value of 3.42 which agrees with the value reported in the literature [51,57].

The FP pulses observed in the measurement correspond to the multiple propagation through the sample as discussed earlier. The first FP pulse corresponds to the radiation travelling through the sample two additional times compared to the main pulse in the sample measurement. Consequently, the time-of-arrival of the first FP pulse with respect to the main pulse (t_{FP}), corresponds to the round-trip of the radiation in the sample and can be written as:

$$t_{FP} = \frac{2nd}{c}. \qquad\qquad 2.3$$

Having two linear equations (2.2, 2.3) allows us to calculate the refractive index of the sample even if the thickness of the sample is unknown. Expressing d from equation 2.3 and inserting it into equation 2.2 leads to the following expression for the refractive index of the investigated samples:

$$n = \frac{t_{FP}}{t_{FP} - 2\Delta t}. \qquad\qquad 2.4$$

Calculating the refractive index according to Evaluating equation 2.4 results in a refractive index value of 3.43, which slightly exceeds the value of 3.42 reported in the literature [51,57]. The deviation from the literature values can be assigned to the limited resolution of the time-domain data. Furthermore, according to the two equations (2.2, 2.3) also the thickness of the sample can be extracted as:

$$d = \left(\frac{t_{FP}}{2} - \Delta t\right) c. \qquad\qquad 2.5$$

According to the THz measurement, the thickness of the sample is 525 µm, which is 2 µm less than the thickness measured with a micrometer screw gauge.

The amount of transmitted radiation through the sample can be evaluated from the time-domain data as well. This is done by comparing the amplitude of the main THz pulses of the reference measurement with the amplitude of the main THz pulse of the sample measurement. The amplitude of a pulse is typically calculated as the maximum value of the pulse or the difference between the maximum and minimum value of the pulse. The latter is often referred to as the peak-to-peak amplitude. In transmission geometry, this can be easily done by determining the maximum (and minimum) value of the whole time-domain trace since the main pulse has the highest amplitude. For the silicon wafer (Figure 8), the quotient between the two amplitudes equals 0.673, which means that the amplitude of the transmitted radiation is approximately 67 % of the initial amplitude. Furthermore, by considering the intensity of transmitted radiation instead of amplitude the transmittance of the sample can be evaluated. Transmittance of a sample is defined as the quotient between the intensity of the radiation transmitted by the sample and the intensity of the incident (i.e., reference) radiation. Since intensity of electromagnetic radiation is proportional to the square of its amplitude, the transmittance is equal to the square of the calculated amplitude quotient and equals 45 % for the investigated silicon sample.

As mentioned before, pure silicon is a non-absorbing material in the THz range. This means that no radiation is absorbed while passing through the sample and that the radiation, which is not transmitted is merely reflected. Having the refractive index of the sample calculated, one can estimate the transmittance through the sample by employing the Fresnel coefficients, which describe the transmission of the radiation at the two boundaries. Using the determined refractive index of 3.42, the transmittance through the two boundaries is 49 %, which approximately fits the transmittance value calculated from the peak-to-peak amplitudes. The discrepancy can be attributed to the measurement uncertainties and impurities in the sample [60].

The evaluation of the refractive index directly from the time-domain data reveals average information about the refractive index of the sample for the whole measured frequency range. Similar is true for the transmittance. This can be an issue for dispersive samples. Furthermore, analysis of the data in the frequency domain can reveal additional information about the sample and is essential for many applications of THz TDS in the pharmaceutical setting (see section 2.2). However, for certain applications such as monitoring transmission of highly absorbing samples, an evaluation in the time domain can be beneficial due to a typically high dynamic range at the peak of the THz pulse [54]. An analogous but more comprehensive analysis can be performed in the frequency domain.

Frequency-domain analysis

In the time-domain analysis, the focus mainly lies on the time-of-arrival of the main and FP THz pulses and their amplitudes. As demonstrated, the pronounced FP pulses reveal valuable information about a sample. Similar holds for the analysis in the frequency domain. However, analysis of measurements containing FP pulses requires their proper consideration to ensure correct interpretation of the extracted results in terms of extracted absorbance, refractive index, and absorption coefficient. To demonstrate the effect of FP pulses on the analysis in the frequency domain, the time-domain signal is processed in two different ways before performing the FFT: once with and once without FP pulses in the signal. The removal of the FP pulses from the original time-domain signal is done, by truncating the signal before the first FP pulse and zero-padding it to the original signal length. The frequency-domain analysis is demonstrated on the same data, which was used for the discussion of the time-domain analysis (i.e., measurement of the silicon wafer). In Figure 9 the spectra corresponding to the time-domain sample measurement with and without FP pulses are shown with the corresponding reference spectra. For clearer representation, only the frequency range between 0.3 and 2 THz is considered.

For the sample spectrum corresponding to the longer time-domain signal containing FP pulses, an oscillating pattern can be observed in the frequency domain. In the case of the shorter signal without any FP pulses, the spectrum is smooth and does not exhibit an oscillating pattern. This oscillating pattern corresponds to the constructive and destructive interference of the radiation passing directly through the sample with the radiation passing through the sample multiple times (see Figure 7). Due to the biplanar sample geometry, the sample can be considered as an optical resonator or a Fabry-Perot etalon. As such the frequency spacing between constructively interfering radiation (v_{FP}) corresponds to the frequency spacing of adjacent modes in a resonator and can be calculated as [61]:

$$v_{FP} = \frac{c}{2nd},$$

2.6

where d is the thickness and n the refractive index of the sample. Considering the refractive index and thickness of the sample extracted from the time-domain data, the frequency spacing for the investigated silicon wafer is approximately 0.08 THz, which agrees with the observed oscillation in the spectrum (Figure 9). According to the equation 2.6, the frequency spacing between v_{FP} is inversely proportional to the optical thickness

19

of the sample (i.e., nd). Furthermore, comparing equations 2.3 and 2.6 reveals that v_{FP} equals $1/t_{FP}$, which is the difference in the time-of-arrival between subsequent FP pulses (see Figure 7). This means that for samples with greater optical thickness the FP pulses appear further apart in the time-domain, however, the period of the oscillation in the frequency domain (i.e., v_{FP}) becomes smaller. On the contrary, for thinner samples the oscillation period becomes greater.
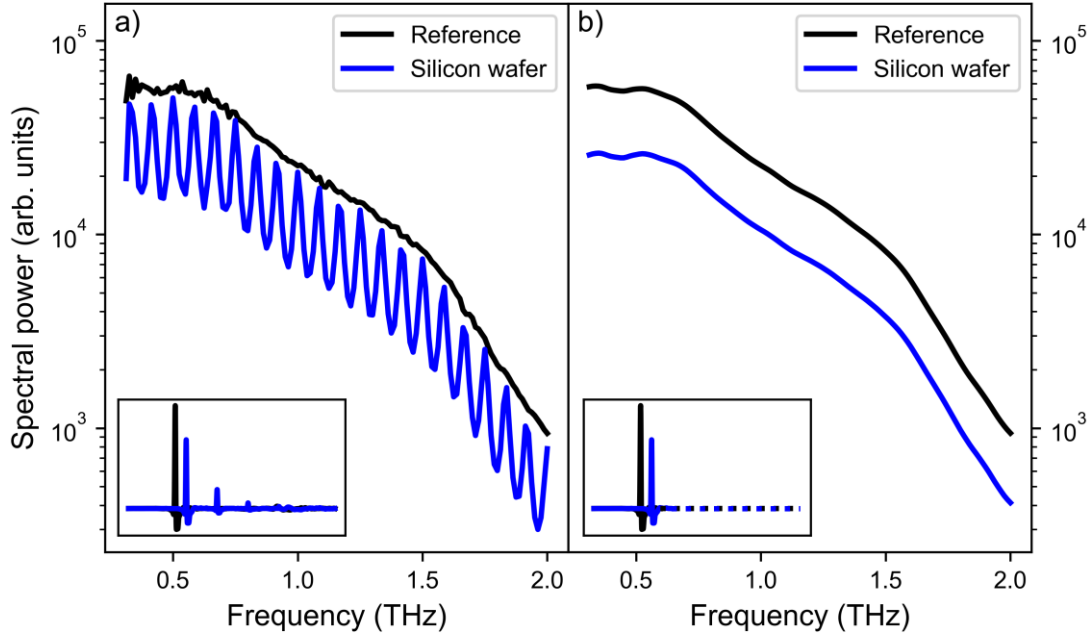
Figure 9. The spectra of the reference and silicon wafer measurement. The results in a) correspond to the time-domain signal of 80 ps length including FP pulses (see Figure 8). The results in b) correspond to the time-domain signal truncated at 30 ps (i.e., before the first FP pulse) and zero padded until 80 ps. The corresponding time-domain data are shown in the insets. The original signals were only offset corrected.

A simple way to analyze a sample is to calculate absorbance, which is typically done without considering any reflection of the radiation by the sample. The absorbance ($A(v)$) in this work is defined as:

$$A(v) = -10 \cdot \log_{10}\big(T(v)\big) = -10 \cdot \log_{10}\left(\frac{I_{sam}(v)}{I_{ref}(v)}\right) = -20 \cdot \log_{10}\left(\frac{\left|\tilde{E}_{sam}(v)\right|}{\left|\tilde{E}_{ref}(v)\right|}\right), \qquad 2.7$$

where $T(v)$ is frequency dependent transmittance of the sample. $I_{sam}(v)$ and $I_{ref}(v)$ are frequency dependent intensity of the radiation transmitted through the sample and the reference material (i.e., air), respectively. $\tilde{E}_{sam}(v)$ and $\tilde{E}_{ref}(v)$ are frequency dependent complex electric field amplitudes, which are calculated by performing FFT of the recorded time-domain signals corresponding to the sample and reference measurement, respectively. Since the intensity of the detected radiation is proportional to its power, the shape of the absorbance spectrum corresponds to the difference between the reference and sample measurement shown in the logarithmic scale in Figure 9. The absorbance spectra of the silicon wafer corresponding to the time domain signal with and without FP pulses are shown in Figure 10.
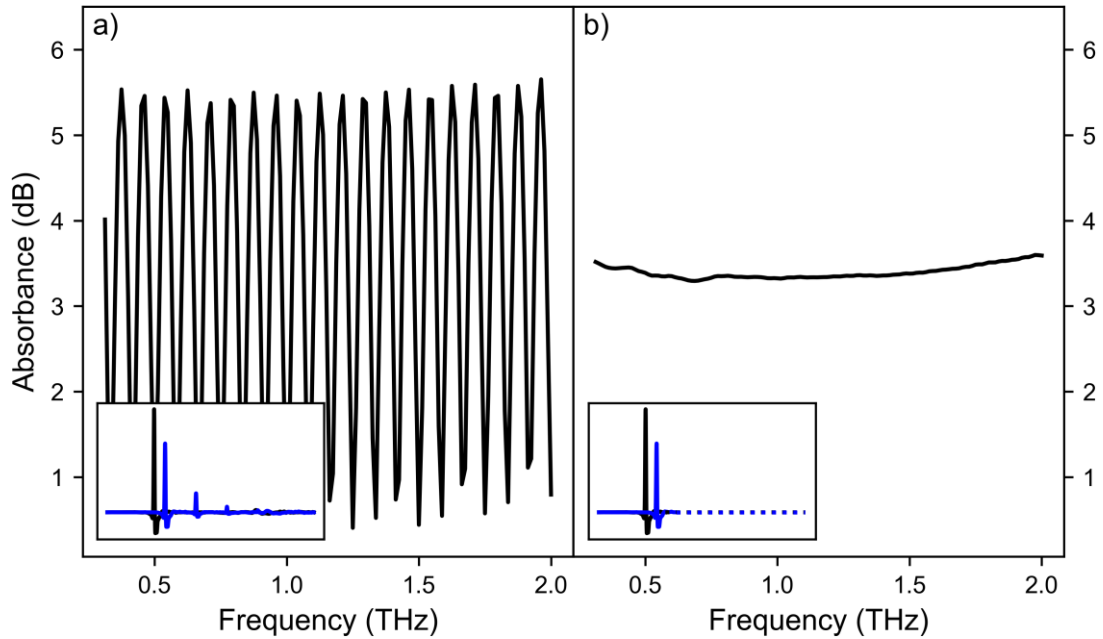
Figure 10. Absorbance of the silicon wafer. The result in a) corresponds to the time-domain signal of 80 ps length including FP pulses (see Figure 8). The result in b) corresponds to the time-domain signal truncated at 30 ps (i.e., before the first FP pulse) and zero padded until 80 ps. The corresponding time-domain data are shown in the insets. The original signals were only offset corrected.

As expected, a similar oscillation pattern can be observed in the absorbance spectrum when the time-domain signal with the FP pulses is considered. The absorbance oscillates with frequency approximately between 0 dB and 6 dB, which corresponds to the constructive and destructive interference, respectively. However, if the time-domain signal does not include the FP pulses a nearly constant absorbance of approximately 3.5 dB is observed. This corresponds to approximately 55 % losses, meaning that approximately 45 % of the radiation energy was transmitted through the sample. The same result was observed in the time-domain analysis. Since the reflection losses are not considered when calculating the absorbance, the 3.5 dB losses can again be, at least partially, contributed to the reflection of the THz radiation at the air-sample interfaces. Furthermore, for absorbing materials, the total absorbance depends also on the sample thickness. Therefore, care must be taken when interpreting the absorbance spectra. Nevertheless, useful, and valuable results can be drawn from the absorbance spectra.

A more comprehensive analysis is needed to extract the complex refractive index of a sample from THz TDS transmission measurements. The complex refractive index is a material property, which is independent from the sample geometry and thickness. Therefore, to extract it from the measured data, the interaction of the radiation with the sample must be carefully considered. Investigating a flat biplanar sample and considering the radiation interacting with the sample as plane waves, a so-called transfer function ($\tilde{T}(v)$) can be written as:

$$\tilde{T}(v) = \frac{\tilde{E}_{sam}(v)}{\tilde{E}_{ref}(v)} = \frac{\tilde{E}_0(v)\tau_{1,2}\tau_{2,1}e^{ik\tilde{n}(v)d}}{\tilde{E}_0(v)e^{ikd}} \sum_{m=0}^{N}\left(\rho_{2,1}\rho_{1,2}e^{i2k\tilde{n}(v)d}\right)^m, \qquad 2.8$$

where i is the imaginary unit (i.e., $i = \sqrt{-1}$), k is the wave number, $\tilde{n}(v)$ is the frequency dependent complex refractive index of the sample, $\tilde{E}_0(v)$ is the complex electric field amplitude of the incident radiation, $\tau_{1,2}$ and $\tau_{2,1}$ are Fresnel transmission coefficients at the first and second interface (see Figure 7), respectively, and $\rho_{1,2}$ and $\rho_{2,1}$ are Fresnel reflection coefficient at the same two interfaces, respectively. Furthermore, all Fresnel coefficients depend on the complex refractive index of the sample and as such are also frequency dependent. Finally, N is the number of FP pulses within the measured time-domain signal. Note that the term in the numerator multiplied with the summation term describes the radiation propagating through the sample and that the term in the denominator describes the propagation of the radiation through the reference medium of the same thickness (i.e., air with thickness d and refractive index of one). Furthermore, $\tilde{E}_{sam}(v)$ and $\tilde{E}_{ref}(v)$ are the corresponding complex electric field amplitudes acquired from the THz TDS sample and reference measurements.

The goal is to determine the real (n) and imaginary part (κ) of the complex refractive index ($\tilde{n} = n + i\kappa$) by solving equation 2.8. The real part of the refractive index is often simply referred to as the refractive index and the imaginary part as the extinction coefficient. This terminology will be used from here on. The extraction of the refractive index and extinction coefficient from equation 2.8. can be done only numerically. However, the equation 2.8 can be further simplified and the refractive index and extinction coefficient can be expressed analytically, if two requirements are met. The first requirement is that there are no FP pulses present in the measured time-domain signal (N in equation 2.8 equals to zero), which requires sufficient sample thickness. This way the summation term in the equation 2.7 equals to one. Furthermore, by using the definitions of the wave number ($k = 2\pi/\lambda$), complex refractive index ($\tilde{n} = n + i\kappa$), and Fresnel transmission coefficients for the normal incidence, the equation 2.8 can be rewritten as:

$$\tilde{T}(v) = \frac{4\tilde{n}(v)}{(\tilde{n}(v) + 1)^2}e^{i\frac{2\pi}{\lambda}(\tilde{n}(v)-1)d} \qquad 2.9$$

The second requirement to analytically retrieve the complex refractive index from the transfer function is that the real part of the complex refractive index is much greater than the imaginary part ($n \gg \kappa$). This way the equation 2.8 can be simplified to:

$$\left|\tilde{T}(v)\right|e^{i\Delta\varphi(v)} = \frac{4n(v)}{(n(v) + 1)^2}e^{i\frac{2\pi v}{c}(n(v)-1)d}e^{-\frac{2\pi v}{c}\kappa(v)d}, \qquad 2.10$$

where $\tilde{T}(v)$ is rewritten in the polar notation of complex numbers and $\Delta\varphi(v)$ is the frequency dependent phase difference of the electric field between the sample and reference measurement. In the last step the relation between the frequency, wavelength, and speed of light (i.e., $c = \lambda v$) of electromagnetic radiation was also considered. The equation 2.10 can be rewritten into two equations by separately considering the real and imaginary part of the equation. Thus, the refractive index and extinction coefficient can be expressed as:

$$n(v) = 1 + \frac{c\Delta\varphi(v)}{2\pi v d},$$
<div align="right">2.11</div>

$$\kappa(v) = -\frac{c}{2\pi v d} \ln\left(\frac{(n(v)+1)^2}{4n(v)}\left|\tilde{T}(v)\right|\right).$$
<div align="right">2.12</div>

Furthermore, the extinction coefficient and the absorption coefficient ($\alpha(v)$) are related as:

$$\alpha(v) = \frac{4\pi v}{c}\kappa(v) = -\frac{2}{d}\ln\left(\frac{(n(v)+1)^2}{4n(v)}\left|\tilde{T}(v)\right|\right).$$
<div align="right">2.13</div>

By knowing the absorption coefficient of a material, the intensity of the electromagnetic radiation propagating through an absorbing material can be determined according to the Beer-Lambert law:

$$I(v) = I_0(v)e^{-\alpha(v)d},$$
<div align="right">2.14</div>

where I_0 is the initial intensity of the radiation and I is the intensity after radiation propagated through a material layer of thickness d.

Since the refractive index is needed for the calculation of the extinction and absorption coefficients, the refractive index must be extracted first. To do so, the sample thickness and the phase difference are required. On the one hand, the thickness of a flat biplanar sample can be reliably measured using a vernier caliper or a micrometer screw gauge. On the other hand, the calculation of phase difference requires some additional consideration. First, the calculation of the phase angle should be done using four quadrant arctangent function, which returns the values in the whole $[-\pi, \pi]$ range [62]. However, this still means that whenever the absolute value of the phase exceeds π, it changes the polarity by 2π, which causes discontinuity in the phase spectrum in terms of phase-jumping between $-\pi$ and π [51]. To overcome this issue, the so-called phase unwrapping needs to be performed, which is followed by the DC phase offset correction. The latter is done by fitting a linear function to the unwrapped phase in the spectral part with the highest SNR and extrapolating it to the zero frequency. Then the extrapolated value at the zero frequency is subtracted from the whole unwrapped phase [51]. A tutorial by P. Jepsen [62] provides more details about phase retrieval and common pitfalls in the process. In Figure 11 the real part of the refractive index of the silicon wafer extracted from the THz TDS measurement (see Figure 8) is shown. Again, once the whole time-domain signal including FP pulses and once a windowed signal without FP pulses is considered.
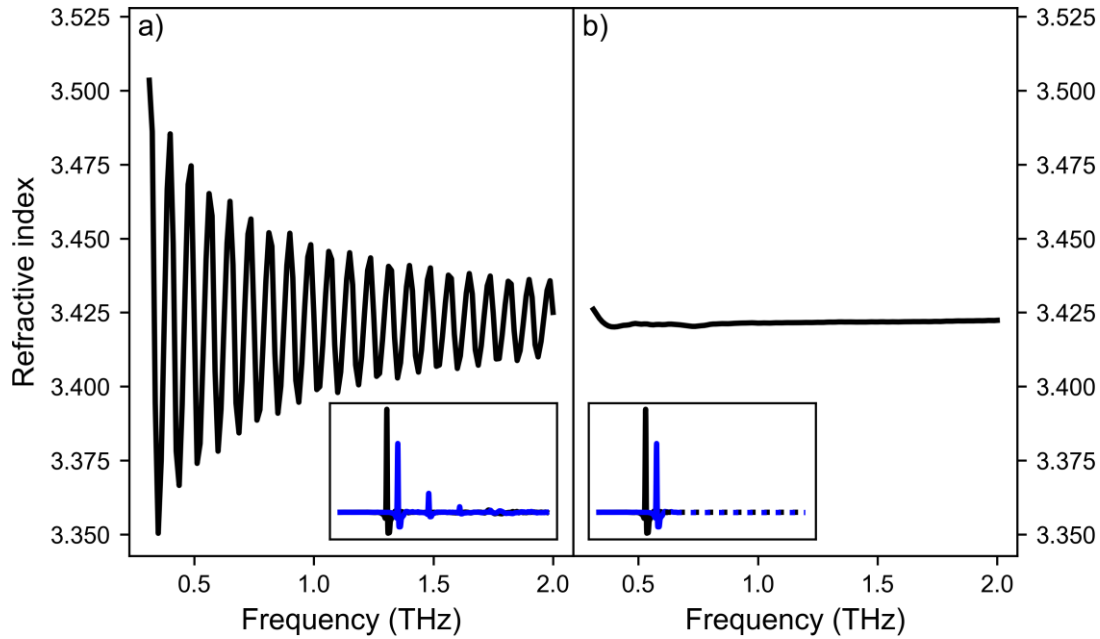
Figure 11. Refractive index of the silicon wafer. The result in a) corresponds to the time-domain signal of 80 ps length including FP pulses (see Figure 8). The result in b) corresponds to the time-domain signal truncated at 30 ps (i.e., before the first FP pulse) and zero padded until 80 ps. The corresponding time-domain data are shown in the insets. The original signals were only offset corrected.

When FP pulses are included in the signal but not accounted for in the evaluation of the refractive index, an oscillating pattern can be observed again. By truncating the signal before the first FP pulse, the oscillating values of the refractive index are avoided. The extracted refractive index values approximately match the reported values for silicon [51,57,60]. The small deviation can be again attributed to the uncertainty due to the system instability and the uncertainty of sample thickness determination. Having the refractive index calculated, the absorption coefficient can be extracted as well. The absorption coefficient is shown in Figure 12, once for the calculation based on the whole signal length and once based on the signal truncated before the first FP pulse.

The oscillating pattern can again be observed in the frequency dependent representation of the absorption coefficient when the FP pulses are included in the signal and not accounted for in the evaluation. In addition, also negative values of the absorption coefficient appear. This "unphysical" result would mean, that for certain frequencies the investigated material amplifies the incident radiation. However, in the case of the absorption coefficient evaluation based on the truncated time-domain signal without FP pulses, which agrees with the model assumption (equation 2.9), again a smooth, non-oscillating frequency dependence can be observed. The average value of the absorption coefficient in the shown frequency range is approximately 1.4 cm^{-1}. This means that according to the performed measurement, the investigated silicon wafer is slightly absorbing. This agrees with observations reported in the literature for silicon samples with lower resistivities, however, exceeds the expected values for the given sample resistivity [60]. Furthermore, it is important to consider that there is uncertainty about the extracted values due to different uncertainty sources (e.g., sample thickness, system

24

instability, sample positioning). A detailed description of the uncertainty analysis can be found in literature [63,64].
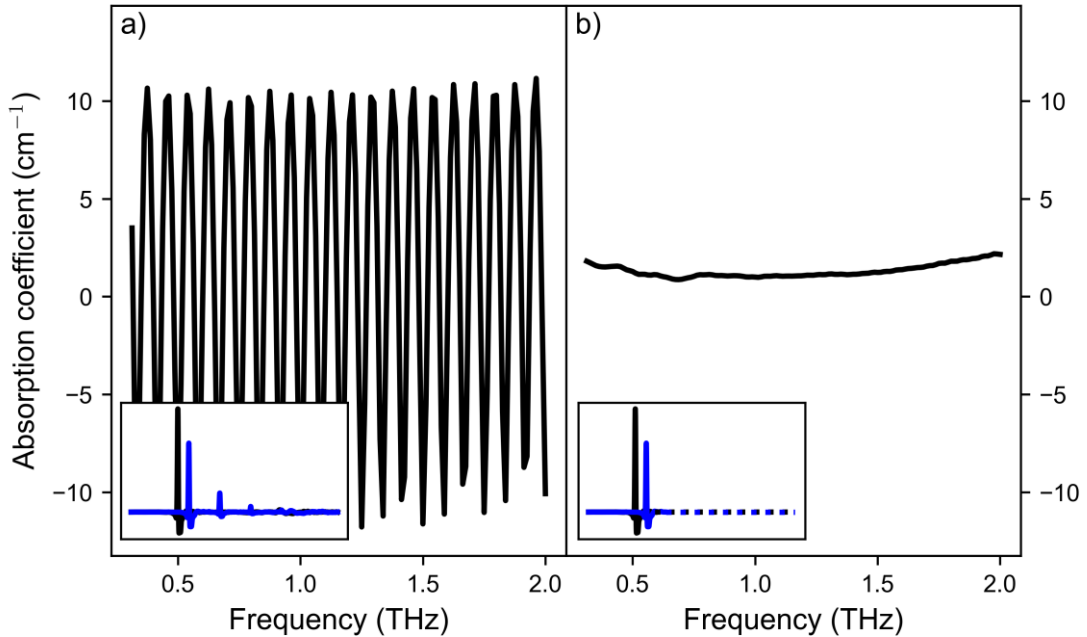
Figure 12. Absorption coefficient of the silicon wafer. The result in a) corresponds to the time-domain signal of 80 ps length including FP pulses (see Figure 8). The result in b) corresponds to the time-domain signal truncated at 30 ps (i.e., before the first FP pulse) and zero padded until 80 ps. The corresponding time-domain data are shown in the insets. The original signals were only offset corrected.

Comparing the extracted absorbance (Figure 10) with the absorption coefficient (Figure 12) reveals similar spectral shape and features. This indicates that absorbance provides useful information about the absorption of a material especially for materials with pronounced spectral absorption features. However, the presence of FP pulses in the measured time-domain signal can significantly alter the absorbance spectra as well as the values of the extracted absorption coefficient. This is also true for the extraction of the refractive index. A straightforward way to overcome such problems is to measure a sample with sufficient thickness. This way the FP pulses can be easily truncated from the time-domain signal and their effect on the frequency-domain analysis diminishes as shown on the example of the silicon wafer. This, however, can become challenging if the investigated material is strongly absorbing and the dynamic range of the spectrometer is exceeded [56]. Such problems can be encountered also during the investigation of pharmaceuticals, which can be strongly absorbing. A common way to overcome this issue when investigating pharmaceuticals is to dilute the investigated sample in a non-absorbing material (e.g., mixing powder of a pharmaceutical with polyethylene powder) as discussed in more detail in section 2.2. Another option is to take the FP pulses properly into account and to numerically extract the refractive index and absorption coefficient [65]. Furthermore, similar oscillation patterns appear in the extracted parameters if the sample thickness is inaccurately determined, which can be also useful for simultaneous extraction of the sample thickness [66]. The results of such extraction for the investigated silicon wafer are shown in Figure 13 and Figure 14 for refractive

index and absorption coefficient, respectively. The extraction was performed with a commercially available software called TeraLyzer, which is based on algorithms presented in [55,67,68]. Furthermore, the sample thickness was also simultaneously evaluated based on the quasi space optimization [68] within the software and determined to be 522 µm. This thickness was also used for the parameter extraction from signals truncated before the first FP pulse when using the TeraLyzer software, which are shown in Figure 13 b) and Figure 14 b). The extracted values were additionally filtered within the confidence interval of the transfer function based on the evaluated measurement uncertainty using five iterations of the SVMAF filter [55].

Figure 13. Refractive index of the silicon wafer extracted with the TeraLyzer. The dotted curve corresponds to the extracted values before SVMAF filtering and the solid curve corresponds to the SVMAF filtered values. The result in a) corresponds to the time-domain signal of 80 ps length including FP pulses (see Figure 8). The result in b) corresponds to the time-domain signal truncated at 30 ps (i.e., before the first FP pulse) and zero padded until 80 ps. The corresponding time-domain data are shown in the insets. The original signals were only offset corrected. The shaded areas around the curves correspond to the uncertainty of the extracted values evaluated based on the signal variation between the repeated measurements.

By correctly considering the FP pulses in the evaluation of the refractive index and absorption coefficient from the whole measured time-domain signal, the oscillation pattern becomes less pronounced and completely diminishes after applying the SVMAF filter. The latter is expected since the oscillations appear within the uncertainty interval of the extracted values. Furthermore, evaluation of the data truncated before the first FP pulse again results in smooth curves as previously observed (see Figure 11 and Figure 12). On the one hand, the refractive index values extracted using the TeraLyzer are higher than the values extracted using equation 2.11 (Figure 11), which is due to the differently determined sample thickness. On the other hand, the difference in the extracted absorption coefficient between the evaluation with the TeraLyzer and according to the equation 2.12 is much smaller than the uncertainty of the extracted

values. The remaining oscillation pattern, which can be observed for the evaluation based on the time-domain signal containing FP pulses, indicates that the propagation of the radiation through the sample is not perfectly modeled (equation 2.8). Since the sample was measured in the focus of the THz beam, the assumption that THz waves interacting with the sample are plane waves is not completely met. By placing the sample in the focus of the beam, the object plane and the image of the sample at the detector are displaced, which can affect the extraction of refractive index and absorption coefficient, if not correctly considered [69]. Nevertheless, the extracted values are in close agreement with the reported values for silicon [69,70] especially when considering the uncertainty interval of the extracted values and the uncertainty of the sample thickness determination.
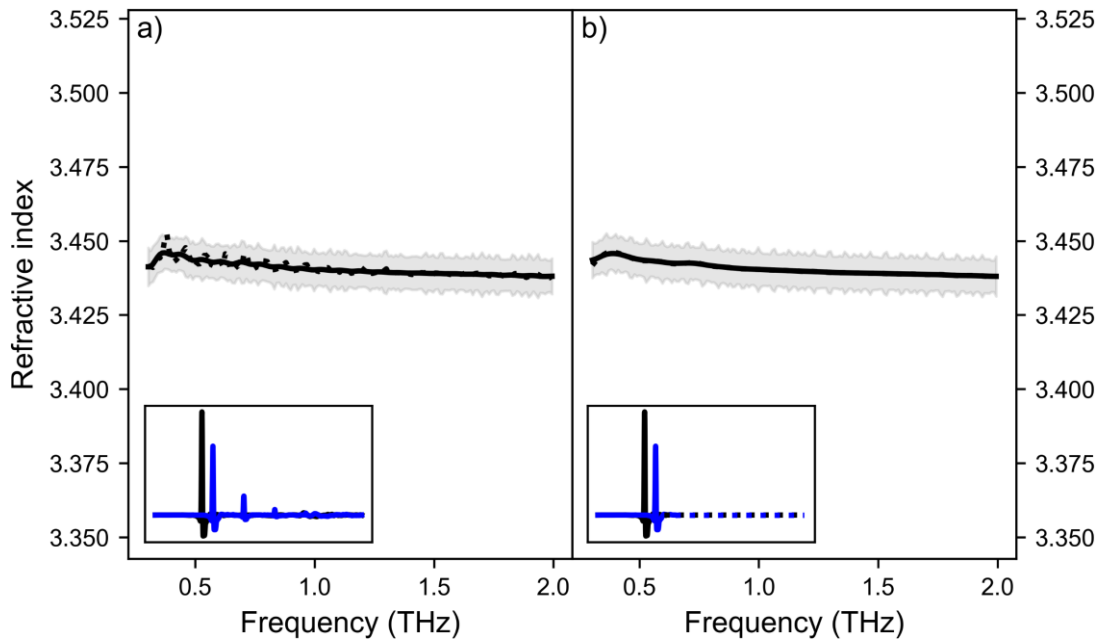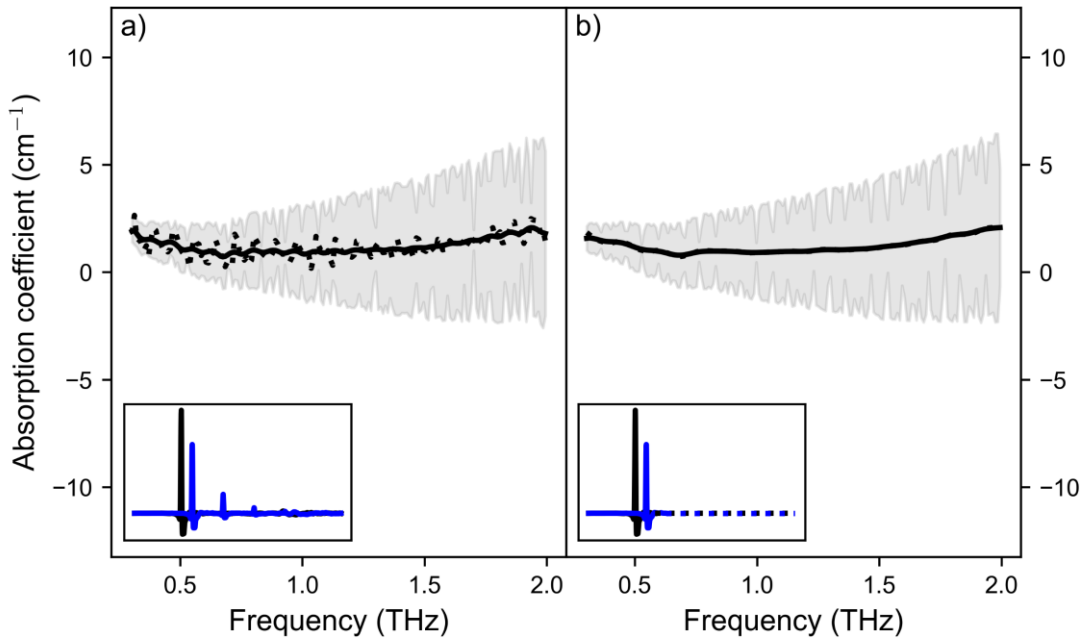

Figure 14. Absorption coefficient of the silicon wafer extracted with the TeraLyzer. The dotted curve corresponds to the extracted values before SVMAF filtering and the solid curve corresponds to the SVMAF filtered values. The result in a) corresponds to the time-domain signal of 80 ps length including FP pulses (see Figure 8). The result in b) corresponds to the time-domain signal truncated at 30 ps (i.e., before the first FP pulse) and zero padded until 80 ps. The corresponding time-domain data are shown in the insets. The original signals were only offset corrected. The shaded areas around the curves correspond to the uncertainty of the extracted values evaluated based on the signal variation between the repeated measurements.

In this subsection the evaluation of sample properties which is performed by comparing the signal of the sample measurement with the signal of the reference measurement in the transmission geometry was presented. The two signals can be compared in the time domain or in the frequency domain. In the former case, an average value of refractive index, absorbance, and absorption coefficient for the whole frequency range can be estimated, which can be rather inaccurate for samples with a strong frequency dependence of the refractive index and absorption coefficient. In the latter case, a frequency dependent evaluation of the material properties can be carried out. In both cases, a proper determination of the sample thickness is crucial for a successful

evaluation. Furthermore, FP pulses, which correspond to the multiple round-trip of the radiation within the biplanar sample, can be used for thickness estimation directly from the THz TDS measurement. However, if not correctly considered, the presence of the FP pulses in the data can lead to an oscillating pattern of the extracted frequency dependent material parameters, which can make the interpretation of the data troublesome. Nevertheless, with the proper experimental procedure and data evaluation, the refractive index and absorption coefficient of the investigated sample can be directly extracted from the THz TDS transmission measurement. In the following subsection an investigation of samples in a reflection geometry using THz TDS is presented.

2.1.3 Reflection geometry

THz TDS in reflection geometry is the method of choice for investigation of highly absorbing, thick samples and objects which cannot be investigated in transmission geometry due to their size or shape. The key idea of the investigation in the reflection geometry is to detect the reflected part of the incident radiation and extract the sample properties from it. Considering the normal incidence case, the reflected part of the beam propagates back in the direction of the incident beam. This means that the reflected beam must be spatially separated from the incident beam or the emitter and detector antenna should at least nearly coincide. The latter can be achieved by monolithic integration of emitter and detector antennas [71]. In the former case, a THz beam splitter can be used to split the reflected beam towards the detector, which is, however, connected with additional signal losses due to the beam splitting [57,72]. Another option is to forgo the normal incidence and to direct the incident beam to the sample surface at some different angle and detect the specular reflected radiation. This way the reflected beam does not coincide with the incident beam, which means that the position of the detector does not interfere with the position of the emitter [72]. However, the angle of incidence as well as the polarization of the incident radiation must be well-defined and properly accounted for when extracting the sample properties [73]. Nevertheless, for some applications the THz beam path is constructed in a way that the incident beam is nearly parallel to the surface normal (i.e., approximately normal incidence), however, the angle deviation is sufficient to separately guide the reflected beam to the detector without using a beam splitter [74,75]. This enables a compact construction of the THz beam path and an easy alignment of the sample. Furthermore, due to a small angular deviation from the normal incidence, the interaction of the THz radiation with the sample can be, in the first approximation, described by assuming normal incidence, which simplifies the analysis.

Another type of reflection configuration is the attenuated total reflection (ATR) spectroscopy, which requires that the radiation propagates in a medium with a higher refractive index than that of the sample. Furthermore, the angle of incidence must exceed the critical angle. In the case of THz ATR spectroscopy, this is often achieved by using a silicon prism, which is placed into a THz beam path of a transmission setup and the sample is placed on top of the prism. This way the THz radiation is coupled into a silicon prism, reflected from the sample on top of the prism and then guided to the detector after exiting the prism [76–80]. A THz ATR setup with an emitter and detector antenna integrated directly on a prism has also been demonstrated [81].

All these different THz reflection configurations require proper consideration and mathematical modeling when analyzing the sample and extracting its properties in the THz range. In addition, there are also different ways to perform a reference measurement, which must be considered during the data evaluation as well. Furthermore, in the case of ellipsometry a sample independent reference measurement is not needed [82]. Describing all these possibilities in detail is out of the scope of this work. Therefore, only normal incidence is considered in the following part of this subsection to provide a basic understanding of sample investigation in the reflection geometry. First investigation of samples consisting of a single layer is considered. This is followed by the conceptual description of THz tomography based on multilayered samples.

One-layer samples

Considering only normal incidence, different sample configurations in THz reflection spectroscopy are possible. Three common configurations are shown in Figure 15. The main difference arises from the way the reference measurement is acquired. The three sample configurations are compatible with different instrumentation used in the reflection geometry as discussed above (e.g., transceiver-based, beam-splitter-based).
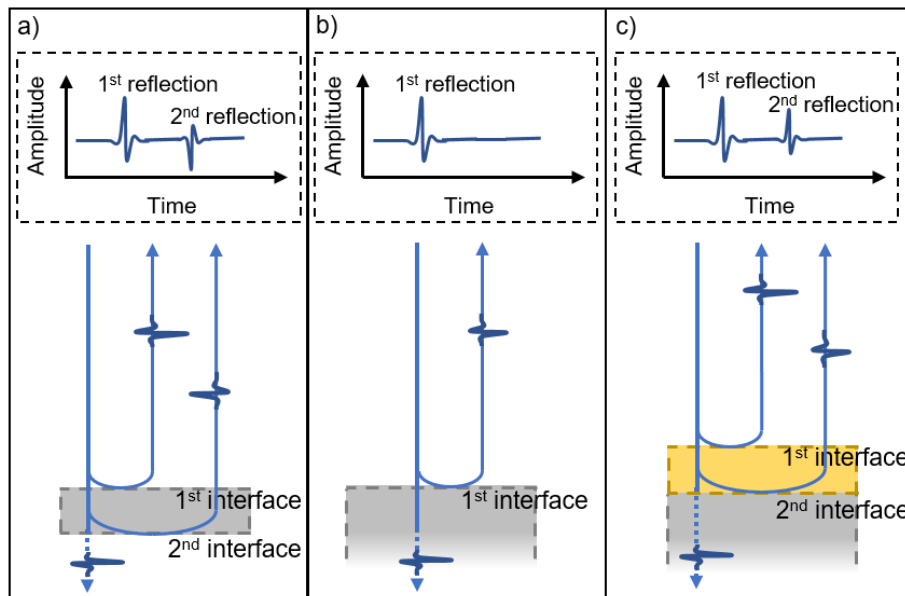
Figure 15. Schematic representation of THz radiation propagating downwards under normal incidence towards the sample for three different sample configurations. a) A biplanar low-absorbing sample of sufficient thickness with recorded THz pulses originated from the first (air – sample) and second (sample – air) interface. b) A thick biplanar sample with a single recorded THz pulse originated from the first (air – sample) interface. c) A thick biplanar sample placed in contact with a reference window on top and THz pulses originating from the first (air – reference window) and second (reference window – sample) interface. The radiation transmitted through the sample (dashed arrows) is not detected. Only radiation reflected in the direction of the incident radiation is detected. Multiple reflections within the sample or the reference window are not considered. The signal consisting of the recorded reflected THz pulses corresponding to the schematic of the radiation propagation is shown in the insets above.

In the first configuration the dielectric properties of a biplanar sample can be extracted by separately considering the two THz pulses, one originating from the first interface and the other from the second interface of the sample surrounded with air (Figure 15 a). The difference in the time of arrival of the two pulses corresponds to twice the optical thickness of the sample. By measuring the thickness of the sample, an average refractive index of the sample can be extracted, similar as in transmission geometry (see subsection 2.1.2). Furthermore, the time-domain signal can be divided into two separate signals by separately windowing the time-domain signal in the proximity of the first and of the second pulse. The two signals can be then considered as two separate measurements. It is important to note that the sample must be on the one hand sufficiently thick and on the other hand low absorbing so that the two pulses can be separately processed. This, however, means that the reflection spectroscopy in this configuration, similar to transmission spectroscopy, is not appropriate for investigation of highly absorbing samples, since THz radiation propagating twice through the sample must be detected and analyzed. The transfer function (T_a) for this configuration can be written as [57]:

$$\tilde{T}_a = \frac{\tilde{E}(v)_{2^{nd}}}{\tilde{E}(v)_{1^{st}}} = \frac{\tilde{E}_0(v)\tau_{1,2}\rho_{2,1}\tau_{2,1}e^{i2k\tilde{n}(v)d}}{\tilde{E}_0(v)\rho_{1,2}} = -\tau_{1,2}\tau_{2,1}e^{i2k\tilde{n}(v)d}, \qquad 2.15$$

where $\tilde{E}(v)_{2^{nd}}$ and $\tilde{E}(v)_{1^{st}}$ are the complex electric field amplitudes of the radiation reflected from the second and first interface, respectively. Comparing this equation with the transfer function for transmission geometry without any FP pulses in the measured signal (i.e., $m = 0$ in equation 2.8) reveals that the two transfer functions are almost identical. There is a difference between the two transfer functions in the exponential terms, which describe the propagation of the radiation. Therefore, if the same approximations are considered, the refractive index, extinction coefficient, and absorption coefficient can be expressed in a similar way as from equations 2.11-2.13, respectively. Note that proper phase processing in terms of phase unwrapping must be performed as well (see subsection 2.1.2 for more detail).

In the second configuration shown in Figure 15 b the reflection only from the first interface (air – sample) is considered. This requires a sufficient thickness of the sample so that the THz pulses originating from the back side of the sample can be neglected in the analysis. To extract the sample properties, the measured signal must be compared with a signal originating from a known, reference sample (i.e., a reference measurement). Often polished metal mirrors are used as reference samples and their reflection coefficient is considered to equal $\rho_{ref} = -1$. The exact positioning of the reference mirror and sample in the same plane is crucial for accurate investigation of a sample in this configuration since already small misalignments can affect the extraction of refractive index and absorption coefficient of the sample [83]. The transfer function for this configuration ($\tilde{T}_b$) can be written as:

$$\tilde{T}_b = \frac{\tilde{E}(v)_{sam}}{\tilde{E}(v)_{ref}} = \frac{\rho_{1,2}\tilde{E}_0(v)}{-\tilde{E}_0(v)} = -\rho_{1,2} \qquad 2.16$$

and the refractive index and absorption coefficient can be directly expressed in terms of two simple equations [56]. Furthermore, since there are no exponential terms describing

the propagation of the radiation in the transfer function describing this configuration, no phase unwrapping is needed before the extraction of the refractive index and absorption coefficient [62]. Highly absorbing samples can be investigated in this configuration since the radiation propagating through the sample is not considered in this evaluation. The largest detectable absorption coefficient can be determined by the scan-to-scan reproducibility of the results and not by the dynamic range of the spectrometer, which is the case in transmission geometry [56].

In the third configuration shown in Figure 15 c an additional reference window is placed in contact with the sample and THz pulses reflected from the firs (air – reference window) and the second (reference window – sample) interface are analyzed. Like in the first configuration (Figure 15 a), the time-domain signal can be divided into two separate signals by windowing the recorded signal in the proximity of the two THz pulse, for which the reference window should be sufficiently thick and preferably non-absorbing. The signal with the THz pulse originating from the first interface can be considered as a reference signal since the radiation originates from an interface between two known materials (i.e., air and reference window). The second signal corresponds to the THz radiation originating from the second interface between a known reference material and an investigated, unknown sample. Again, a sufficient thickness of the sample is required so that the THz pulses originating from the back side of the sample do not interfere with the analysis. The transfer function for this configuration can be written as:

$$\tilde{T}_c = \frac{\tilde{E}(v)_{2^{nd}}}{\tilde{E}(v)_{1^{st}}} = \frac{\tilde{E}_0(v)\tau_{1,2}\rho_{2,3}\tau_{2,1}e^{i2k\tilde{n}_2(v)d_2}}{\tilde{E}_0(v)\rho_{1,2}}, \qquad\qquad 2.17$$

where $\tilde{n}_2(v)$ and d_2 are complex refractive index and thickness of the reference window. The indices 1, 2, and 3 correspond to air, reference window, and investigated sample, respectively. To ensure a sufficient amplitude of the recorded signal corresponding to the second THz pulse, a non-absorbing window is preferred. Employing a non-absorbing window also simplifies the extraction of the refractive index and absorption coefficient of the investigated sample, which can again be directly expressed in terms of two independent equations [57,72,84]. The advantage of this configuration is that the radiation does not have to propagate through the sample, which allows for investigation of strongly absorbing samples. Furthermore, the problems of slight mispositioning of a reference mirror are avoided, as an extra reference measurement is not needed. However, it is important to ensure a proper contact between the reference window and the sample, which typically requires smooth and flat surface of the window and of the investigated solid sample.

So far investigation of samples consisting out of only a single layer was considered while focusing on the extraction of the refractive index and absorption coefficient of the investigated sample from a reflection measurement. Furthermore, the emission of THz radiation in form of short pulses enables independent observation of pulses originating from different sample interfaces. This pulsed nature of THz TDS offers a rather straightforward way for tomographic investigation of multilayered samples. The basic concept of THz tomography is discussed in the next part of this subsection.

Terahertz tomography of multilayered samples

The concept of THz tomography in terms of internal structure imaging presented in here is based on the experiment reported by Mittleman et al. in 1997 and conducted on a floppy disk [85]. This technique is often referred to as terahertz pulsed imaging (TPI). It relies on identification of reflected THz pulses in the time domain and can be used for structural imaging of multilayered objects.

When radiation propagates through such a multilayer sample, part of the radiation is reflected at each layer interface. Considering the pulsed nature of THz TDS, the reflected radiation at each interface results in a THz pulse recorded in the time-domain signal. Figure 16 shows a sample consisting of five different material layers and an exemplary time-domain signal with the five THz pulses corresponding to the reflections at the five interfaces. The key idea of THz tomography is to identify these THz pulses from the recorded time-domain signal, determine their time-of-flight and assign them to the corresponding interfaces.
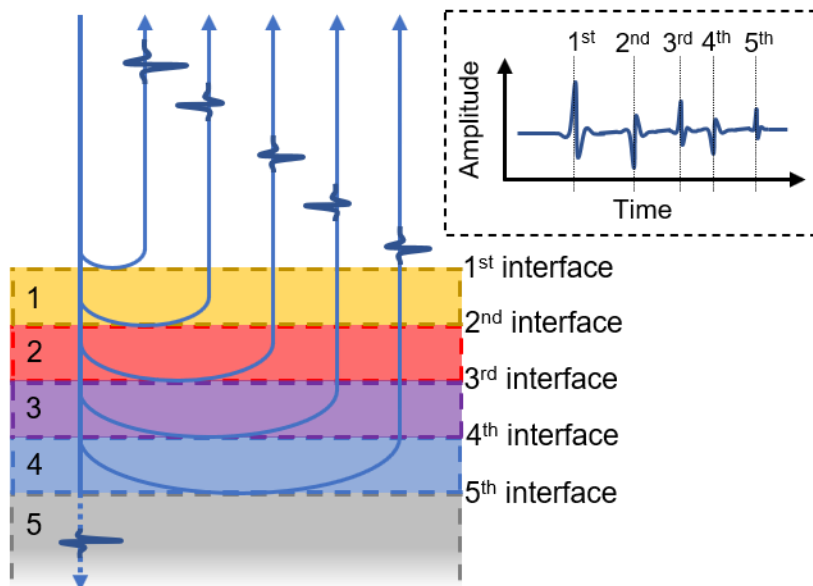
Figure 16. A sample consisting of five different material layers measured in reflection geometry. Part of the radiation is reflected at each interface resulting in THz pulses in the recorded time-domain signal. An exemplary time-domain signal corresponding to the multilayer sample is shown in the inset. Note that the first interface commonly corresponds to the boundary between the surrounding medium (e.g., air) and the first material layer.

Amplitude, shape, and time-of-flight of the THz pulses depends on the material properties and thicknesses of the individual layers. Considering non-absorbing and non-dispersive media, the amplitude of the recorded THz pulses depends on the amplitude of the radiation incident on the interface and the refractive indices of the two materials forming the interface, as described by the Fresnel coefficients. Furthermore, the shape of the recorded THz pulse depends on which layer has a higher refractive index. If the radiation propagates into optically denser (i.e., higher refractive index) material, the recorded THz pulse will be flipped (i.e., mirrored with respect to the time-axis) compared to the case when the radiation enters a layer with a lower refractive index. This is due to the "phase jump" that radiation experiences when entering an optically denser medium.

In addition to the different amplitude and shape of the THz pulses, the time at which the THz pulse is detected (i.e., time-of-flight) is essential for tomographic reconstruction of a multilayered sample. The difference in time-of-flight between the two consecutive pulses ($\Delta t_{i,i+1}$) is proportional to the product of the refractive index (n_i) and the thickness (d_i) of the layer between the two interfaces (i.e., optical thickness) and can be written analogous to equation 2.3 as:

$$\Delta t_{i,i+1} = \frac{2n_i d_i}{c},$$
<div align="right">2.18</div>

where index i corresponds to the interface and the layer number. By knowing the average refractive index of the different material layers in the THz range, the thickness of the individual layers can be determined. This way the internal structure of the sample can be resolved. The refractive index of materials forming the individual layers can be obtained separately by investigating samples made from individual materials in transmission (see subsection 2.1.2). In the case of thin individual layers, the pulses originating from the two interfaces of the layer can overlap and therefore make the estimation of Δt troublesome. In such cases different deconvolution algorithms can be employed to resolve the time position of the individual pulses [86].

The described time-of-flight analysis represents the fundamental of TPI or THz tomographic investigation performed in the time domain. TPI has found applications in different fields (e.g., conservation [87–89] and non-destructive inspection of arts [90,91] Furthermore, investigation of paint layer thickness in automotive industry based on sophisticated evaluation models of the THz TDS reflection measurements is currently one of the promising industrial applications of THz TDS [35,92,93]. Furthermore, evaluation of the coating thickness of pharmaceutical tablets has been successfully demonstrated based on the THz TDS tomographic investigation [94–96]. Inspection of tablet coatings is one of the applications of THz TDS related to the field of pharmaceuticals. In the following section applications of THz TDS in pharmaceutical setting are presented in more detail.

2.2 Applications of THz TDS in the field of pharmaceutics

The concepts of THz TDS presented in the previous section have been widely employed for the investigation of pharmaceuticals and pharmaceutic formulations. A great part of the investigation has been performed in the transmission geometry focusing on properties of APIs. The pure, solid APIs are commonly purchased in form of powders and are pressed into biplanar tablets for easier handling and THz investigation. The purchased powders are often additionally grinded with mortar and pastel before being pressed into tablets to minimize the effect of scattering on the investigation [97,98]. Furthermore, such powder samples can also be diluted by mixing them with an additional fine-granulated, low absorbing powder (e.g., polyethylene). This is done to ensure that the tablet stays firm and does not break or crack too easily. One further reason to do so, is to be able to make samples of greater thickness (e.g., exceeding 1 mm) even if the API is strongly absorbing in the THz range, which is often the case. Furthermore, having a sample of sufficient thickness simplifies the evaluation of the sample properties in a way that the FP pulses do not have to be considered during the evaluation as discussed in subsection 2.1.2. On the one hand, this is especially useful, if only absorption features

or changes in absorbance are of interest. On the other hand, the extraction of the refractive index and absorption coefficient of the API from a THz TDS measurement becomes more challenging this way since the sample is a mixture of the API, additional powder, and small air voids. Such samples can be described as an effective medium, whose dielectric properties depend on the dielectric properties of the constituting materials and their proportions in the sample. This means that the dielectric properties of the investigated API in such a diluted sample can be extracted, if proper proportions of all the substances in the mixtures and the dielectric properties of the remaining substances are known [99]. It is fair to mention that even if samples for THz investigation are prepared by pressing only the API powder (i.e., no dilutant powder used), inclusion of air voids in the sample is unavoidable. This again affects the measured refractive index and absorption coefficient of the API. The same is true for the scattering as the sample consists of many small particles, whose size can differ based on how the sample was prepared, which in turn affects the degree of scattering. This makes the comparison of reported values difficult, and care should be taken while doing so. However, the sensitivity of the THz spectroscopy to the inclusion of air makes it a potential tool to study porosity and density of pharmaceutical tablets [99], which is one of the applications of THz spectroscopy in the pharmaceutical setting.

The focus of THz spectroscopy applications in the field of pharmaceutics lies on the inspection of solid oral dosage forms, in particular tablets. This is not surprising, since the marketed drugs are most commonly formulated as solid oral dosage forms (65 % - 70 %) [1,2], with tablets being the most popular [100]. In general, pharmaceutical applications of THz spectroscopy can be divided into the following categories: investigation of the solid state of the APIs, investigation of tablet coatings, and investigation of tablet porosity. In the following subsections an overview of the individual categories is briefly presented, starting with the solid state of the APIs.

2.2.1 Solid state of the APIs

Probing solid APIs with THz TDS is conceptually similar to the more familiar infrared spectroscopy. However, the origin of the absorption features, which can be observed in the THz and infrared absorption spectra, is different. The absorption features in the infrared region are related to the intramolecular vibrations specific to the functional groups, whereas the absorption features observed in the THz range are mainly related to the intermolecular motions and intermolecular interactions [11–14]. This is the case especially for the low frequency part of the THz range, which is easily assessable with typical THz TDS systems. This means that for molecular crystals the absorption spectrum strongly depends on the crystalline structure and not only on the structure of the individual molecules. On the one hand, this makes THz TDS an excellent tool for the observation of changes in the crystalline structure (e.g., differentiation between polymorphs of the same API). On the other hand, it makes the interpretation of the absorption features more difficult since the crystalline structure plays an important role. For a proper interpretation and an assignment of absorption features to specific molecular motions advanced computational methods like density functional theory (DFT) and *ab initio* molecular dynamics (AIMD) are required [101]. Furthermore, such spectral assignment can provide new insights into the thermodynamic properties of crystalline substances [102]. More details on such computational methods and interpretation of THz solid-state spectra can be found in [103,104].

Despite the need of advanced computational methods for a proper interpretation of the molecular motions underlying the THz absorption spectra, THz TDS can be directly used for many applications in the pharmaceutical field. Common examples are identification of APIs, their polymorphs [16–19] and cocrystals [105,106] as well as differentiation between crystalline and the amorphous state of a substance [12,16]. It can also be used to quantify the crystallinity of an API [107–110] and to monitor or observe dehydration [111,112], crystallization [108,113,114] and even amorphization [115] processes. All this can be done without the need to assign the absorption features to the underlying molecular motions. As an example, the absorption coefficient of IM in two crystalline forms and in its amorphous state are shown in Figure 17.
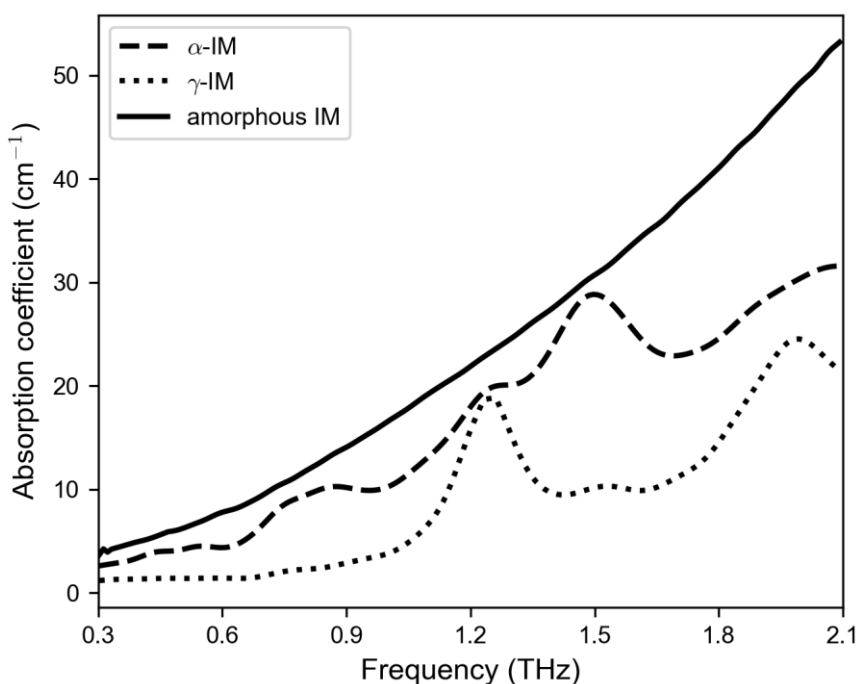
Figure 17. Absorption spectra of α, γ, and amorphous IM.

Comparing the absorption spectra of the different IM forms, one can first establish that the three forms can be distinguished from one another based on the THz absorption spectra shown in the above figure. The γ-form shows two pronounced absorption peaks, one at approximately 1.2 THz and the other at approximately 2 THz. A less pronounced peak can be observed at approximately 1.5 THz. In the case of α-form, the most pronounced peak is at 1.5 THz and less pronounced peaks can be observed at approximately 1.2 THz and a double peak at approximately 0.8 THz. Unlike the two crystal forms, the amorphous form shows continuous, featureless absorption, which increases with frequency in the shown spectral range. Such featureless, continuous absorption is universal for amorphous substances in this frequency range and it is related to the coupling of THz radiation into the vibrational density of states (VDOS) [20,101,115,116]. This characteristic of materials in the amorphous state enables a straightforward identification of crystal formation from the amorphous state given that the crystalline forms of the substance exhibit pronounced absorption peaks in the

investigated frequency range. The fact that many pharmaceuticals show pronounced absorption peaks in the THz frequency range makes THz TDS an attractive method to inspect, whether an API is in its amorphous or in one of the crystalline forms. This is also the essence of this work as it will be shown later.

Not only is THz TDS capable of distinguishing between amorphous and crystalline state of an API, it can also be used to study the temperature dependent relaxation processes of the amorphous materials, which seem to be related to a universal change in the hydrogen bonding structure [116]. Furthermore, it has been shown that it is possible to determine and predict stability of the amorphous state in this way [117,118]. Talking about the stability of the amorphous state might first sound surprising as amorphous state is intrinsically unstable. Therefore, it should rather be considered in the frame of stability of amorphous drugs in sense of predicting the crystallization of the API from its amorphous state. Crystallization of an amorphous drug during the shelf life would affect the properties of the drug as well as its bioavailability, which could limit the effectiveness of the drug and cause unsatisfactory patient treatment.

On the final note to this subsection, it is worth stating that the majority of measurements is performed in transmission when investigating the solid state of the APIs. In the following subsection the application of THz reflection measurements for investigation of tablet coatings is discussed.

2.2.2 Tablet coatings

The investigation of tablet coatings directly followed the initial focus on the solid state of the APIs as a potential application of THz TDS in a pharmaceutical setting. In 2005 Fitzgerald et al. were first to demonstrate the applicability of THz TDS for non-destructive investigation of tablet coating thickness [94]. The principle relies on the pulsed nature of THz TDS which can be exploited for identification of individual layers within a multilayered sample (e.g., coated tablet) when measured in reflection geometry (see subsection 2.1.3) and is also referred to as TPI. Shortly after the first demonstration, a dedicated system for mapping the coating thickness across the whole surface of the solid oral dosage forms was developed [95]. The key component of this system was a robotic arm in combination with a laser gauge, which enabled scanning of the surface of differently shaped tablets while ensuring the correct angle of incidence and positioning of the sample surface into the focal plane of the probing THz beam. The mapping of the whole tablet could be performed in 20 – 50 min. Furthermore, an identification of buried structure and chemical mapping was demonstrated using this system [119]. The axial spatial (i.e., in-depth) resolution limit of the system was estimated as 30 µm, mainly limited by the pulse width, whereas the lateral resolution was estimated to be 150 µm at 2.7 THz. These resolution limits can be considered common for conventional THz TDS systems, as similar resolution limits were reported in different publications [120].

In the following years much work has been done on the investigation of tablet coatings using TPI. Besides working on the determination of the coating thickness and its uniformity on a single tablet, focus was also on the inter-tablet coating uniformity and coating thickness variation [121,122], detection of defects in the coatings or in the tablet structure [123–125] as well as on the drug release performance related to the tablet coating [126–128]. Furthermore, there have been demonstrations of in-line investigation

of the tablet coatings using TPI [129–131]. It has been demonstrated that by combining TPI and optical coherence tomography (OCT), the coating thickness can be accurately determined over a greater thickness range, where the OCT performs better for thinner coatings (<50 µm) and THz TDS for thicker coatings [131,132]. A comparison of coating thickness evaluation between TDI and x-ray microtomography, revealed that TPI is a robust technique for direct measurement of coating thickness since refractive index of the coating material, which is needed for the thickness evaluation when using TPI, varies less than 3 % within the same tablet and less than 4 % among different tablets [133]. Since TPI can directly measure the coating thickness, it could be used as a reference and for calibration when employing other indirect techniques for coating thickness measurements (e.g., near infrared spectroscopy, Raman spectroscopy) [120].

The tablet coatings can be classified into three groups depending on their role [134]. Non-functional coatings mainly affect the appearance of the tablet, facilitate the intake of the drug and can protect the API from environmental influences. Functional coatings can be designed for example to affect the release of the API (e.g., prolonged release formulations) or to modify the taste or smell of the product. These two groups do not contain an API in contrast to the third group of active coatings containing an API. Especially in the case of functional and active coatings, the coating quality is of high importance. Defects as well as varying and non-uniform thickness can affect the performance of the drug. Therefore, different techniques including TPI are being considered to become part of the process analytical technology (PAT) for non-destructive, in-line monitoring and control of the tablet coatings. More detailed reviews about the work done on coating investigation of pharmaceutical tablets using TPI can be found in the articles reviewing this topic in its early as well as its more recent stage [120,135,136].

TPI has been also used to observe the liquid transport and swelling during the tablet disintegration [137,138]. Tablet coatings can be used to modify the disintegration properties of a tablet. Porosity of a tablet is another important property which also affects the disintegration of the tablet as well as its dissolution performance. In the following subsection the measurement of tablet porosity using THz TDS in transmission geometry is presented in more detail.

2.2.3 Tablet porosity

Tablets are typically prepared by compressing and coating the API with excipients. As a result, small voids or pores of air are present in the tablets and the amount of air in a tablet is described by the porosity. Porosity is an important property of tablets as it plays an important role in the disintegration of tablets, which also affects the dissolution characteristics of the dosage form [139–142]. Furthermore, porosity also affects the THz radiation propagating through the tablet. In 2008 Juuti et al. observed that the ratio between the tablet thickness and the time delay of the THz radiation propagating through the tablet as a function of the compression force correlates with the porosity of the tablet as a function of the compression force [143]. Parrott et al. focused on the accurate evaluation of refractive index and absorption coefficient of compressed powders into tablets by using effective medium theory approach and realized that measuring the effective refractive index of a tablet can be used to estimate its porosity [99].

The first requirement to correctly determine the porosity of a tablet using THz TDS is to accurately retrieve the effective refractive index of the tablet [101], which can be performed by analyzing the data in the time or in the frequency domain [144]. The analysis in frequency domain with appropriate effective medium model was found to deliver most robust and accurate results. However, additional factors might influence the refractive index measurement and introduce an error if not considered correctly. For example, lensing effect and Gouy phase shift can affect the measurement depending on the thickness and shape (e.g., curved faceted tablets) of the tablet, density distribution within the tablet, and properties of the THz beam [69,101]. Additionally, tablets consisting of highly absorbing APIs or excipients in connection with the tablet thickness can cause problems since the measurements are mainly performed in transmission geometry. In the last decade an extensive investigation of porosity of pharmaceutical tablets using THz TDS focusing on overcoming these potential problems took place [101]. THz TDS has been successfully used to study porosity of tablets of different shapes (e.g., flat-faceted [145], biconvex [146]) as well as tablets consisting of different excipients and APIs [143,147–149]. Furthermore, different effective medium models have been considered and modified to improve the accuracy of porosity measurements and even predict the structural orientation of pores in a tablet [101,147,148].

THz TDS offers several advantages compared to other techniques used for investigation of tablet porosity. For example, mercury or helium porosimetry are destructive, time consuming and can only probe the pores which are connected to the surface of the sample [142]. Near infrared (NIR) and Raman spectroscopy have been used to study porosity of tablets in a fast and non-destructive manner [150,151]. However, only the surface porosity can be investigated [101]. X-ray microtomography and different nuclear magnetic resonance based techniques can be used for non-destructive examination of porosity and even pore size distribution, however, longer measuring times compared to THz TDS are needed [142]. Since THz TDS has proven to be a fast, non-destructive, and robust measurement technique of bulk porosity, it could be used as a PAT-tool for on-line drug release testing of tablets based on the determination of their porosity [152,153].

A more comprehensive overview of porosity measurements of pharmaceutical tablets using THz TDS can be found in a recent review article by Lu et al. [154]. Further details about the measurement procedure can be found in a tutorial by Bawuah et al. [144]. To conclude, inspecting porosity of pharmaceutical tablets is important as it is directly related to the disintegration of and drug dissolution from the tablet. This in turn affects the bioavailability of APIs and, therefore, also the patient treatment. In the following chapter bioavailability of APIs and ways to improve it are discussed in more detail.

3 Solubility and bioavailability of pharmaceuticals

For an API to have the desired pharmacological effect it must reach the site of action after it is administered. There are different ways to administer a drug with oral administration being the most common one [3]. Orally administered drugs are mainly designed to get absorbed in the GI tract with some exceptions (e.g., antidiarrheals for the treatment of the intestine). In the scope of this work the term oral administration of a drug is limited to the drugs designed to be absorbed in the GI tract, which can occur only if the API is dissolved [4]. This means that after the oral administration of a drug, the dissolution of the API in the GI tract is required before it can permeate into the systemic circulation through which it is then delivered to the site of action. The rate and the extent of an API being absorbed into the systemic circulation defines its bioavailability [155]. This in turn means that poor aqueous solubility of an API can substantially limit its bioavailability and therefore the efficiency of the treatment. The United States Pharmacopeia (USP) defines seven different degrees of solubility ranging from very soluble to practically insoluble. These are listed in Table 1 with the corresponding criteria.

Table 1. Solubility definition according to USP. Adopted from [6] and [156].

Degree of solubility	Parts of solvent required per part of solute	Solubility range (mg/ml)
Very soluble	Less than 1	More than 1000
Freely soluble	From 1 to 10	100-1000
Soluble	From 10 to 30	33-100
Sparingly soluble	From 30 to 100	10-33
Slightly soluble	From 100 to 1000	1-10
Very slightly soluble	From 1000 to 10,000	0.1-1
Practically insoluble	More than 10,000	Less than 0.1

A definite and API independent solubility value at which the solubility starts to limit the bioavailability of an API is difficult to determine since further factors (e.g., the dose and permeation of the membrane in the GI tract) affect the overall bioavailability of an API. In 1995 Amidon et al. proposed a theoretical basis for biopharmaceutics classification system (BCS), which divides APIs into four classes based on their aqueous solubility (i.e., high or low solubility) and intestinal permeability (i.e., high or low permeability) as shown in Figure 18 [4]. The definition of the solubility within the scope of the BCS takes the dosage of the drug into account. An API is considered highly soluble, if the highest therapeutic dose of the API can be completely dissolved in 250 ml or less of aqueous media [157]. Furthermore, this criterium should be met across a broad physiological pH range (i.e., 1.2–6.8) at a temperature of 37°C [158]. An API is considered highly permeable, if at least 85 % of the administered dose is recovered mostly unchanged in urine [158].
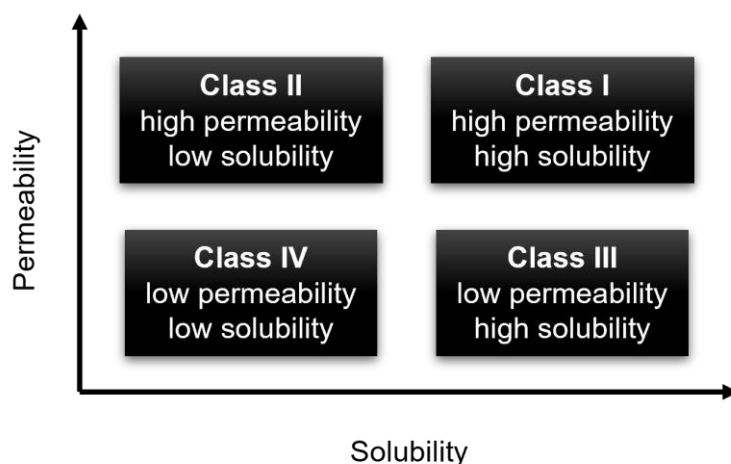
Figure 18. The four classes according to the BCS.

The fundamental idea of the BCS was to establish a framework for biowaivers based on the correlation between *in vitro* dissolution properties and *in vivo* bioavailability of a drug product. This way potentially unnecessary *in vivo* studies can be avoided, and the process of drug development and approval simplified. In 2000 the US Food and Drug Administration (FDA) introduced a guidance for industry on the BCS based biowaivers, which resulted in more than 160 applications being granted until 2017 and saving the pharmaceutical industry $100 million [157]. Similar guidance was adopted by other agencies such as the European Medicines Agency (EMA) and the World Health Organization (WHO) [157]. The initial guidance for BCS based biowaivers considered only class I drugs eligible. The guidance was modified over the years and recently also extended to the BCS class III drugs [158]. Furthermore, a division of BCS class II drugs into subcategories has been proposed with the possibility of expanding the BCS based biowaivers to some of them [159].

This work focuses on poorly soluble pharmaceuticals, which means that BCS class II and class IV drugs are mainly of interest. In Table 2 the distribution of marketed drugs and drugs under development (i.e., drug candidates) among the four classes of BCS are listed. 40 % of the marketed drugs are estimated to be poorly soluble, which means that improving their solubility could have positive effects on their bioavailability. This is especially relevant for the class II drugs, which show low solubility but high permeability (see Figure 18) and are estimated to present 30 % of the marketed drugs. The estimated percentage of newly developed drugs belonging to BCS class II is even higher exceeding 60 %. Considering also the estimated percentage of drug candidates belonging to BCS class IV, in total more than 70 % of drugs being developed is expected to exhibit poor aqueous solubility. This can be accounted to the fact that the new APIs should be able to bind to cell receptors, which often involves hydrophobic interactions and therefore lipophilic candidates are more commonly considered for the development [5]. This means that poor solubility could substantially hinder bioavailability of new drugs and as such poses an obstacle for their development.

Table 2. Percentage distribution of marketed drugs and drug candidates (i.e., APIs under development) between the four BCS classes. Adopted from [5].

BCS class	Marketed drugs (%)	Drug candidates (%)
I	35	5-10
II	30	60-70
III	25	5-10
IV	10	10-20

It is worth pointing out that several estimations on the percentage distribution of drugs among the four BCS classes exist [156,160–162] These were made in different years after the BCS was designed and by considering different sets of drugs in the analysis. Therefore, some deviation in the reported percentage can be observed. However, it is common to all such reports that less than the half of the marketed drugs are classified as either class II or IV (i.e., poorly soluble). Furthermore, class II drugs present less than one third of all marketed drugs and the percentage of class II drugs exceeds that of class IV drugs. When it comes to drug candidates, it can be considered that the estimated percentage would deviate more and be less reliable. Nevertheless, it seems safe to state that most newly developed drugs and drug candidates are poorly soluble [6,163,164].

Since many APIs exhibit poor aqueous solubility, which can substantially limit their bioavailability, different approaches for improvement of solubility are being considered. Before presenting the most common strategies for solubility improvement, the basics of API dissolution, solubility and absorption, and dissolution rate in the GI tract are described in the following sections.

3.1 Dissolution

Dissolution of a solute in a solvent can be simplistically described as a three-step process as depicted in Figure 19 [165]. In the first step, a molecule of the solute needs to be extracted from the solid particle, which involves breaking solute-solute interaction. In the second step, a void in the solvent for the molecule of the solute must be induced, which requires breaking of the solvent-solvent interaction. In the third step the solute molecule fills the void in the solvent forming solute-solvent interaction. In the first and the second step energy is required to break the solute-solute and solvent-solvent bonds and in the third step the energy is released. Commonly the solvent-solvent bonds are much weaker compared to the solute-solute bonds. Therefore, the energy required in the second step can be neglected. This means that dissolution depends mainly on the energy difference between the solute-solute and solute-solvent interactions.

From this simple description of the dissolution process two important aspects affecting solubility of a solute in a particular solvent can be deduced. First, for dissolution to take place, solute-solvent interaction must be energetically favorable, which is common for molecules with similar properties (e.g., polar solutes dissolve well in polar solvents). This

concept is often referred to as "like dissolves like". The second aspect is the importance of the solute-solute interactions in the solid API for its solubility. The interactions depend on the solid state of the solute. For example, different arrangement of the molecules in the crystal lattice (e.g., polymorphism) or lack of long-range order (amorphous state) exhibit different intermolecular interactions. Therefore, certain solid states of an API exhibit higher solubility. How solubility affects the absorption of an API in the GI tract is described in the following section.
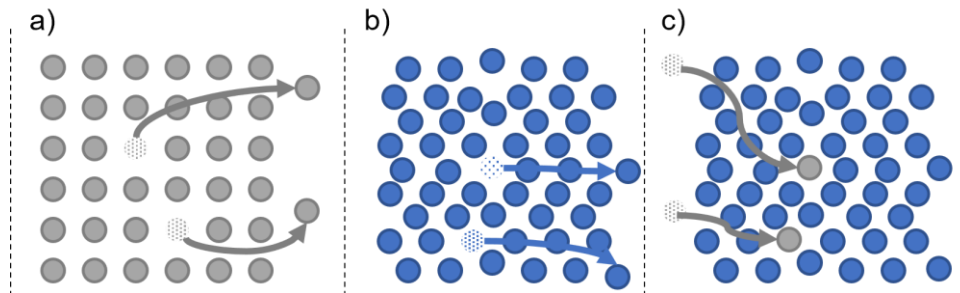

Figure 19. Graphical representation of the dissolution as a three-step process. a) Solute molecules are extracted from the solid lattice. b) Solvent molecules are removed from the solvent network leaving a void for the incorporation of the solute molecules into the network. c) Incorporation of the solute molecules into the solvent network (i.e., solvation). Adopted from [165].

3.2 Solubility and absorption

To better understand when solubility limits bioavailability, first the API dissolving in the GI tract should be considered. A mass flux (J) of API molecules dissolved in the intestinal fluid across the absorptive membrane per surface area of the membrane in the GI tract can be written as [165]:

$$J = \frac{D\,K}{h}(C_m - C_0),$$ 3.1

where C_m is concertation of the API on the absorptive side of the membrane, C_0 is the concentration of the API on the other, abluminal side of the membrane, h is the width of the diffusion layer, D is the diffusion coefficient of the drug in the membrane, and K is the partition coefficient between the membrane itself and the API solution overlaying the membrane. By assuming that C_m is much greater than C_0 and that it equals the equilibrium solubility (C_s), the above equation can be rewritten as:

$$J = PC_s,$$ 3.2

with

$$P = \frac{D\,K}{h}$$ 3.3

being the permeability coefficient of the membrane. Equation 3.2 reveals that the flux does not only depend on the solubility but also on the permeability of the membrane as already discussed at the beginning of this chapter. Furthermore, absorption rate (AR) at

any given time can be obtained by integrating the flux in equation 3.2 over the entire surface area (*S*) of the absorption membrane [4]:

$$AR = \frac{dm}{dt} = \iint PC_s \, dS,$$

3.4

where *m* is mass and *t* is time. Furthermore, the total mass (*M*) of the absorbed API at time t_a after the drug administration can be obtained by integrating the absorption rate:

$$M = \int_0^{t_a} AR \, dt = \int_0^{t_a} \iint PC_s \, dS \, dt,$$

3.5

If C_s is assumed to be homogenous across the whole small intestine as well as time invariant, maximum absorbable dose (M_{max}) in the small intestine can be estimated as:

$$M_{max} = C_s \, k_{abs} \, V_0 \, t_{transit},$$

3.6

where $t_{transit}$ is the small intestine transit time, V_0 is the small intestine water volume, and k_{abs} is the API specific absorption rate constant [166]. $t_{transit}$, and V_0 are typically assumed to be 270 min (i.e., 4.5 hours), and 250 ml, respectively, whereas k_{abs} is related to the permeability (*P*) of the membrane [165]. This expression allows to estimate the minimum solubility of an API (C_{min}), which is required to absorb the administered dose at a given absorption rate. Figure 20 shows minimum solubility for different dose and absorption rate values.
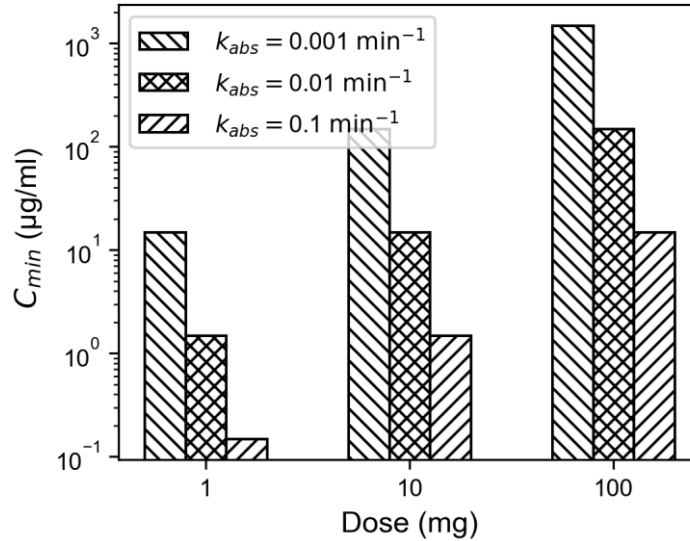
Figure 20. Minimum API solubility required to absorb the desired dose of an API. The k_{abs} values of 0.001, 0.01, and 0.1 min-1 can be related to low, medium, and high permeability, respectively [165]. Adopted from [165].

From Figure 20 it becomes evident that the required minimum solubility increases with the increasing dose and the decreasing absorption rate. This means that for low potency drugs and drugs with lower permeability, higher solubility is required to achieve sufficient bioavailability of the drug. For given absorption rate and dose values in Figure 20, the required minimum solubility is around 1 mg/ml or lower. This reveals that also slightly

43

soluble, very slightly soluble, and practically insoluble drugs according to the USP (see Table 1) might still have sufficient solubility if the required dose is small enough and the absorption rate is high enough. Considering a required dose of 10 mg and medium absorption rate (i.e., 0.01 min^{-1}), which can be considered realistic for a non-steroidal ant-inflammatory drug NIF [166], the required minimum solubility is around 10 µg/ml, which fits the reported experimentally determined solubility values [167]. This means that NIF, despite being BCS class II drug (i.e., poorly soluble), has sufficient bioavailability for the design dose, which is reasonable, since otherwise a drug would not be approved in the first place.

The estimation of when solubility becomes a limiting factor based on equation 3.6 are strongly dependent on the correct assessment of absorption rate values of an API in the small intestine, which are challenging to determine and the error of values in the literature could be one order of magnitude [166]. Furthermore, this assessment assumes that the concentration of the drug dissolved in the small intestine is constant and equal to the equilibrium solubility. This assumption and therefore also the estimated minimum solubility can become questionable for drugs with low dissolution rates. The dissolution rate of an API is described in the following section.

3.3 Dissolution rate

Dissolution rate of a drug is a rate at which an API passes into a solution from the administered formulation. Its relevance is especially high in the case of oral administration due to the limited transit time through the intestine. To achieve optimal absorption, the dissolution rate must be significantly greater compared to the rate of transit through the intestine [165]. The underlying mechanism affecting the drug dissolution rate can be explained by considering a solid drug particle dissolving in a well stirred aqueous medium as shown in Figure 21.
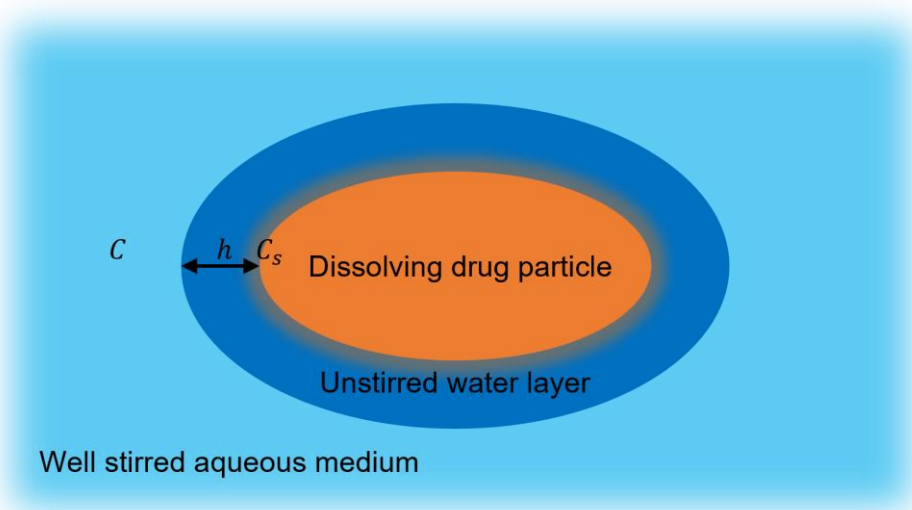

Figure 21. A sketch showing a drug particle dissolving in an aqueous medium surrounded with a layer of unstirred water of thickness h. C_s is the maximal concentration of the drug at the surface of the dissolving particle and C is the drug concentration in a well stirred aqueous medium. Adopted from [165].

In 1897 Noyes and Whitney proposed an equation describing the dissolution rate of a drug based on their experimental observations [168]. The equation, which bares their name (i.e., Noyes-Whitney equation), was subsequently modified by including the surface area of the exposed solid drug (S_d) and the thickness of the unstirred water layer surrounding the surface of the solid drug:

$$\frac{dC}{dt} = \frac{DS_d}{h}(C_s - C),$$
3.7

where D is the diffusion coefficient of the solute in the solution, C_s is solubility of the dissolving solid drug, C is the drug concentration, and the term on the left side of the equation is the dissolution rate. Considering drug concentration being much smaller than the drug solubility (e.g., sink conditions or directly after the drug administration) the dissolution rate becomes directly proportional to the solubility [169]. This means that by improving the solubility of an API the dissolution rate is also improved. Furthermore, the Noyes-Whitney equation reveals that the dissolution rate can be increased by increasing the surface area of the solid drug. Increasing the surface area of drug particles, which is commonly achieved by particle size reduction, is one of the strategies for improving solubility or solubility rate limited bioavailability of pharmaceuticals. In the following section the most common solubility improvement strategies are shortly presented.

3.4 Solubility improvement strategies

Since the majority of new drug candidates are expected to be poorly soluble, solubility studies take place already in the early development stage of a new drug candidate. Furthermore, different solubility improvement strategies are commonly considered and applied throughout the drug development process to ensure well characterized and sufficient solubility before performing *in vivo* studies on humans [6]. Choice of solubility improvement strategy depends also on the type of drug administration, which can vary throughout the development process and can be different for the final product. For example, *in vivo* tests on animals (e.g., rats, dogs) often require parenteral drug administration (e.g., intravenous) since oral administration can be troublesome. This means that also different solubility improvement strategies are considered at this stage compared to the solid drug formulations for oral administration, which might become the route of administration for the final product [165].

In the early stage of the drug discovery the amount of the new drug is limited and the focus lies mainly on the assessment of the drug efficacy. Therefore, the use of simple solutions is preferred in the early development stage, also in the case of oral administration, to avoid different complexities (e.g., solid-state properties of the drug) affecting the dissolution and solubility of the drug. The commonly applied strategies include pH adjustment of the solution, usage of cosolvents, surfactants, complexation agents (e.g., cyclodextrins), lipid formulation, and particle size reduction as well as their combinations. These techniques are relevant also in later development stages as well as when designing the final formulation. More details on these strategies can be found in a comprehensive review paper by Williams et al. [165]. At the later development stages as well as for the design of the final drug formulation further techniques are considered. These include solid dispersions and engineering of the solid state of the drug (e.g.,

polymorphs, cocrystals, amorphous drugs), which will be discussed in more detail in the following subsection, since they are particularly relevant for this work.

3.4.1 Solid-state engineering

The solid state of an API can importantly affect the solubility of an API, its dissolution rate, and consequently its bioavailability. The key idea is to modify the arrangement of the molecules in the solid in such a way that weaker interactions between the molecules are achieved. This enables easier breaking of the solute-solute interactions in the solid and facilitates the drug dissolution (see section 3.1). Such solid forms of a drug are often described as higher-energy forms or states of an API, where high energy refers to the thermodynamic instability [165]. Although this instability causes the improved solubility, it is also important to realize that it can cause problems in the design of the final dosage form. The main concern is the transformation of such high-energy forms, which are instable or metastable, into a more stable form during the shelf-life of the drug. Such unwanted transformation can cause insufficient patient treatment due to the modified solubility of the drug. Indeed, in the late 1990s such a problem occurred with a marketed product containing ritonavir, as crystallization into a more stable form with lower solubility, which was unknown beforehand, took place during the shelf-life. As a consequence the product had to be recalled and reformulated [170].

Modifications of the crystalline structure are one of the approaches of solid-state engineering, which include polymorphs, solvates and hydrates, and cocrystals. Polymorphs are crystal forms of the same chemical structure with different arrangement of the molecules in the crystal unit cell. Solvates include molecules of a solvent in their crystal lattice, which means that their chemical structure differs. Hydrates are a special type of solvates with water molecules in the crystalline structure. Cocrystals like solvates have a modified crystalline structure, which includes the target API and a coformer. The difference is that solvents are typically not considered to be coformers. Coformers can be pharmacologically neutral ingredients or APIs, which are different from the target API. As such, solvates and cocrystals in particular are additional possibilities to polymorphs, which rely on the modification of the crystalline structure. The aim is to obtain better solubility and bioavailability of a poorly soluble API with sufficient stability of the formulation at the same time [165].

In addition to the modification of the crystal lattice, solid-state engineering includes amorphization of the drug. In contrast to crystals, whose structure can be described as a simple translation of a unit cell, the amorphous substances lack this kind of a long-range order. Amorphous substances are considered to generally exhibit better solubility compared to the crystalline forms [7,171]. However, again one major concern is the high instability of the amorphous state which can lead to recrystallization into a more stable crystalline form with lower solubility and lower bioavailability during the shelf-life [165]. Therefore, different approaches to ensure sufficient stability of amorphous drugs are considered. Co-amorphous systems are one of such approaches, which are made from two or more small molecules forming a single amorphous phase with increased stability of the formulation and solubility of the API [172]. Furthermore, in the case of carbamazepine, it has been shown that the amorphous drug resulted in a lower solubility compared to the crystalline form, which is considered stable at normal, storage conditions. The reason for this unexpected outcome, was the fact that at higher

temperatures (37 °C) and in aqueous medium even a more stable dihydrate form of carbamazepine with even lower solubility exists. Amorphous carbamazepine directly converted into this dihydrate form during the solubility experiments, which were conducted at 37°C in an aqueous medium mimicking the conditions in the GI tract. This in turn led to the reduced measured solubility of the amorphous carbamazepine compared to the commonly used crystalline form.

One further concern when using high-energy forms (e.g., metastable polymorphs, amorphous drugs) is the precipitation and recrystallization of the drug from the solution into the more stable crystalline form after the drug administration. This reduces the concentration of the dissolved drug and therefore its absorption. It is expected that after a certain time the concentration of the drug will reduce when using such high-energy forms and eventually become equal to the solubility of the most stable crystalline form. However, the transient increase of the concentration in the GI tract leads to a transient increase of the API concentration in the blood and, therefore, a higher total absorption of the API [165,173]. Nevertheless, inhibiting precipitation and crystallization after the drug administration can further increase the absorption of a drug and is, therefore, of interest. Solid dispersions, which are discussed in more detail in the following subsection, can be used for combining the advantage of an amorphous API and the inhibition of crystallization during storage as well as after administration.

3.4.2 Solid dispersions

Solid dispersions are formulations which consist of an API dispersed in a carrier. Commonly used carrier materials are polymers such as polyvinylpyrrolidone (PVP), polyethylene glycol (PEG), hydroxypropyl methylcellulose (HPMC), and hydroxypropyl methylcellulose acetate succinate (HPMCAS). Solid dispersions are commonly produced by melting and mixing the carrier material with the drug (e.g., hot-melt extrusion) and by using solvent evaporation techniques. Solid dispersions can be classified into different types based on the solid state of the carrier (i.e., crystalline or amorphous) and based on the arrangement of drug molecules in the carrier. On the one hand, the drug molecules can form particles within the carrier which can be either crystalline or amorphous. On the other hand, the drug can be molecularly dispersed within the carrier (i.e., solid solution). In this case the drug is amorphous, however, its molecules do not form particles. For different types of solid dispersion different mechanisms of solubility enhancement can be expected. For crystalline particles within the matrix the main advantage is the particle size reduction which facilitates the dissolution rate due to the increased total surface area (see equation 3.7). In the case of amorphous particles or a molecularly dispersed drug, an increased solubility is expected due to the weaker interactions between the drug molecules (see section 3.1) in addition to the reduced particle size. For a molecularly dispersed drug the maximum area for hydration is obtained, which additionally increases the drug release rate [165].

For solid dispersions containing amorphous APIs the greatest bioavailability enhancement can be expected. However, as discussed, in the case of solid-state engineering (subsection 3.4.1), drugs in amorphous state are unstable and tend to convert into a more stable crystalline form. The crystallization of an amorphous drug during the shelf-life is the main concern when using amorphous formulations. In the case of solid dispersions, it is expected that the drug remains in its amorphous state over a

longer period, as the molecular mobility is reduced by the carrier. One further advantage of solid dispersions is that once the formulation is dissolved and the concentration of the drug exceeds the solubility of the stable crystalline form, the carrier can inhibit nucleation and crystal particle growth. This way the concentration of the dissolved drug can be maintained at an increased level (i.e., exceeding the solubility of the stable crystalline form) for longer time which results in a better absorption of the drug and therefore an increased bioavailability [165].

In addition to the described types of solid dispersions, formulations involving porous materials can be considered as one further, however, unconventional type of solid dispersions [165]. Such formulations are commonly prepared by impregnation of the solid porous carrier with the solution containing the drug [174]. After the solvent evaporates, the drug molecules adsorb to the surface of the carrier. This way the drug remains amorphous which leads to an increased solubility and bioavailability of the drug. Selection of materials containing networks of nano- and microsized pores and capillaries leads to high surface areas (>500 m²/g) of the material and consequently high drug loading in the amorphous form. An example of widely considered carrier material is mesoporous silica [175]. Again, the physical stability of the amorphous drug during shelf-life as well as precipitation and crystallization after drug administration remain the challenging factors [165].

Another example of a porous material is paper (e.g., coffee filter paper). Therefore, it can be considered as a porous carrier for production of amorphous solid dispersions. SmartFilms® encompass this idea. They are presented in the following subsection in more detail since the focus of this work lies within the applicability of THz TDS for the inspection of the solid state of drugs loaded into smartFilms.

3.4.3 SmartFilms®

SmartFilms® are a novel formulation for improving solubility of poorly soluble drugs, which relies on the solubility advantage of amorphous APIs. SmartFilms can be made from conventional paper films (e.g., tissue paper, coffee filter paper) with density between 0.1 and 2 g/cm³, crystallinity index between 1 and 200, capability to intake water between 10 and 2000 % (m/m), water content between 1 and 20 % (m/m) and pores with diameter between 1 and 200 µm [8,9]. Such paper films are soaked with a drug dissolved in a solvent. After the solvent evaporates, the drug remains loaded into the paper matrix in its amorphous state. Figure 22 schematically shows how smartFilms can be prepared on a laboratory scale.

First the selected sheet of paper is cut into pieces of smaller size which are easier to handle and a stock solution with a specific concentration of the selected drug is prepared. Then the solution is applied onto the paper and the paper is left to dry. After the paper is dry, the solution can be applied to the paper again to increase the amount of the drug loaded in the smartFilm. These loading cycles can be repeated until the desired content of the drug in the smartFilm is achieved.
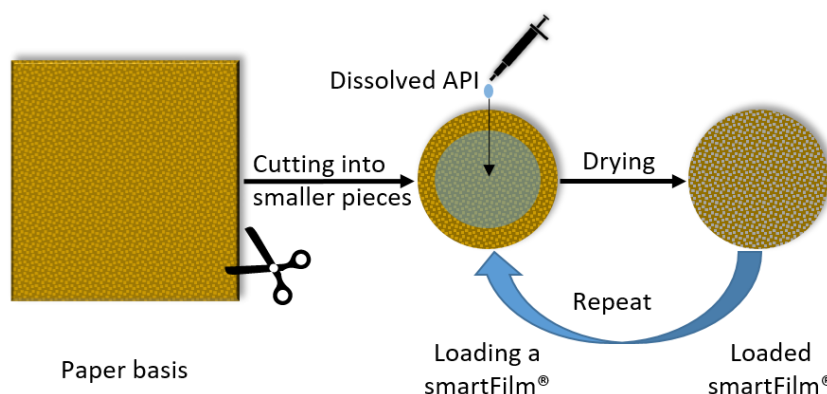
Figure 22. Manual production of smartFilms on a laboratory scale. Adopted from [176].

The amount of drug loaded into the paper matrix in a single cycle is determined by the concentration of the solution and the volume applied. The volume is typically selected in a way that the whole paper gets wet. The volume should be selected carefully to avoid solution dropping from the paper. This way the amount of the drug loaded per cycle equals the concentration of the solution multiplied by the applied volume. The actual mass loaded can be further controlled by weighing the paper before and after the loading once the solvent completely evaporated.

The drying of the soaked paper can take place in a fume hood at room temperature. Alternatively, the drying process can be accelerated by elevating the temperature during drying. However, exposing smartFilms to higher temperatures during drying might influence the amorphousness of the loaded drug. The time it takes to dry also depends on the solvent used. Typically, organic solvents such as ethanol, methanol, and acetone are used. It is important that the drug is sufficiently soluble in the selected solvent and that the solvent completely and readily evaporates after being soaked by the paper.

In addition to the straightforward production of smartFilms, another advantage of smartFilms is the possibility to easily convert them into tablets. This is done by first cutting the smartFilms into smaller pieces which more easily fit a tablet press and then pressing them into a tablet. The tablets obtained this way meet the requirements of the European Pharmacopoeia in terms of mass and content uniformity, resistance to crushing and friability [177]. Alternatively, smartFilms can be first milled to obtain a fine powder before pressing the tablets. In a proof-of-principle study [178] smartFilms were loaded with rutin, milled into a powder with median particle size of 86.5 µm and then pressed into tablets. X-ray diffractometry (XRD) as well as differential scanning colometry (DSC) confirmed that rutin remained amorphous after milling. Furthermore, tablets pressed from powder showed higher dissolution rate compared to the tablets pressed directly from smartFilms [178]. One further alternative to prepare an oral dosage form with smartFilms is to fill smaller pieces of smartFilms into capsules. Recently, a different approach of drug delivery involving smartFilms was investigated by Eckert et al. [179]. In this study smartFilms loaded with amorphous curcumin were used for improvement of dermal penetration efficacy of curcumin. *Ex Vivo* investigation on porcine skin revealed that curcumin loaded into smartFilms could efficiently permeate into the *stratum corneum*. Furthermore, an improved penetration into deeper layers of the skin could be observed

compared to other formulations (i.e., bulk suspension, diluted bulk suspension, nanocrystals, and diluted nanocrystals).

Despite several demonstrations that smartFilms maintain the API amorphous, the exact mechanism how this is achieved is not completely understood yet and it is part of an ongoing research. Considering that paper consists of pores and fibers of cellulose, which increase the available surface for adsorption of the drug, smartFilms can be considered another special type of solid dispersions. As such, different factors can contribute to maintaining the drug amorphous. One could imagine that pores physically limit the formation of crystals due to the limited available space. However, this is unlikely due to the relatively big pore size. It is more likely that the interactions of the drug molecules with the paper matrix reduce the mobility of the drug molecules which inhibits crystallization. Furthermore, effectively dispersing the drug molecules throughout the whole paper matrix could prevent the drug molecules from interacting directly with one another. Therefore, the probability of forming even amorphous particles, which could convert into crystalline particles, is reduced. However, by increasing the amount of drug molecules in the paper matrix, the likelihood for direct interactions between the drug molecules increases. Therefore, it can be expected that smartFilms maintain the drug in its amorphous state only until a certain drug content.

The stability of the formulation in sense of drug amorphousness over a long enough period remains the main concern. To address this concern, appropriate analytical methods are required, which preferably also enable testing of the final dosage form (e.g., tablets) in a non-destructive way. THz TDS is a non-destructive technique which can be used to differentiate crystalline forms from amorphous state for many substances and even quantify the degree of crystallinity (see subsection 2.2.1). Therefore, THz TDS is a good candidate for this task. The potential of THz TDS for the non-destructive inspection of the solid state of APIs loaded into smartFilms is presented in the following chapters.

4   Feasibility of THz TDS for the investigation of smartFilms®

The goal of the first THz TDS investigations regarding smartFilms was to determine if such investigation is feasible at all. For this purpose, L-(+)-tartaric acid (LTA, Carl Roth GmbH + Co. KG, Germany) was chosen as a model substance for loading the paper films since it is a well-studied chemical in the THz range, which exhibits a strong absorption peak at around 1.1 THz when in its crystalline state (see Figure 23) [15,180–182]. Coffee filter paper (Filtertüte 1x6/40 naturbraun, Melitta Europa GmbH & Co. KG, Germany) was used as a paper film basis for the preparation of smartFilms, as it delivered promising results in previous studies of smartFilms and tablets made from them [177,178].
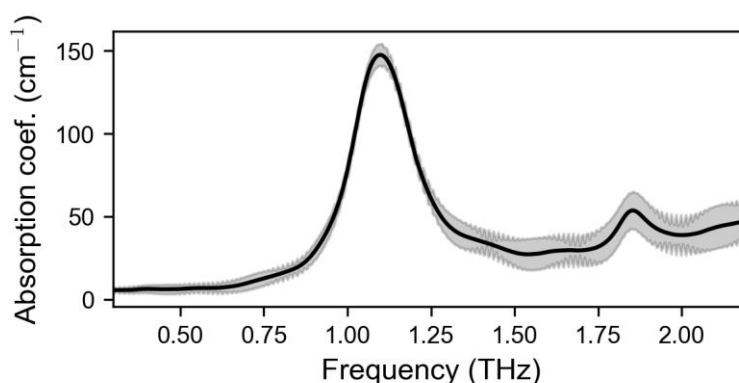

Figure 23. Absorption coefficient of LTA extracted by using the software TeraLyzer. 80 mg of LTA powder were pressed into a tablet using a manual hydraulic press (Model No. GF-10B Cl. 1.0, Enerpac, Germany) and applying force of 30 kN for 90 s. The resulting tablet had a diameter of 13 mm and thickness of approximately 0.35 mm and was investigated in transmission. The grey shaded area corresponds to the measurement uncertainty calculated based on repeated measurements.

For the THz investigation within this part of the work, a THz TDS system like the one shown in Figure 2 was used, however, with a modified laser beam path as fiber-coupled antennas were employed. Furthermore, a femtosecond fiber-laser (M-Fiber, Menlo systems GmbH, Germany) emitting short laser pulses (<100 fs) with a central wavelength emission at approximately 1550 nm was used. The emitted laser light was split into two parts using a fiber beam-splitter. One part was directly guided to the fiber-coupled emitter antenna. The other part of the laser beam was coupled out of the fiber and directed onto a retroreflector mounted on an optical delay line. The reflected beam was then coupled back into a fiber attached to the detector antenna. AC voltage was applied to the emitter and a Lock-in amplifier (SR830, Stanford Research Systems, USA) was used for the amplification of the detected signal. Polyethylene lenses were used to form the THz beam path for the transmission measurements.

The investigation on the feasibility of THz TDS for the investigation of smartFilms involving LTA presented in this chapter can be divided into two parts. The first part involves the preliminary investigation, whereas the second part involves a more comprehensive THz TDS investigation of smartFilms loaded with LTA as well as tablets made from them. Furthermore, it also includes a comparison with XRD investigation of the prepared smartFilms.

4.1 Preliminary investigation

In the first step, five circular pieces of paper with a diameter of approximately 93 mm were cut from the coffee filter paper basis. After the paper samples were weighted, they were individually mounted into the holder and then investigated in transmission geometry on six different areas of the sample as shown in Figure 24. Additionally, a reference measurement without the sample in the beam path was performed. This set of measurements was repeated ten times in an enclosed chamber with a constant inflow of nitrogen resulting in relative humidity not exceeding 4% at a temperature of approximately 20 °C. After the measurement of the unloaded paper sample (i.e., paper film without LTA) was done, the mounted sample was removed from the THz TDS setup. Then an LTA aqueous solution with a selected concentration was prepared and poured onto the paper, which was still mounted into the holder. The amount of the applied solution (i.e., 20 g) sufficed to completely soak the paper sample. The exceeding solution, which could not be absorbed by the paper, was drained off and the sample was inserted back into the beam path while still being wet. Then the measurements were performed on the same six areas of the sample with an extra reference measurement without the sample in the beam path. This measurement set was repeated 100 times, which exceeded ten hours. In this time the soaked water completely evaporated from the sample and the last ten repetitions, which were recorded several hours after the sample had dried, were used for further analysis. After the THz measurements were completed, the smartFilms were removed from the holder and weighted again.
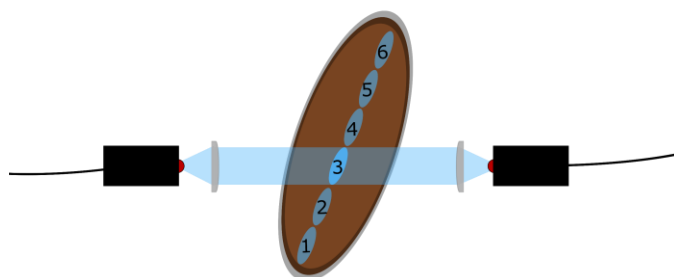
Figure 24. Filter papers were individually mounted into a metal holder and six different areas on the sample were repeatedly investigated with a collimated beam.

In total four LTA aqueous solutions with different concentrations (i.e., approximately 5, 10, 15, and 20 w%) were used in the experiment. The concentrations of the solutions and results of weighing the sample before and after the experiment with the corresponding loaded content of LTA are listed in Table 3. In addition to using LTA aqueous solutions to wet the filter papers, one paper sample was soaked with distilled water without any LTA dissolved in it (i.e., 0 w%, see Table 3). This control sample was used to estimate the time it takes for a sample to dry and to determine if wetting of the paper and subsequent evaporation of the water have an influence on the THz absorbance of the dried sample. The results of the investigation of the control sample are shown in Figure 25.

Table 3. Overview of the investigated samples. LTA aqueous solutions with four different concentrations of LTA as well as pure water were used to soak the paper samples. The mass of the samples before (m_1) and after the loading (m_2) were recorded (Libror EB-3300HW, Shimadzu Deutschland GmbH, Germany). The resulting mass difference (Δm) corresponds to the LTA loaded into the paper samples. The content of the LTA in the paper samples was calculated in terms of weight percentage (i.e., w%) and mg of LTA per unit area of the paper samples (i.e., mg/cm²). For the calculation of the latter, the area of the paper samples was determined to be 67.9 cm². Note that for pure water (i.e., C_{LTA} = 0 w%) the negative mass difference, which equals to the resolution of the scale used, confirms that no LTA was loaded into the sample and that the water completely evaporated during drying.

N	C_{LTA} (w%)	m_1 (g)	m_2 (g)	Δm (g)	LTA content (w%)	LTA content (mg/cm²)
0	0	0.46	0.45	-0.01	/	/
1	5.0	0.45	0.53	0.08	15.1	1.2
2	10.1	0.45	0.60	0.15	25.0	2.2
3	14.9	0.45	0.67	0.22	32.8	3.2
4	19.9	0.45	0.79	0.34	43.0	5.0

The transmittance (see equation 2.7) of the control sample during drying of the control sample was the smallest (i.e., approx. 10 %) at the beginning of the experiment when the amount of water in the sample was the greatest. This was expected since water strongly absorbs THz radiation [181]. With increasing drying time, the transmittance also increased and reached a plateau of approximately 85 %. This plateau was reached approximately after one hour, indicating that the sample was dry. The same behavior could be observed for all six investigated areas on the sample as shown in Figure 25 a). Furthermore, a comparison of the frequency dependent absorbance of the fresh paper sample (i.e., before wetting) and of the paper after wetting reveals that applying water to the paper sample and letting it dry did not have any significant effect on the absorbance of the THz radiation (see Figure 25 b)). Therefore, any significant difference in the absorbance of the fresh and loaded samples can be contributed to the LTA loaded into the paper matrix. The results for paper samples loaded with LTA are shown in Figure 26.

The transmittance of the samples during drying shown in Figure 26 a-d) increased in a similar way as in the case of the control sample (see Figure 25 a)). The time it took to reach the plateau differs among the samples. This could mean that the presence of LTA in the applied solution and its concentration might influence the drying dynamics of the paper. However, since the exact amount of water soaked by the paper and the time required between wetting the paper and starting the THz measurement were not systematically controlled, no reliable conclusions can be made about the dynamics of the drying process of the samples, which can be of interest for certain pharmaceutical applications [183]. Nevertheless, comparing the transmittance after the samples were dry reveals that the final transmittance is lower for samples soaked with more concentrated solutions. Such a result was expected since more LTA is deposited into the paper matrix when using more concentrated solutions, which additionally attenuates the THz radiation propagating through the sample. A similar conclusion can be made by observing the absorbance spectra shown in in Figure 26 e-h) and keeping in mind that lower transmittance means higher absorbance (see equation 2.7). For all samples an

increase in the absorbance across the investigated spectral range can be observed after the samples were loaded and dried. Furthermore, the samples loaded with a more concentrated solution revealed overall higher absorbance, which can be again attributed to a greater amount of LTA deposited into the paper matrix of the samples. By weighing the samples before and after the loading confirmed that the amount of LTA in the samples increased when using more concentrated solutions (see Table 3).
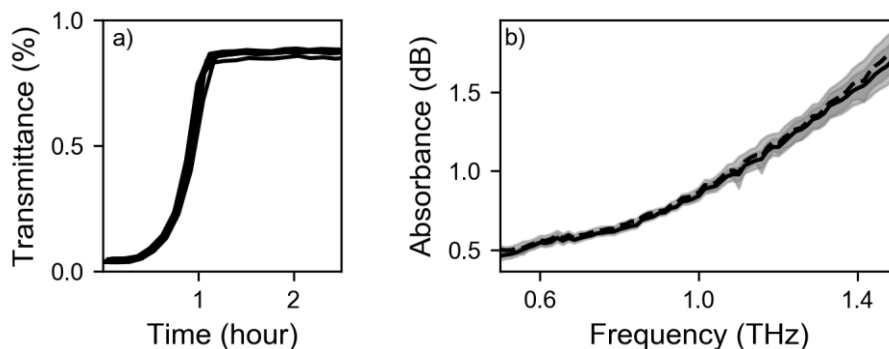

Figure 25. Investigation of the control sample (i.e., 0 w%). a) Transmittance in the frequency range between 0.6 and 0.8 THz of the six different areas on the sample (see Figure 24) in the first 2.5 hours of the measurement after the wetting. b) Average absorbance of the paper sample before wetting (dashed curve) and after the sample was completely dry (solid curve). The shaded areas correspond to the measurement uncertainty assessed based on the ten measurement repetitions.

The goal of this preliminary investigation was to determine based on the THz data whether the LTA loaded into the paper samples was in its crystalline or amorphous state. For this the absorbance spectra of the individual samples before and after loading, which are shown in Figure 26 e-h) were compared. On the one hand, for the highest loaded content of LTA (Figure 26 h)), a clear absorption peak at approximately 1.1 THz can be observed, which is characteristic for crystalline LTA. On the other hand, in the absorbance spectra for the lowest two LTA contents shown in Figure 26 e-f) no such absorption peak can be observed, which indicates that the LTA loaded into the paper matrix remained amorphous. In the case of the 15 w% solution (Figure 26 g)), a weak absorption peak at approximately 1.1 THz can be observed, which indicates that some part of LTA was crystalline. Observing the absorbance spectra of the individual investigated areas for this sample shown in the inset in Figure 26 g) reveals a clear absorption peak at 1.1 THz for two out of six investigated areas. This indicates that crystalline LTA was present only on parts of the sample, which could be due to paper inhomogeneity or inhomogeneous distribution of the loaded LTA across the sample.

Since the same six areas on smartFilms were investigated before and after the loading, the absorbance of fresh paper samples (i.e., before loading) was subtracted from the absorbance of the loaded smartFilms independently for all six areas. This difference in absorbance can be attributed to the LTA loaded into the smartFilms. The calculated absorbance difference for all four loaded samples as well as the control sample is shown in Figure 27.
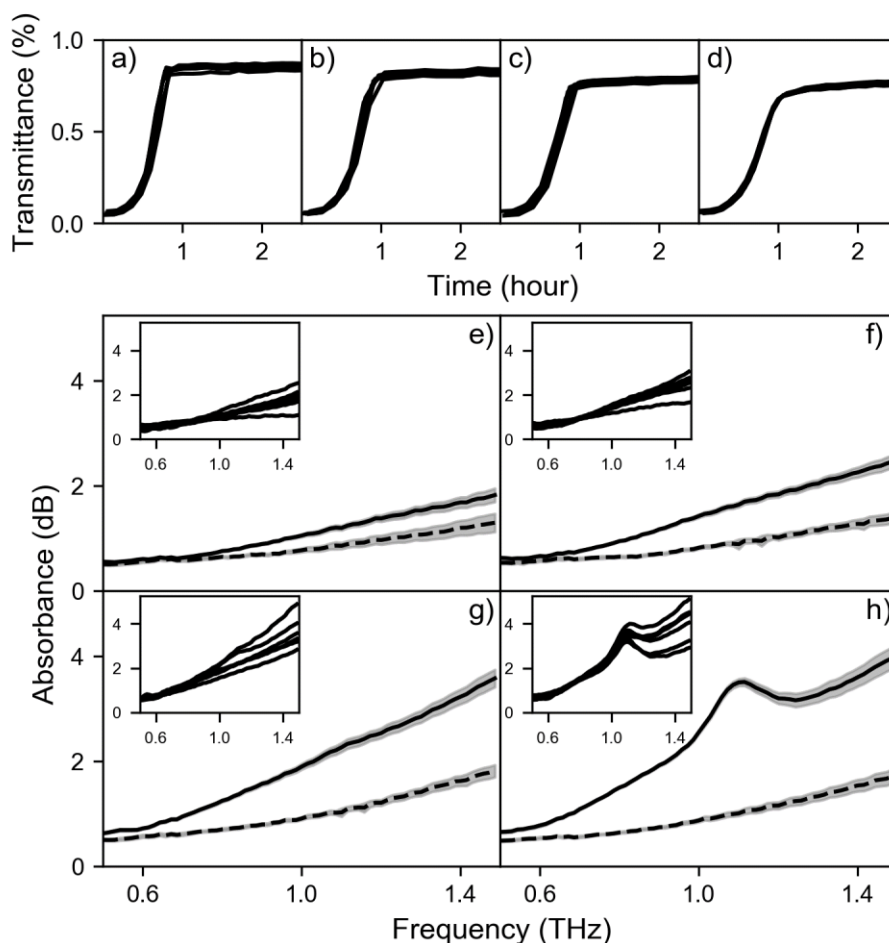
Figure 26. a-d) Transmittance in the frequency range between 0.6 and 0.8 THz of the individual areas of the samples during drying after applying the LTA solution with concentration of 5, 10, 15 20 w%, respectively. e-h) Average frequency dependent absorbance of the whole paper samples before (dashed lines) and after loading and drying (solid lines) for the applied LTA solution with concentration of 5, 10, 15 20 w%, respectively. The shaded gray areas correspond to the assessed measurement uncertainty based on the ten repeated measurements. In the inset, the absorbance for the individual areas of the loaded sample is shown.

For the control sample, the absorbance difference was approximately zero within the measurement uncertainty. This is expected since no LTA was loaded into the sample. In the case of all smartFilms (Figure 27 b-e)) a positive difference in absorbance can be observed, which is attributed to the amount of the loaded LTA. Furthermore, for the 15 w% sample an absorption peak at 1.1 THz, which indicates the presence of crystalline LTA, can be observed for two out of six investigated areas on the sample. In the case of 20 w% the 1.1 THz absorption peak can be observed for all six investigated areas. From the results presented in terms of absorbance difference (Figure 27) and in terms of absorbance before and after the loading (Figure 26) equivalent conclusions can be drawn. However, in the case of absorbance difference the curves corresponding to different areas on the sample vary less compared to the absorbance of loaded samples (see insets in Figure 26). This can be attributed to the different absorption of the fresh paper (i.e., before loading) on different areas due to paper inhomogeneity that is already considered in the case of absorbance difference. Therefore, the results for smartFilms

obtained in the main investigation are discussed in terms of absorbance difference. The results of the main investigation are presented in the next section.
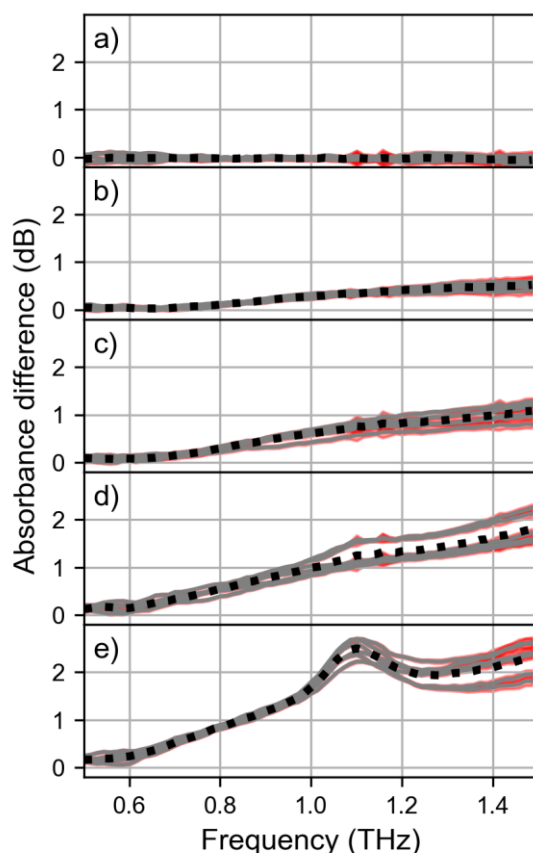

Figure 27. Absorbance difference for a) control sample (i.e., 0 w%) and for b-e) smartFilms loaded with LTA aqueous solution with concentration of approximately 5, 10, 15, and 20 w%, respectively. The gray lines correspond to the six investigated areas. The red shaded area corresponds to the measurement uncertainty estimated based on the measurement repetitions. The black dotted lines correspond to the average absorbance difference of the whole sample.

In summary, the preliminary investigation revealed that THz TDS has the potential for non-destructive inspection of smartFilms in terms of the crystallinity state of the loaded chemical (i.e., LTA). The data suggest that the LTA loaded into the paper remains amorphous when the paper samples are soaked with aqueous solutions with LTA concentration not exceeding 10 w%. This corresponds to an LTA content in the smartFilms of approximately 25 w% and 2.2 mg/cm². When more concentrated solutions are used, the LTA content increases and the characteristic 1.1 THz absorption peak for the crystalline LTA can be observed. This indicates that smartFilms have a certain loading limit up to which they can maintain the substance amorphous. In the following section a more elaborated investigation of smartFilms loaded with LTA is presented.

4.2 Main investigation

For the second, main part of investigation focusing on the feasibility of THz TDS for investigation of smartFilms the procedure of loading the smartFilms was altered. In the

preliminary investigation, solutions with different concentrations were prepared to influence the content of the LTA loaded into a sample. For the preparation of smartFilms presented in this section of the thesis a single stock solution was used. To increase the content of LTA loaded into a sample, the loading cycle was repeated, i.e., the solution was applied to the already loaded and dried smartFilms as discussed in subsection 3.4.3. Furthermore, for each selected loading of the smartFilms five samples were prepared and investigated. As a positive control, physical mixtures with corresponding LTA content were prepared and investigated. SmartFilms were also pressed into tablets and investigated using THz TDS. Additionally, smartFilms were investigated using XRD and DSC.

4.2.1 Sample preparation and investigation

For the preparation of smartFilms, in total 25 smaller rectangular pieces (35 mm x 40 mm) were first cut from the paper basis. Then a stock aqueous solution of LTA with a concentration of 56 mg/ml was prepared. In each loading cycle 250 µl of the solution were applied to the paper samples with a pipette. The selected volume resulted in wetting of the whole sample in a way that no excess solution dropped from the paper sample. The wet samples were dried in a fume hood at ambient temperature for approximately one hour. The applied volume and the selected concentration of the stock solution resulted in 14 mg of LTA loaded into the paper matrix per loading cycle, which corresponds to the LTA content of 1 mg/cm² per loading cycle. This was also the lowest selected amount of loaded LTA, as the preliminary investigation revealed that for approximately this content smartFilms can maintain LTA amorphous (see section 4.1). To increase the amount of the LTA in the smartFilms, the loading cycle was repeated. Each repetition resulted in additional 1 mg/cm² loaded into the smartFilms. In total 1, 2, 3, 4, and 5 loading cycles were considered resulting in an LTA content of 1, 2, 3, 4, and 5 mg/cm², respectively. For each LTA content five smartFilms were prepared, which were stored at room temperature until the subsequent investigation and processing. The overview of the prepared smartFilms is summarized in Table 4.

Table 4. Overview of the prepared smartFilms. For each amount of loaded LTA (i.e., LTA content) five samples were prepared, resulting in 25 samples in total.

Number of loading cycles	m_{LTA} (mg)	LTA content (mg/cm²)	LTA content (w%)
1	14	1	13
2	28	2	23
3	42	3	31
4	56	4	37
5	70	5	43

The prepared smartFilms were placed into slide frames for easier handling during THz TDS investigation (see Figure 28 a)). The cut paper samples were investigated using THz TDS prior to the loading of LTA and can be considered as a negative control. In addition to the smartFilms, physical mixtures with corresponding LTA content (i.e., 13, 23, 31, 37, and 43 w%) were prepared as a positive control. For preparation of physical mixtures paper powder was first prepared by milling the coffee filter paper using a mixer

mill (MM 400, Resch GmbH, Germany). Then LTA bulk material was added in desired proportions with respect to the paper powder and mixed by using pestle and mortar.
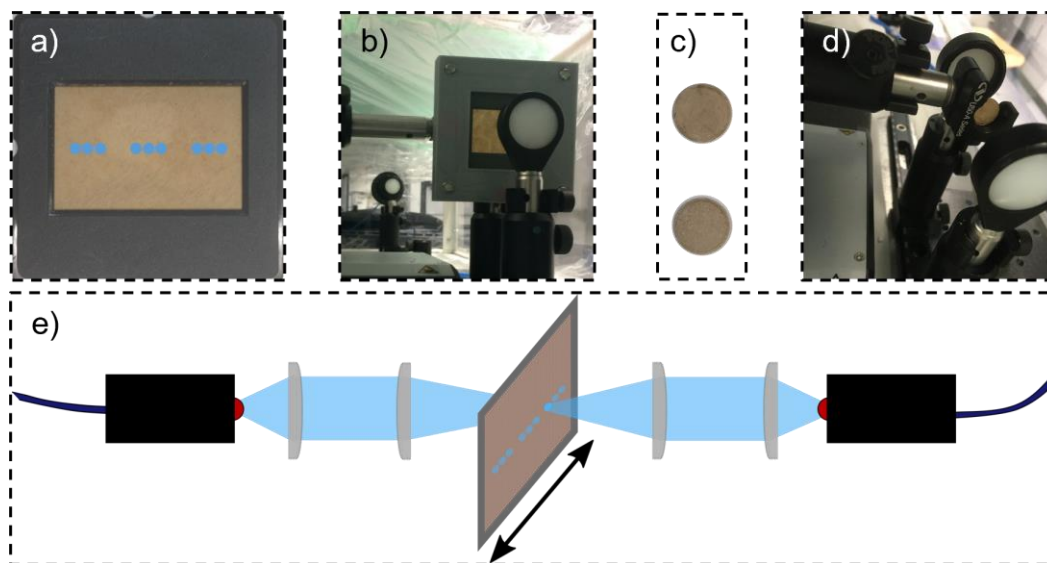

Figure 28. THz TDS investigation of smartFilms and paper tablets. a) SmartFilm inserted into a slide frame. The nine blue dots indicate the nine investigated areas on a smartFilm. The same nine areas were investigated before and after loading of each sample. b) Photo of a smartFilm sample in the THz beam path. c) Photos of paper tablets made from smartFilms (top) and physical mixture (bottom). d) A photo of a paper tablet in the beam path. e) Sketch of the THz beam path consisting of fiber-coupled emitter and detector modules and two pairs of lenses. More details about the setup can be found in [176].

For the THz investigation the prepared powder mixtures were pressed into tablets by filling the cavity of the tablet press (EK0, Korsch AG, Germany) and compressing them with a force not exceeding 30 kN [177]. The tablet press was operated manually. For each LTA content three tablets were prepared. In addition to the tablets made from physical mixtures, five individual smartFilms (i.e., one per LTA content) were also pressed into tablets. They were first cut into smaller pieces of approximately 10 mm by 10 mm to fit the cavity of the tablet press. All obtained tablets were circularly shaped (see Figure 28 c)) with diameter of 10 mm, bi-planar facetted, and had a thickness of approximately 1 mm.

For the XRD and DSC analysis the prepared powder mixtures were directly used without pressing them into tablets. The XRD and DSC analysis of smartFilms was performed after the THz measurements were completed. For the XRD analysis of smartFilms a single smartFilms sample per LTA content was analyzed after cutting it into smaller pieces which fit the sample stage. Additionally pure bulk LTA material and paper films without loaded LTA were investigated. The XRD analysis was performed with a X'Pert Pro PW3040/60 (Philips/Panalytical B.V., Netherlands) system. The voltage of the anode made from cobalt was set to 40 kV with a current of 35 mA. The measurements were performed for the 2θ ranging from 10 ° to 110 ° with a step size of 0.026 °. The DSC analysis was performed using a DSC 7 (Perkin-Elmer Inc., USA). 5-6 mg of corresponding samples were inserted into 40 µl aluminum pans. SmartFilms were cut

into smaller pieces which fit into the aluminum pans. The samples were heated from 50 °C to 300 °C at a heating rate of 10 K/min.

4.2.2 Results

SmartFilms were investigated on nine colinearly selected spots (see Figure 28) using THz TDS before loading them with LTA. Several days after the 25 smartFilms were loaded the same nine areas on the samples were again investigated. Furthermore, first the smartFilms with higher LTA content were investigated followed by the smartFilms with lower LTA content. The THz TDS measurements of all 25 loaded smartFilms were performed within two weeks. The difference in absorbance before and after the loading of the smartFilms is shown in Figure 29.
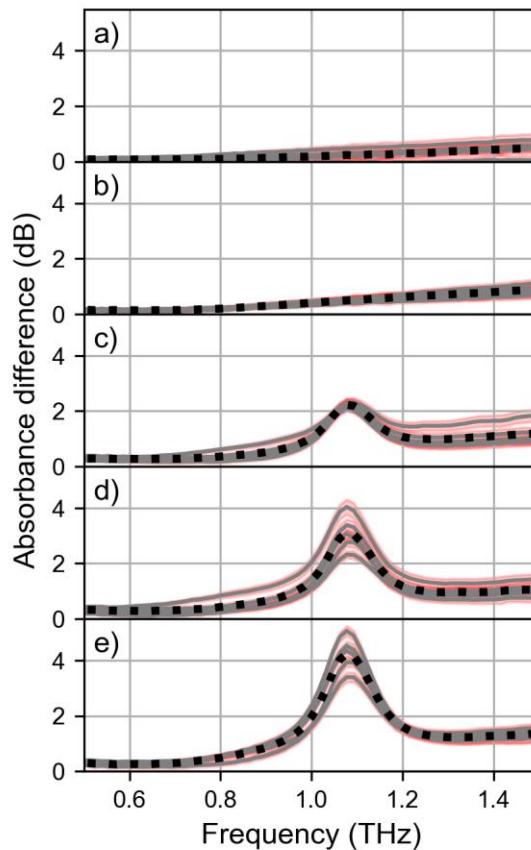
Figure 29. a-e) Absorbance difference for smartFilms with 1-5 mg/cm² LTA content, respectively. The gray lines correspond to the average absorbance difference for five different samples (i.e., individual investigated areas not shown). The red shaded area corresponds to the measurement uncertainty estimated based on the measurement repetitions. The black dotted lines correspond to the average absorbance difference of all five samples with the same LTA content.

For the lowest two LTA contents (i.e., 1 and 2 mg/cm²) the 1.1 THz absorption peak is not observed, which indicates that the smartFilms maintained the LTA in its amorphous state. This was the case for all five samples per loading (grey lines in Figure 29) and for all investigated areas (data not shown). For higher loadings (i.e., 3-5 mg/cm²) a clear absorption peak at 1.1 THz can be observed, which indicates that the loading limit of the paper matrix was exceeded and LTA at least partially crystallized. This was again the

case for all five samples per LTA content and all investigated areas (data not shown). Furthermore, with increasing LTA content also the peak amplitude increased, which suggests that after the loading limit was reached, the majority of added LTA crystallized. After the THz measurements of smartFilms were done, single sample per LTA content was investigated with XRD and DSC. The results of the XRD investigation of smartFilms are shown in the left half of Figure 30. On the right side of the figure the diffractograms of the corresponding physical mixtures are shown.
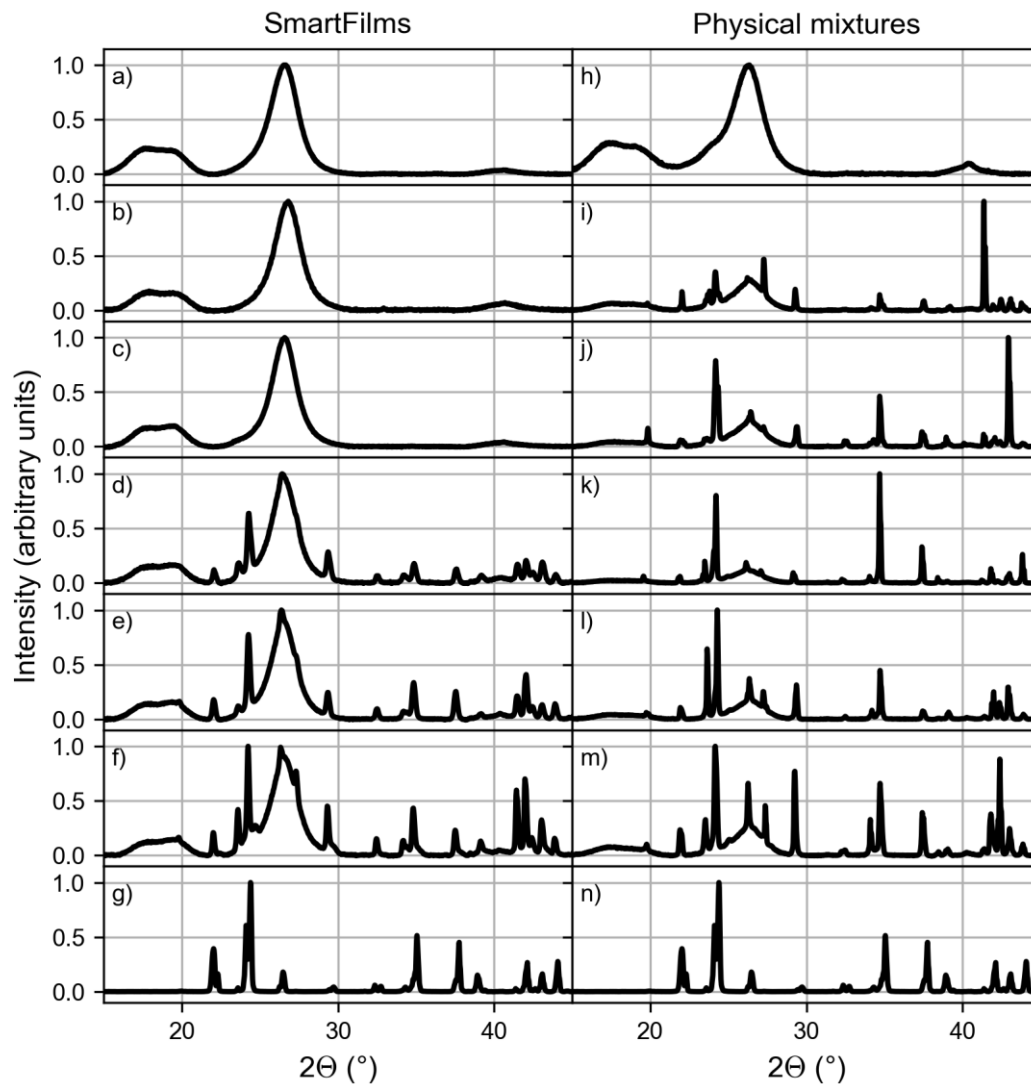
Figure 30. X-ray diffractograms for smartFilms (left part of the figure) and physical mixtures (right part of the figure). The panels a) and h) on top of the figure correspond to paper film and milled paper without any LTA, respectively. In panels g) and n) at the bottom the same diffractogram of bulk LTA is shown. In panels c-d) diffractograms corresponding to smartFilms with 1-5 mg/cm² LTA content are shown, respectively. Panels i-m) show diffractograms of the corresponding physical mixtures (i.e., LTA content of 1-5 mg/cm², respectively).

In the most upper two panels in Figure 30 the diffractograms of a) paper film and h) milled paper both without any LTA are shown. In both diffractograms two broad diffraction features can be observed. First at approximately 17 ° and second at approximately 26 °.

In the panels g) and n) at the bottom of the Figure 30 the same diffractogram of the bulk LTA material is shown. LTA exhibits several diffraction peaks, which are all narrower compared to the two features exhibited by the paper. The most prominent features are located at 22, 24, 35, and 35 °, whereby the features at 22 ° and 24 ° both contain two diffraction peaks. Between the panels with diffractograms of the paper and the LTA sample, diffractograms of smartFilms (left part of Figure 30) and the corresponding physical mixtures are shown (right part of Figure 30).

In the case of physical mixtures, peaks characteristic for LTA can be observed for all LTA contents. In the case of smartFilms, no peaks characteristic for LTA can be observed for the LTA content of 1 and 2 mg/cm², which again suggests that LTA was maintained amorphous by the smartFilms. For a greater LTA content, the characteristic LTA peaks can be observed, which means that crystalline LTA was present in the sample and that the loading limit of the smartFilms was exceeded. These observations are in complete agreement with the observations made based on the THz TDS measurements of smartFilms. Additional THz TDS measurements were performed on tablets pressed from smartFilms and physical mixtures. The results of the extracted absorption coefficient from these measurements are shown in Figure 31.

In the panels a) and g) in the upper part of the Figure 31 absorption spectra of pressed paper films and pressed milled paper are shown, respectively. In both cases the absorption coefficient monotonically increases with frequency and no distinct absorption features can be observed. In the case of physical mixtures (right hand-side of Figure 31) the absorption peak at around 1.1 THz can be clearly observed. The strength of the peak increases with the increasing LTA content. In the case of smartFilms, no 1.1 THz absorption feature is observed for the loadings lower than 3 mg/cm², which again indicates that LTA was maintained amorphous by the smartFilms. Furthermore, this also means that the pressing of smartFilms into the tablets did not cause a crystallization of LTA. For greater LTA content the smartFilms could not maintain the LTA amorphous (see Figure 29), which remained this way also after transferring them into the tablet form.

SmartFilms and physical mixtures as well as the bulk LTA were examined using DSC. However, except for the investigation of the bulk LTA, the measurements were irreproducible (data not shown). Furthermore, neither for smartFilms nor for the physical mixtures the endothermic feature due to the melting of the LTA could be observed. This endothermic feature was expected at least for physical mixtures since they contain crystalline LTA. Different potential reasons for such unexpected behavior were experimentally investigated. It was established that the observed problem is related to the hygroscopic nature of LTA and its good aqueous solubility and the fact that paper contains certain amount of water which is sufficient to dissolve the amount of LTA in the samples during heating of the sample. More information about the DSC investigation can be found in [176].
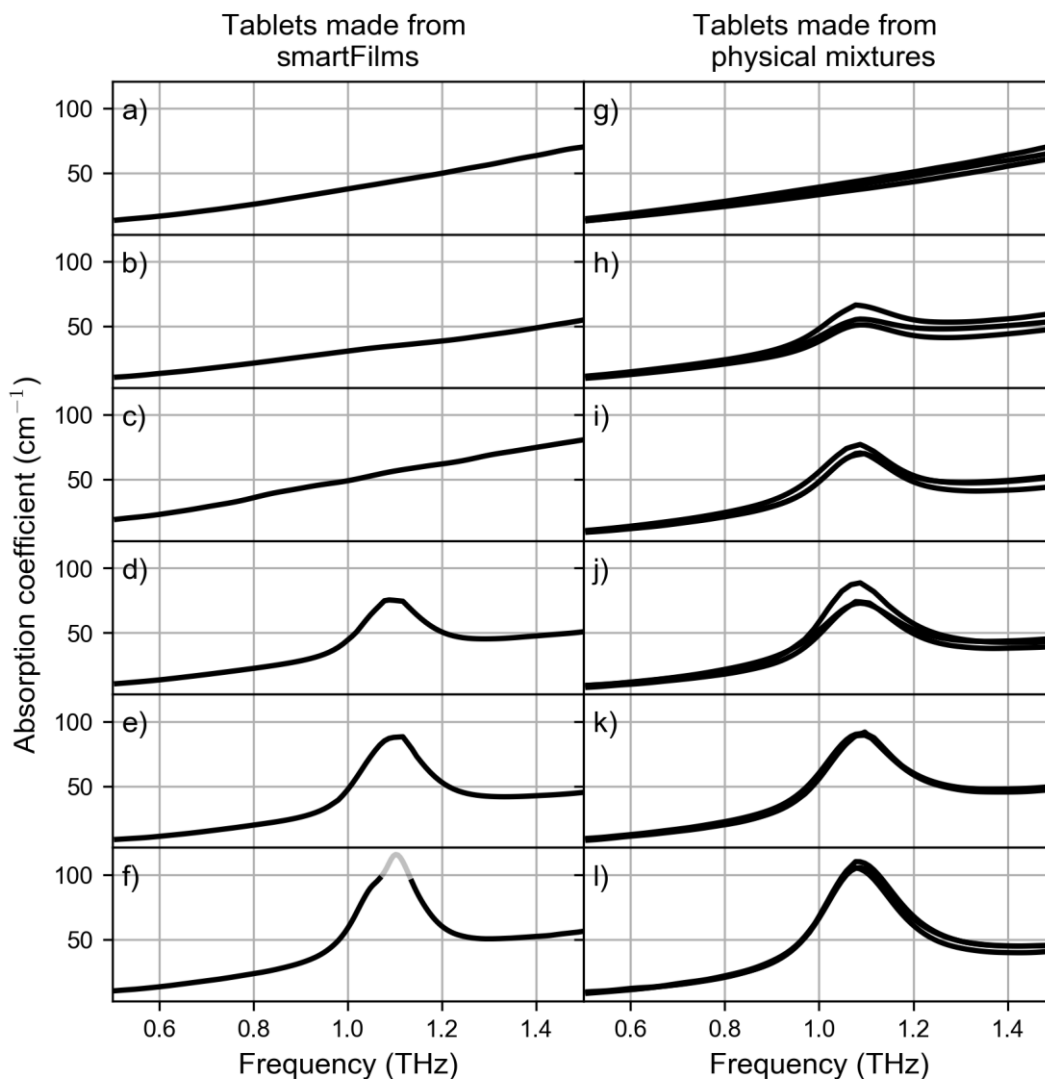
Figure 31. a-f) Absorption coefficient for smartFilms pressed into tablets (left part of the figure) with LTA content of 0, 1, 2, 3, 4, and 5 mg/cm² , respectively. g-l) Absorption coefficient for the corresponding physical mixtures (right part of the figure). Tablets made from physical mixtures were prepared in triplicate, whereas single smartFilms per LTA content were pressed into tablets. Note that for the tablet made from smartFilms with 5 mg/cm² content of LTA shown in f) the dynamic range of the spectrometer was exceeded around 1.1 THz (light-grey part of the curve). The tablets differed in thickness between approximately 0.8 and 1.2 mm. The 5 mg/cm² smartFilms tablet was the thickest. The absorption coefficient was extracted using software TeraLyzer (see subsection 2.1.2). The absorption coefficient of bulk LTA is shown in Figure 23.

In summary, the investigation of smartFilms loaded with LTA confirmed the feasibility of THz TDS for non-destructive testing of smartFilms as well as tablets made from them. The presented results revealed that smartFilms maintain LTA amorphous up to the LTA content of approximately 2 mg/cm² which corresponds to 23 w% of LTA in the paper matrix. If more LTA is loaded into the smartFilms, the LTA at least partially crystallizes. In the case of physical mixtures with the corresponding LTA content the characteristic absorption peak for the crystalline LTA was observed for all samples. This suggests that THz TDS is sensitive enough to detect crystalline LTA for the selected LTA content. Furthermore, the results obtained from THz TDS were confirmed with an XRD analysis

of the samples, which delivered qualitatively equivalent results, however, in a destructive way. The presented results in this proof-of-principle study demonstrate the potential of THz TDS for the non-destructive investigation of the crystalline state of APIs in the smartFilms and tablets made from them. In the following chapter THz absorption properties of different pharmaceutically relevant materials are presented.

5 THz absorption coefficients of selected pharmaceuticals

In this chapter the absorption coefficients of selected materials are presented. The key idea thereby is to determine which materials exhibit distinct absorption features in the investigated spectral range. Furthermore, the magnitude of these features is also of interest. In the case of APIs, pronounced absorption features are desired since this way THz TDS could be used for the inspection of their solid state in a similar manner as discussed in the previous chapter. Furthermore, absorption properties of pharmaceutically non-active ingredients (i.e., excipients) are also relevant as they could influence the success of such an investigation. Many of the selected materials have been investigated before and the results have been published in different scientific journals as well as in online THz databases [184,185]. However, the results are often reported in terms of the absorbance which limits the comparison between different materials especially if the information about the sample thickness is not provided. Furthermore, the way the samples were prepared and analyzed can also differ from one publication to the other, which limits the direct comparison of the magnitude of the absorption peaks. Therefore, the samples of the selected materials in this work were all prepared, investigated, and evaluated following the same procedure.

The materials selected for this work can be divided into two groups. The first group consists of poorly soluble APIs. The second group is composed of selected excipients including the coffee filter paper in form of a powder and of a film, and microcrystalline cellulose (MCC) powder since the smartFilms technology relies on loading APIs into the paper matrix, which is mainly made of cellulose. All acquired samples were received in the form of powders except for the coffee filter paper, and PEG 4000. The latter formed bigger pieces of material. These pieces were, therefore, first grinded with mortar and pestle into a finer powder. Powders of all the selected materials were then individually pressed into tablets without adding any additional material. For this approximately 120 mg of the powder were weighted (Libror EB-3300HW, Shimadzu Deutschland GmbH, Germany) and inserted into the hydraulic press (Model No. GF-10B Cl. 1.0, Enerpac, Germany) and pressed with a force of 30 kN for 90 s. In the case of the milled coffee filter paper the tablet was prepared in the same way as for the rest of the powders. A tablet was also pressed directly from the coffee filter paper. To fit the press the filter paper was first cut into smaller pieces of about 13 mm by 13 mm in size and then pressed into a tablet. All obtained tablets were of cylindrical shape with a diameter of 13 mm and the thickness ranging from 0.55 to 0.85 mm. The obtained tablets were then inserted into the focal plane of a THz TDS transmission system and measured five times. In addition, five reference measurements were recorded. The reference measurements were performed by removing the tablets from the beam path. All measurements were performed under nitrogen atmosphere. The absorption coefficient was extracted with the software TeraLyzer (see section 2.1.2), which allows for simultaneous evaluation of the dielectric properties and the thickness of the sample. The starting value of the sample thickness, which needs to be entered into the software, was determined with a micrometer screw gauge. The extracted absorption coefficients of selected APIs are presented in the next section.

5.1 APIs

The APIs presented in this section were considered as potential model drugs for further investigation involving THz TDS and smartFilms technology. They can be further divided into two subgroups. The first one involves poorly soluble APIs which are used in marketed drugs, whereas the second subgroup includes poorly soluble naturally occurring substances, which can be mainly found in different food supplement products.

The first subgroup includes caffeine (CAF, Caesar & Loretz GmbH, Germany), ibuprofen (IBU, Caesar & Loretz GmbH, Germany), (S)-naproxen (NAP, Carbolution Chemicals GmbH, Germany), indomethacin (IM, Across Organics BV, Belgium), fenoprofen calcium dihydrate (FC, TCI Deutschland GmbH, Germany), carbamazepine (CBZ, TH Geyer GmbH & Co. KG, Germany), nifedipine (NIF, abcr GmbH, Germany), azithromycin (AZM, abcr GmbH, Germany), and norfloxacin (NOR, abcr GmbH, Germany). Caffeine was selected since it was used as a model drug for loading smartFilms and transferring them into tablets [177]. CAF is sparingly soluble in water and used for pain-relief treatment in combination with other pain relievers (e.g., Aspirin) to facilitate their impact [178]. IBU, NAP, IM, and FC are BCS class II drugs and belong to the group of non-steroidal anti-inflammatory drugs [186–189]. CBZ and NIF are also BCS class II drugs. The former is used for treatment of epilepsy [190] and the latter is used for the treatment of high blood pressure as well as angina [191–193]. AZM and NOR are BCS class II and class IV antibiotics [194,195], respectively. The absorption spectra of the nine selected APIs are plotted in Figure 32.

Panel a) in Figure 32 shows absorption spectra of CAF, IBU, and NAP. CAF exhibits two broad absorption peaks in the investigated frequency range. The weaker and stronger absorption peak can be observed at approximately 0.8 THz and 1.25 THz, respectively, which agrees well with the previous reports [196,197]. IBU shows the most prominent absorption peak at approximately 1.05 THz and two weaker absorption peaks at approximately 1.45 and 1.95 THz. This matches with the reported values for the most commonly used racemic (RS)-IBU [198]. In the case of NAP five absorption peaks at approximately 0.95, 1.2, 1.65, 2.0, 2.35 THz can be observed with the most prominent absorption peak at 1.65 THz. The observed absorption features agree with the reported absorption properties of NAP [199]. Strachan et al. investigated different forms of IM, FC, CBZ, which was one of the first demonstrations of the capability of THz TDS for the differentiation and quantification of polymorphism and crystallinity [16,107]. The absorption spectra of these APIs plotted in the panel b) in Figure 32 agree with the reported ones. IM shows three peaks at approximately 1.25, 1.45, and 2.0 THz, with the one at 1.25 THz being the most prominent one. FC shows four broad absorption peaks at approximately 0.5, 0.8, 1.5, and 2.1 THz, whereas CBZ shows five absorption peaks at approximately 0.85, 1.25, 1.8, 2.0, and 2.4 THz with the peaks at 1.25 and 1.8 THz being the most prominent ones. The observed features agree well with the reported absorption spectrum for CBZ form III [16]. Panel c) in Figure 32 displays absorption spectra for NIF, AZM, and NOR. NIF exhibits a pronounced absorption feature centered at approximately 1.2 THz composed out of three individual absorption peaks and a broad absorption feature at approximately 2.3 THz. The observed spectrum agrees with the previous reports [110,197]. For AZM several weak absorption features can be observed with the most prominent one at approximately 1.5 THz. NOR exhibits four pronounced

absorption features at approximately 0.8, 1.2, 2.0, and 2.3 THz. The absorption peaks at approximately 0.8 and 1.2 THz have been previously reported [200].
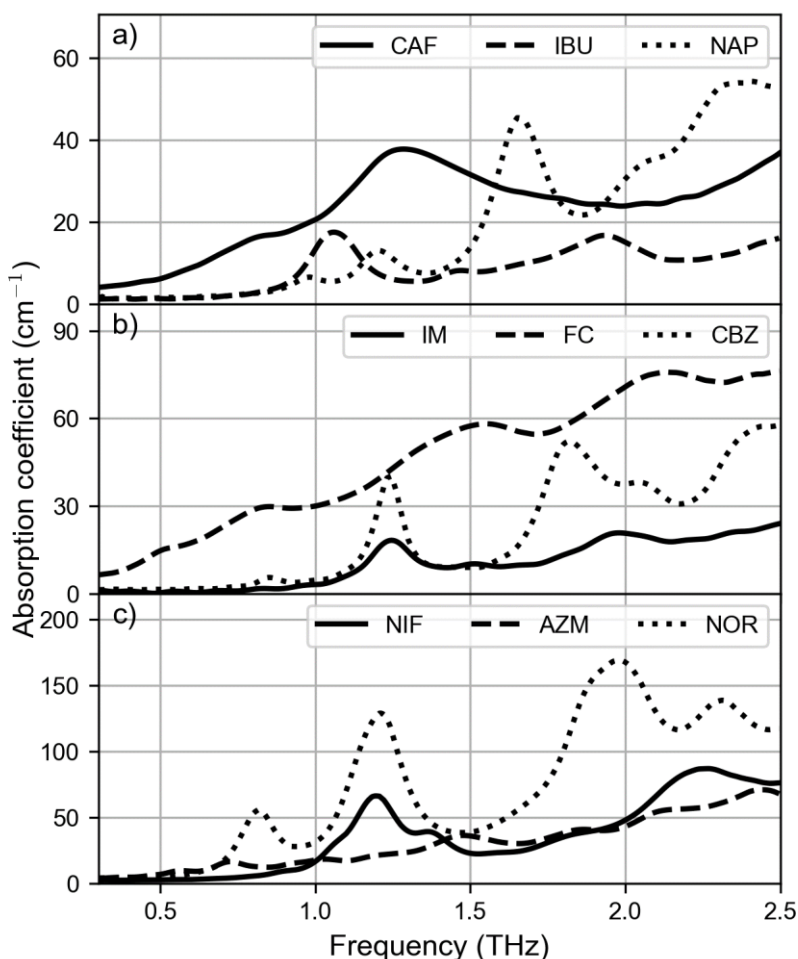

Figure 32. Absorption coefficient for selected APIs in the frequency range between 0.3 and 2.5 THz.

The second subgroup of APIs includes rutin (Denk Ingredients GmbH, Germany), curcumin (CUR, Carl Roth GmbH + Co. KG, Germany), apigenin (APG, Exquim S.A., Spain), hesperetin (HST, Exquim S.A., Spain), hesperidin (HSD, Exquim S.A., Spain), and quercetin (QRT, Denk Ingredients GmbH, Germany). It is common for the substances forming this subgroup that they can be extracted from plants and fruits. Thus, they are often part of a daily diet. Furthermore, their therapeutic potential has been considered in the past and is part of an ongoing investigation. For now, however, these compounds appear on the market mainly as part of food supplement products. Rutin has been considered for many of its properties such as its anti-inflammatory, antioxidant, antibacterial effects as well as most recently for treatment of SARS-CoV-2 infections in combination with other compounds [201]. Furthermore, it was also used as a model, poorly soluble drug in the work of F. Stumpf on smartFilms and tablets made from them [178]. APG, HST, HSD and QRT are also poorly soluble in water [202–205] and belong to the group of flavonoids. They are considered for their anti-inflammatory, antioxidant, and cytoprotective properties [206–208]. Curcumin is a poorly soluble polyphenol known for its antioxidant, anti-inflammatory, and antibacterial properties [179,209]. The

absorption spectra of the six compounds composing this second subgroup are plotted in Figure 33.

In panel a) in Figure 33 absorption spectra of Rutin, CUR, and APG are shown. Rutin exhibits strong background absorption and three weak absorption peaks at approximately 0.9, 1.2, and 1.8 THz. In the case of CUR three absorption features at approximately 0.7, 1.0, and 1.9 THz can be observed with the absorption peak at approximately 0.7 THz being the most pronounced one. In the case of APG the most pronounced absorption peak can be observed at 1.5 THz. In panel b) in Figure 33 absorption spectra of HST, HSD and QRT are presented. For HST three clear absorption peaks can be observed at approximately 0.7, 1.2, and 1.5 THz. HSD exhibits absorption peaks at approximately 0.8, 1.2, 1.6, and 1.9 THz. QRT shows several absorption features at 0.7 1.2, 1.65, 2.1, 2.2 THz. The latter two peaks partially overlap and form kind of a double peak, which is the most pronounced feature in the THz absorption spectrum of QRT.
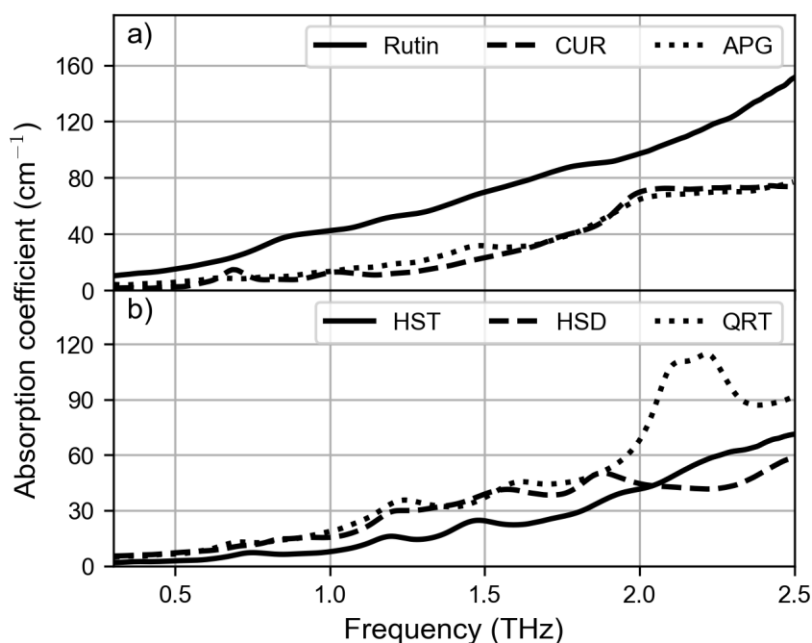
Figure 33. Absorption spectra of selected naturally occurring substances in the frequency range between 0.3 and 2.5 THz.

In this and the previous section in total 15 poorly soluble APIs were introduced and their THz absorption spectra were presented. They all show distinct absorption peaks when in crystalline state, some of them more pronounced than others. This means that they can all be considered for a similar study to the one presented in chapter 4 involving LTA. However, especially those with intense and pronounced absorption features can be considered promising for such an investigation. In the following section the absorption coefficients of the filter paper used for the preparation of smartFilms and further excipients are presented.

5.2 Excipients

Excipients are materials other than the API that compose the final drug formulation. In general, this means that the excipients can be considered inactive. Despite being inactive, they play an important role in the production and in the optimization of the performance of a medicine. For example, excipients are used for solubility improvement of poorly soluble drugs, for increasing dissolution and drug release rate, and to decrease unwanted side effects [210]. Furthermore, some excipients such as microcrystalline cellulose (MCC) are used in the direct compression tableting process to ensure sufficient binding [211]. The absorption spectra of MCC (Carl Roth GmbH + Co. KG, Germany) as well as pressed pieces of coffee filter paper (Filtertüte 1x6/40 naturbraun, Melitta Europa GmbH & Co. KG, Germany) and pressed milled coffee filter paper, which is mainly composed from cellulose, are shown in Figure 34.
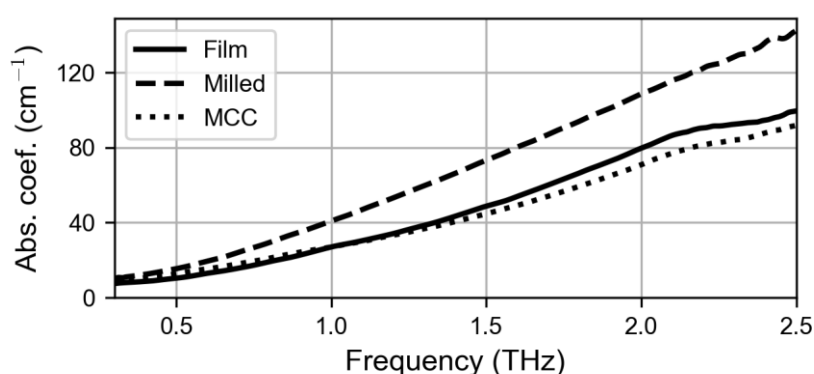

Figure 34. Absorption spectra of coffee filter paper (film), milled coffee filter paper, and MCC powder all individually pressed into tablets. Note that the filter paper consists mainly of cellulose, which is also a common excipient.

For tablets made from MCC and coffee filter paper an absorption peak at around 2.2 THz can be observed, which is in accordance to previous reports on MCC [109]. In the case of a tablet made from milled coffee filter paper, the absorption coefficient appears greater compared to the tablets made from MCC and from non-milled coffee filter paper. Furthermore, the absorption peak at approximately 2.2 THz cannot be observed for the milled paper. This indicates that cellulose became amorphous during the milling process, which has been observed before by employing THz TDS [109].

Polyvinylpyrrolidone K30 (PVP, Carl Roth GmbH + Co. KG, Germany), PEG 4000 (Sigma-Aldrich Chemie GmbH, Germany), magnesium stearate (MGS, Euro OTC Pharma GmbH, Germany), D-(+)-sucrose (SUC, Carl Roth GmbH + Co. KG, Germany), α-lactose monohydrate (α-LAC, Sigma-Aldrich Chemie GmbH, Germany), and D-(+)-glucose also known as dextrose (DEX, Sigma-Aldrich Chemie GmbH, Germany) were selected as example excipient materials. PVP and PEG 4000 are often used for formation of solid dispersions to enhance the solubility of poorly soluble APIs [110,165,212]. MGS is used as lubricant in the tableting process [213]. SUC, α-LAC, and DEX are sugars, which can be used as sweeteners and can help masking the bitter taste of other ingredients [213–215]. However, these sugars often exhibit poor compressibility or binding properties. Therefore, they are often combined with further chemicals to obtain better compressibility [213,216]. Furthermore, DEX is also used as a soluble carrier for

the APIs as well as a bulking agent [214], whereas α-LAC is one of the most common fillers in tablets [216]. The absorption spectra of these six excipients are displayed in Figure 35.
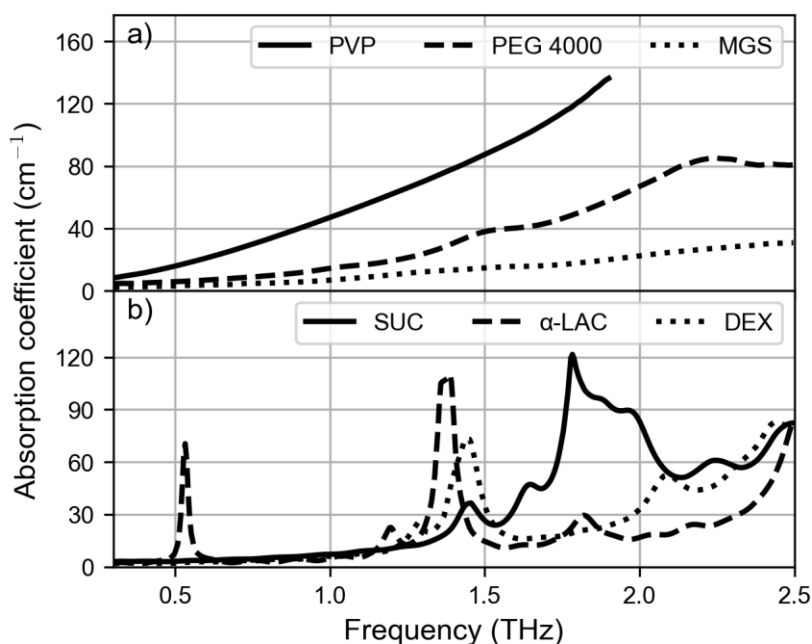

Figure 35. Absorption spectra of the selected excipients.

PVP shows a featureless absorption coefficient continuously increasing with frequency in the investigated frequency range. The absorption coefficient of PVP exceeds 140 cm^{-1} at 1.9 THz. As a result, the dynamic range of the spectrometer is exceeded for higher frequencies at the given sample thickness and the absorption coefficient cannot be evaluated anymore (see subsection 2.1.2). PEG 4000 is less absorbing than PVP and exhibits two broad absorption peaks at approximately 1.5 and 2.2 THz. MGS is even less absorbing and shows no clear, pronounced absorption features in this frequency range. The absorption spectra of sugars shown in the panel b) of Figure 35 reveal that SUC, α-LAC, and DEX are relatively low absorbing for frequencies lower than 1.2 THz except for α-LAC which exhibits a narrow but strong absorption peaks at 0.55 THz. α-LAC shows the most prominent absorption peak at around 1.35 THz and two further, however, weaker absorption peaks at approximately 1.2, and 1.8 THz. For SUC distinct absorption peaks at approximately 1.4, 1.6, 1.8 and 2.3 THz can be identified. In the proximity of the absorption peak at 1.8 THz two comparably weaker absorption peaks can be observed at approximately 1.85 and 1.95 THz. In the case of DEX, the most prominent absorption peak appears at approximately 1.45 THz. Two further, weaker peaks emerge at approximately 1.3 and 2.1 THz. The identified absorption features of the three sugars are in agreement with previous reports [12,15].

In the following section the absorption spectra of pharmaceutical substances presented so far are analyzed in more detail. The goal of the analysis is to provide an overview of individual absorption peaks observed for different substance in terms of their width, magnitude, and frequency position.

5.3 Overview

One of the main objectives of this work is to exploit the potential of THz TDS for the inspection of the solid state of pharmaceuticals loaded into smartFilms. The key idea, as demonstrated in chapter 4, relies on the identification of distinct absorption features in the absorption spectrum, which are related to the crystalline form of the pharmaceuticals. In this section the absorption spectra of the selected pharmaceuticals are analyzed in more detail to obtain amplitude, width, and frequency position of the individual absorption peaks. This is the basis for the quantitative analysis presented in the following chapter. To obtain the parameters of the individual absorption peaks we model them as Gaussian functions and at the same time describe the continuously rising, featureless part of the absorption spectra as a second order polynomial. In other words, we describe the frequency dependent absorption coefficient of individual substance ($a_{sub}(\nu)$) as the sum of second order polynomial and N Gaussian functions:

$$a_{sub}(\nu) = \sum_{i=1}^{N} G_i e^{-\frac{(\nu-\nu_{0,i})^2}{2\Delta\nu_i^2}} + O(2),$$ 5.1

where $O(2)$ is the second order polynomial, N is the number of identified absorption peaks, and G_i, $\nu_{0,i}$, and $\Delta\nu_i$ are amplitude, frequency position, and width of the i-th identified absorption peak, respectively. The parameters of the identified peaks are extracted by fitting this function to the individual absorption spectra. Figure 36 presents the measured and fitted absorption spectrum of LTA between 0.3 and 2.2 THz.
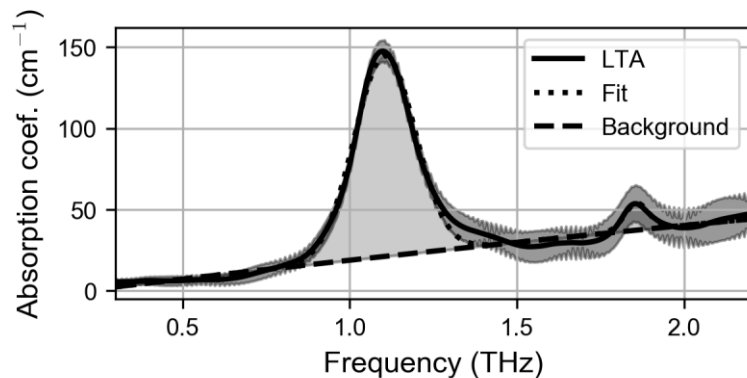
Figure 36. Measured (solid line) and fitted (dotted line) absorption spectrum of LTA. The spectrum is described as a sum of a second order polynomial and two Gaussian absorption peaks. The polynomial describes the background absorption (dashed line). The two shaded areas in light gray correspond to the two modeled absorption peaks. The shaded area in dark gray corresponds to the measurement uncertainty estimated based on the measurement repetition.

Since LTA exhibits only two distinct absorption peaks in the investigated frequency range, only two Gaussians functions and the second order polynomial were needed to describe the spectrum. Therefore, the value of N was set to two when fitting the function 5.1 to the measured absorption spectrum. The fitted spectrum matches well the experimentally obtained values in the investigated spectral range. The peak parameters obtained by fitting the function 5.1 to the absorption spectrum of LTA are listed in Table 5.

Table 5. The amplitude, width, and position of the two absorption peaks exhibited by LTA in the frequency range between 0.3 and 2.2 THz.

i	G (cm^{-1})	ν_0 (THz)	$\Delta\nu$ (THz)
1	123.4	1.10	0.09
2	16.6	1.86	0.04

As expected, the extracted amplitude of the peak at 1.1 THz is much greater compared to the other absorption peak at 1.86 THz. Furthermore, the absorption peak at 1.1 THz is also more than two times wider than the weaker absorption peak at 1.86 THz. Note that the width of the peak based on the definition in equation 5.1 means that at $\nu_0 \pm \Delta\nu$ the peak amplitude drops to approximately 60 % of its maximum value. The same analysis of the absorption spectra was performed for all pharmaceutical substances investigated in this work. Depending on the number of identified absorption peaks, the number of peaks to be fitted was adjusted accordingly. Figure 37 summarizes the extracted properties of the identified absorption peaks for all investigated substances in the frequency range between 0.3 and 2.0 THz.

The intensity of the absorption peaks in Figure 37 is color coded and plotted with respect to the frequency and individual pharmaceutical substance on the horizontal and vertical axis, respectively. The horizontal bands related to the individual substances are equidistant and, in a way, correspond to the absorption spectra of individual substances in terms of the individual absorption peaks in the investigated frequency range. The horizontal band at the bottom corresponds to LTA and the six bands on the top correspond to the investigated excipients. In between the APIs are located. Note that MCC, MGS, and PVP are not shown in this representation, since they do not show any distinct absorption peaks in this frequency range, which would result in zero values (i.e., blue color) across the whole band.

Due to the great difference between the weakest and strongest absorption peak among all the investigated substances, the color scale had to be additionally adjusted for clearer representation. All values of absorption coefficient exceeding 35 cm^{-1} were set to this limit value. This can be clearly observed on the example of LTA, whose absorption peak at 1.1 THz exceeds 120 cm^{-1} (see Table 5), however, in this representation the value is artificially limited to 35 cm^{-1}. Note that because of this color scale adjustment this peak appears also much wider compared to the original measurement and the extracted peak parameter shown in Figure 36 and Table 5, respectively. Nevertheless, Figure 37 offers an easy way to compare the position of individual absorption features and to certain extent also their intensities and widths. This way combinations of substances for which absorption features overlap can be easily identified. Such overlapping of spectral features could additionally complicate the analysis of a pharmaceutical formulation consisting of several different substances when investigating the crystallinity and amorphousness of an API in a formulation using THz TDS.
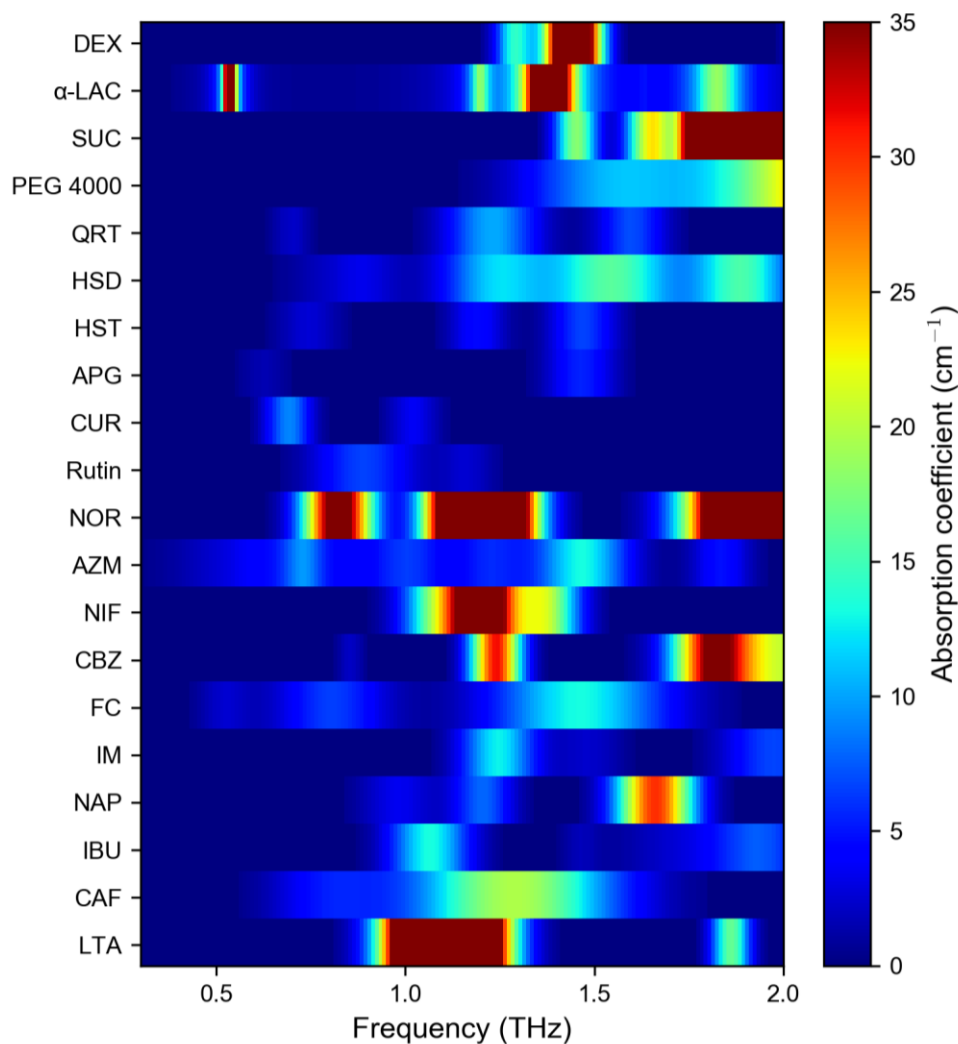
Figure 37. Absorption coefficients of the identified absorption peaks for selected pharmaceuticals in the frequency range between 0.3 and 2.0 THz. The absorption coefficient is color coded. The individual equidistant horizontal bands correspond to the identified and extracted absorption features of the individual pharmaceuticals indicated on the vertical axis. Note that the values of the absorption coefficient, which exceed 35 cm^{-1} were artificially limited to 35 cm^{-1}.

In this chapter absorption spectra of selected pharmaceuticals were presented. Many show distinct absorption peaks when in crystalline state. On the contrary, in the investigated frequency range amorphous substances generally show featureless absorption which continuously increases with the increasing frequency for the investigated frequency range [20]. By describing the absorption spectra as a sum of a second order polynomial and a number of Gaussian functions corresponding to the number of identified absorption peaks, the individual absorption peaks could be characterized. This characterization presents the basis for the quantitative analysis of crystalline and amorphous IM in tablets made from smartFilms which is presented in the following chapter.

6   Crystallinity quantification of indomethacin in paper tablets

IM is a poorly soluble non-steroidal anti-inflammatory drug used for treatment of rheumatic arthritis [217,218]. Due to its high permeability and low solubility it is a BCS class II drug [219]. This means that poor solubility can be considered as the main factor limiting its bioavailability (see chapter 3). The solubility of IM can be improved by converting the most used γ-form into the α-form. The solubility of IM can be improved even further by transferring it into its amorphous state [7]. IM is also a well-studied substance in the THz range [16,102,107]. The two most commonly studied polymorphs, α and γ, both show distinct absorption features, which can be used for their discrimination, whereas the amorphous IM shows a featureless absorption spectrum (see Figure 17) [16,102,107]. Furthermore, IM can be easily converted into its amorphous state by melting and subsequently colling it [220,221]. Therefore, IM was selected as a model drug for studying crystallinity of an API loaded in tablets made from paper.

This study is divided into two parts which are presented in the following two sections of this chapter. The first part involves investigation of the two polymorphs of IM as well as the amorphous IM. This includes the characterization of the identified absorption peaks in the case of the two crystalline forms as discussed in the previous chapter. In the second part the preparation of tablets made from smartFilms and the corresponding physical mixtures, and their investigation using THz TDS are presented. Furthermore, the second part includes the quantitative assessment of the amount of crystalline and amorphous IM in tablets made from smartFilms.

6.1   Characterization of absorption features of γ- and α-IM

γ-IM with purity of 97.5 % was acquired from Across Organics BV, Belgium in a powder form and was used without further purification. According to the method reported by Kaneniwa et al. [222], α-IM was recrystallized from the γ-form in a two-step process. In the first step 1.5 g of γ-IM were dissolved in 60 ml of ethanol and the obtained solution was heated up to 75°C. Then the warm solution was filtered using a circular filter paper (LLG-Labware, diameter: 125 mm, pore size 5-13 µm) and a funnel. In the second step, cold distilled water was added to the solution resulting in precipitation of α-IM, which was removed by filtration. The obtained recrystallized-IM was left to dry overnight in a vacuum desiccator containing P_2O_5 as a dehydrating agent.

Both γ-IM and the recrystallized IM were investigated using DSC and THz TDS. For the DSC investigation 1-4 mg of the sample powder were placed into an aluminum pan and heated up with a heating rate of 10 K/min from 293 K to 473 K using the DSC 3 (Mettler Toledo, USA). The obtained thermograms of the two samples are shown in Figure 38.
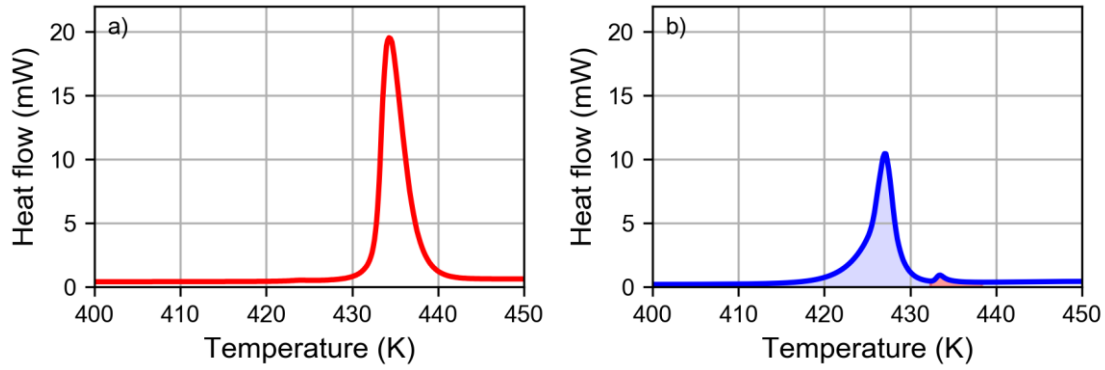
Figure 38. Thermograms of a) γ-IM and b) recrystallized-IM sample. Note the blue and red shaded areas indicating the area under the two peaks in the thermogram in panel b).

For the γ-IM sample a single exothermic peak at 434.3 K can be observed. In the case of the recrystallized-IM samples shown in panel b) in Figure 38 one main peak at 427.0 K and a smaller peak at approximately 434 K can be observed. The former peak corresponds to the α-form and the latter to the γ-form. The presence of the exothermic peak at approximately 434 K indicates that a small amount of γ-IM was still present in the recrystallized sample. By comparing the areas below the two peaks it was possible to determine that the recrystallized-IM sample contained approximately 6 % of γ-IM and 94 % of α-IM.

For the THz investigation two powder samples were pressed into tablets with a diameter of 13 mm by applying a force of 30 kN for 90 s by using a manual hydraulic press (Model No. GF-10B Cl. 1.0, Enerpac, Germany). For the THz TDS measurements a fully fiber-coupled system was employed. More details about the system can be found in reference [30]. Four OAPMs were used to form the THz beam path and the samples were inserted into the focal plane between the second and third OAPM (see Figure 2) with the beam being focused approximately onto the middle of the individual tablets. The THz beam path was enclosed and purged with nitrogen. Reference measurements were performed by recording the THz waveforms without a sample in the beam path. The reference and sample measurements were repeated five times. The absorption coefficient of the samples was extracted with the TeraLyzer software (see section 2.1.2 for more details). Since the DSC analysis revealed that the recrystallized-IM sample still contained 6 % of γ-IM, the absorption coefficient for a pure α-IM ($\alpha_{\alpha\text{-IM}}(v)$) was calculated as:

$$\alpha_{\alpha\text{-IM}}(v) = \frac{\alpha_{recrystallized\text{-}IM}(v) - 0.06\,\alpha_{\gamma\text{-}IM}(v)}{0.94}, \qquad 6.1$$

where $\alpha_{recrystallized\text{-}IM}(v)$ and $\alpha_{\gamma\text{-}IM}(v)$ are frequency dependent absorption coefficients for the recrystallized-IM and γ-IM, respectively. The THz absorption spectra of γ-IM and α-IM were further analyzed by describing them as the sum of a second order polynomial and Gaussian functions according to the equation 5.1. The second order polynomial is used to describe the featureless background absorption related mainly to the scattering whereas the Gaussian functions are used to describe the number of identified absorption peaks in the spectrum. For more details see section 5.3. The absorption coefficient of γ-IM and α-IM is plotted in Figure 39.
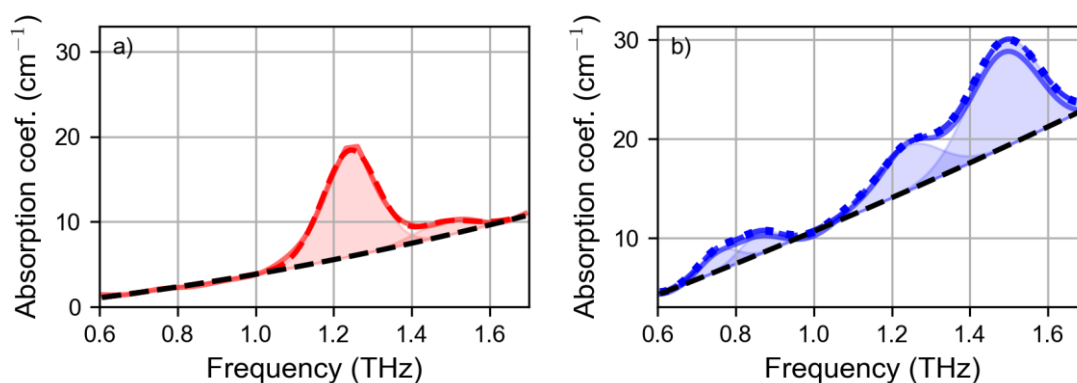
Figure 39. a) Extracted absorption coefficient of γ-IM (red solid line) with the fitted spectrum (dashed red line), featureless background absorption (black dashed line), and the two characteristic absorption peaks (red shaded areas). b) Extracted absorption coefficient of the recrystallized-IM sample (blue solid line) and of the estimated α-IM (blue dotted line) with the fitted spectrum (blue dashed line) consisting of featureless background absorption (black dashed line) and four characteristic absorption peaks (blue shaded areas).

γ-IM shows two pronounced absorption peaks in the shown frequency range. The first, stronger peak is located at 1.25 THz and the second, weaker one at approximately 1.5 THz. In the case of α-IM the two most pronounced absorption peaks can be observed at approximately the same frequencies as the two absorption peaks exhibited by γ-IM. However, the amplitudes of the two peaks are inverted, meaning that the peak at approximately 1.5 THz is stronger than the one at approximately 1.25 THz. Furthermore, in the case of α-IM two additional less pronounced peaks at approximately 0.75 and 0.85 THz are visible. The identified absorption features of the two IM polymorphs are in accordance with the previous THz investigations of IM polymorphs [16,107]. The observed absorption features were further characterized by fitting the function given by equation 5.1 to the absorption spectra of the two IM forms. This way the amplitude, frequency position and width of the individual pulses were obtained. These parameters of the absorption peaks are listed in Table 6.

Table 6. The extracted Gaussian peak properties: amplitude (G), peak frequency position (ν_0), and width ($\Delta\nu$) for the individual absorption peaks. In the upper and bottom table part, peaks corresponding to the γ-IM and α-IM are listed, respectively.

Peak	G (cm^{-1})	ν_0 (THz)	$\Delta\nu$ (THz)
γ_1	12.5	1.24	0.07
γ_2	1.7	1.48	0.07
α_1	2.0	0.76	0.05
α_2	2.0	0.86	0.05
α_3	5.0	1.24	0.08
α_4	10.2	1.49	0.08

In addition to the two crystalline forms, an amorphous IM sample was also prepared and investigated. Amorphous IM was prepared by melting γ-IM and subsequently quench cooling the melt. For this the γ-IM powder was placed into a cylindrical holder made from metal which was then placed onto a hot plate and heated up to 165 °C. After the powder melted, the holder with the melt was placed into a container with liquid nitrogen. The obtained amorphous IM sample retained the disk-like shape of the holder after removing it from the holder. Therefore, no pressing of the amorphous IM sample was needed prior to the THz TDS investigation. The obtained absorption coefficient (see Figure 17) of the amorphous IM was continuously increasing with increasing frequency and no absorption features could be observed as expected according to the previous investigations of amorphous IM [16,107].

The fact that amorphous IM does not show any absorption features in the investigated frequency range and that the two crystalline forms show distinct absorption features can be used to identify crystalline IM in the tablets made from smartFilms. Furthermore, having the parameters of the individual absorption peaks of the two crystalline forms extracted allows for quantitative assessment of the amount of crystalline and amorphous IM in the paper tablets. The preparation of smartFilms tablets, their corresponding physical mixtures, and the crystallinity assessment of IM in the prepared samples is presented in the following section.

6.2 Crystallinity assessment of IM in paper tablets

SmartFilms were prepared by loading IM into a coffee filter paper (Filtertüte 1x6/40 naturbraun, Melitta Europa GmbH & Co. KG, Germany), which was also used for the investigation discussed in chapter 4. The general concept of smartFilms and their preparation was discussed in more detail in subsection 3.4.3. In short, the coffee filter paper was first cut into smaller pieces of circular shape with a diameter of 60 mm. γ-IM was dissolved in a mixture of ethanol (75 mol%) and acetone (25 mol%) since the solubility of IM is increased when the two solvents are mixed compared to the usage of pure individual solvents [223]. 500 µl of the prepared stock solution (28.27 mg/ml) were then applied into the middle of each circular filter paper. This resulted in 14.14 mg of IM being loaded into the smartFilms, which corresponds to 0.5 mg/cm² per loading cycle. After the smartFilms were dry, the loading cycle was repeated from two to ten times in total resulting in smartFilms with loadings of 1, 2, 3, 4, and 5 mg/cm², respectively. For each loading three smartFilms were prepared resulting in 15 samples in total. The overview of the prepared samples is listed in Table 7.

Table 7. Overview of the prepared smartFilms. All samples were prepared in triplicate. The area of individual smartFilms was approximately 28 cm^2.

Number of loading cycles	m_{IM} (mg)	IM content (mg/cm²)	IM content (w%)
2	28.27	1	13
4	56.54	2	23
6	84.81	3	31
8	113.08	4	37
10	141.35	5	43

The prepared smartFilms were then individually transferred into tablets for the subsequent THz investigation. For this, they first needed to be cut into smaller pieces of approximately 16 mm by 16 mm in size to fit the press (Model No. GF-10B Cl. 1.0, Enerpac, Germany). Then they were pressed into tablets by applying a force of 60 kN for 90 s. Additionally, physical mixtures were prepared as a positive control by mixing milled coffee filter paper with γ-IM in the mass proportions corresponding to those in the smartFilms. The prepared mixtures were also pressed into tablets. Furthermore, two additional types of paper tablets without any IM were prepared. The first type was prepared by pressing small cut pieces of coffee paper corresponding to smartFilms with 0 w% IM content. The second type was prepared by compressing the milled coffee filter paper and as such corresponds to the physical mixture with 0 w% IM content. Therefore, these two sample types can be considered as a negative control. All the obtained tablets had a diameter of approximately 13 mm and had a thickness ranging from 0.6 to 2 mm. The THz investigation of the tablets followed within several days after the samples were prepared and was conducted with the same THz TDS system and in the same way as for the pure IM samples as discussed in section 6.1. The obtained absorption spectra are shown in Figure 40.

On the left-hand side of the figure the absorption spectra of physical mixtures are shown. In the absorption spectrum of a tablet made only from the milled paper without any addition of IM, shown in the most bottom panel on the left, no distinct absorption features can be observed in the investigated frequency range. However, when the γ-IM content is increased, the 1.24 THz absorption peak can be observed and it becomes more pronounced with the increasing γ-IM content. γ-IM exhibits an additional absorption peak at approximately 1.5 THz. This peak, however, cannot be clearly observed in the physical mixtures, also in the case of the highest γ-IM content. This is not unexpected, since this absorption peak is much weaker compared to the absorption peak at 1.24 THz (see Table 6). Furthermore, with an increasing γ-IM content, an overall decrease in the absorption coefficient values can be observed. This can be attributed to the fact that the overall absorption of IM in this frequency range is lower than the absorption of the paper (see Figure 32 b) and Figure 34). Additionally, by mixing the two powders, the scattering processes might be affected which could influence the extracted values of the absorption coefficient.

On the right hand-side of Figure 40 the absorption spectra for tablets made from smartFilms are shown. For the tablets made from coffee filter paper (see the most bottom panel) containing no IM, again no distinct absorption features can be observed in the investigated frequency range. The same is true for the tablets made from smartFilms containing 13 w% of IM. This indicates that IM remained amorphous, which is desired in terms of improved solubility. For higher IM content, absorption peaks can be observed. However, in the case of tablets made from smartFilms the absorption peak at approximately 1.5 THz is more pronounced than the peak at 1.24 THz, which corresponds to the α-IM (see Table 6). Furthermore, two additional peaks at 0.76 and 0.86 THz can be observed compared to the physical mixtures. These two peaks are exhibited by α-IM but not the γ-form (see Figure 39). This means that the smartFilms converted into tablets were able to maintain IM amorphous for the lowest IM content and that for higher contents IM at least partially crystallized, however, as α-IM, which still offers improved solubility compared to the initially and more commonly used γ-form.
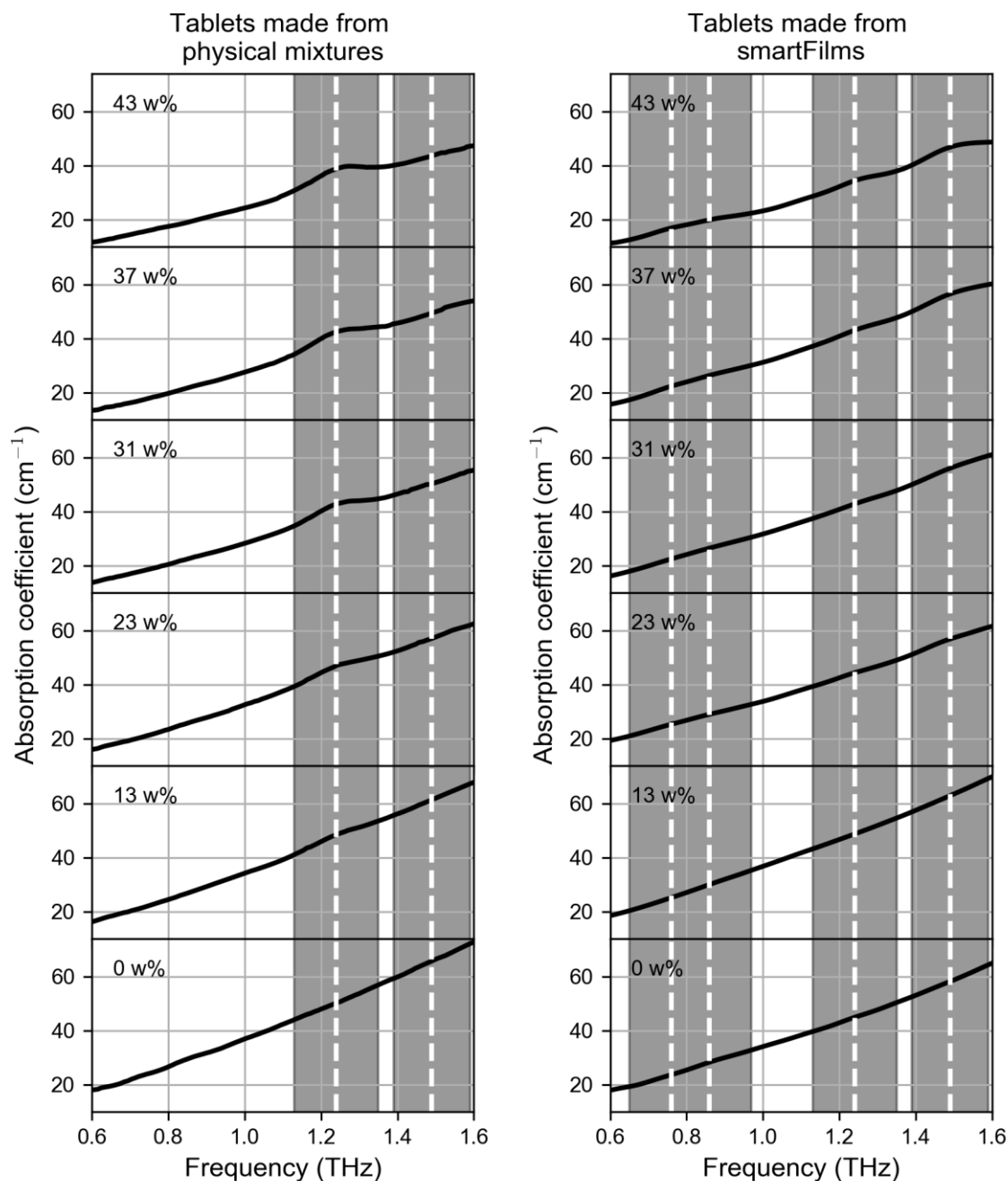
Figure 40. Absorption spectra for tablets made from physical mixtures (left) and smartFilms (right) with increasing IM content from bottom to top. The grey shaded areas with white vertical dashed lines indicate the position of the absorption peaks exhibited by crystalline IM. Note that the two peaks at 0.76 and 0.86 THz corresponding to the α-IM appear only for tablets made from smartFilms. The IM content is indicated in the individual panels. For clarity, the results only for a single sample per each IM content are shown.

By comparing the absorption coefficient of the two 0 w% samples, one can notice that the absorption coefficient of the sample corresponding to the physical mixtures is greater than that of the sample corresponding to the smartFilms. The reason for this difference is that the sample, which is part of the physical mixtures, is prepared by pressing milled coffee filter paper into a tablet whereas the other 0 w% sample was prepared by pressing smaller pieces of coffee filter paper. Consequently, this can lead to different scattering

of the THz radiation passing through the sample, which leads to the difference in the determined absorption coefficient. Furthermore, milling of the filter paper led to its amorphization which also leads to different absorption properties (see Figure 34).

The absorption spectra of the tablets made from physical mixtures and smartFilms shown in Figure 40 were analyzed further with the goal to estimate the amount of crystalline and amorphous IM. This was done by describing the absorption spectra as a sum of the background absorption and a linear combination of α- and γ-IM absorption peaks. The following function was, therefore, fitted to the individual absorption spectra:

$$f(v) = A \sum_{i=1}^{2} G_{\gamma_i} e^{-\frac{\left(v - v_{0,\gamma_i}\right)^2}{2\Delta v_{\gamma_i}^2}} + B \sum_{i=1}^{4} G_{\alpha_i} e^{-\frac{\left(v - v_{0,\alpha_i}\right)^2}{2\Delta v_{\alpha_i}^2}} + O(2), \qquad 6.2$$

where $O(2)$ is the second order polynomial used for describing the background absorption, G_{α_i}, v_{0,α_i}, Δv_{α_i} are amplitude, frequency position and width of the i-th α-IM absorption peak, respectively, and G_{γ_i}, v_{0,γ_i}, Δv_{γ_i} are amplitude, frequency position and width of the i-th γ-IM peak, respectively. These peak parameters were extracted from the analysis of the α- and γ-IM absorption spectra (see section 6.1) and were kept fixed when fitting the spectra. This means that only the values of the second order polynomial and coefficients A and B were evaluated when fitting the function $f(v)$ to the absorption spectra. Fit coefficients A and B are related to the amount of γ- and α-IM in the samples. The obtained values of the two fit coefficients for the tablets made from physical mixtures and smartFilms are shown in Figure 41.
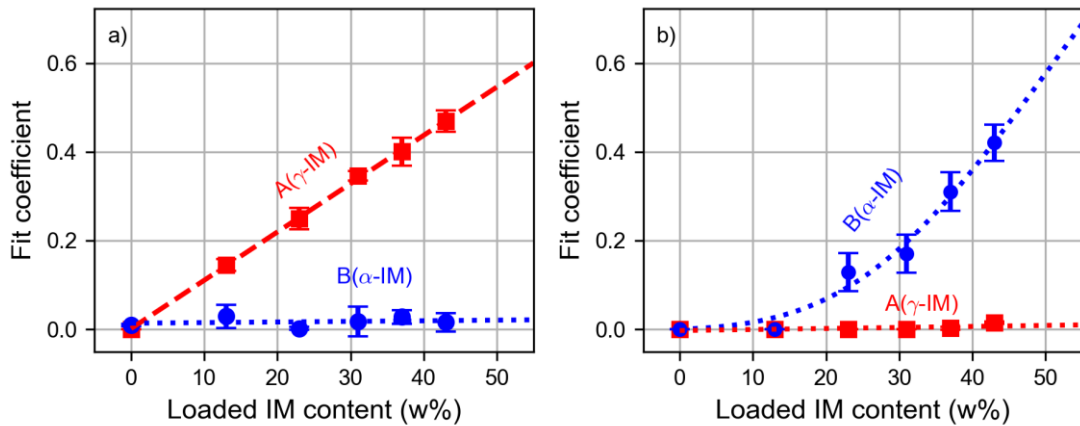
Figure 41. Fit coefficients A (red squares) and B (blues circles) for tablets made from a) physical mixtures and b) smartFilms. The dashed red line represents a linear fit whereas the dotted lines are only a guide-to-the-eye. The error bars correspond to the standard deviation of the repeated estimation of the fit coefficients.

In the case of tablets made from physical mixtures the fit coefficient A increases linearly with the amount of loaded IM content, whereas the fit coefficient B is approximately zero regardless of the IM content. This outcome is expected considering that the physical mixtures were prepared by mixing milled coffee filter paper and γ-IM powder and that the fit coefficient A corresponds to the γ-form, whereas the fit coefficient B corresponds to the α-IM, which was not used in the physical mixtures. This also agrees with the

observations made above based on the absorption features of the physical mixtures in Figure 40.

In the case of tablets made from smartFilms the obtained values of the two fit coefficients show a substantially different trend compared to the case of physical mixtures. The values of fit coefficient A remain approximately zero regardless of the IM content loaded into the smartFilms. Furthermore, the fit coefficient B remains zero for the lowest IM content and then increases non-linearly for higher IM content. This again agrees with the observations made based on the absorption spectra shown in Figure 40 and confirms that the smartFilms maintained IM amorphous for the lowest content. Furthermore, for higher IM content, smartFilms were not able to maintain all the IM amorphous. Nevertheless, the crystalline IM was of α-form, which is still better soluble in aqueous media compared to the initially used γ-form.

Since the amount and the form of the IM in the tablets made from physical mixtures is known, this information can be used to relate the values of the fit coefficients with the amount of the loaded IM in the samples in terms of a conversion factor. The conversion factor was determined as the slope of the fitted line (i.e., linear function) to the values of the fit coefficient A in Figure 41 a). The value of the slope was determined as 0.0109 (w%)$^{-1}$. By dividing the values of the extracted fit coefficients with the conversion factor, the amount of crystalline IM in terms of γ- and α- form could be estimated. Furthermore, since the total amount of IM in the samples was known, the amount of the amorphous IM could be determined as the difference between the loaded content of IM and the content of the two crystalline forms. The results of the IM content assessment in the samples based on the THz TDS investigation is shown in Figure 42
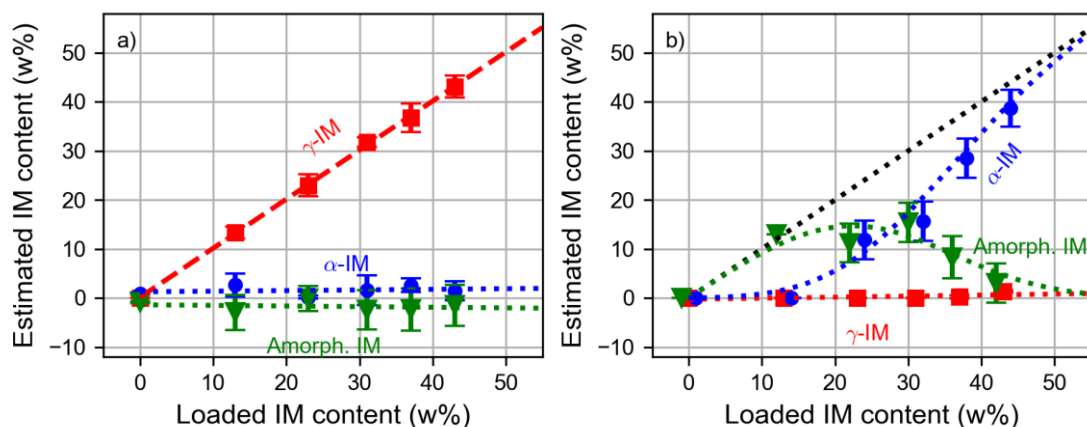
Figure 42. Estimated IM content in tablets made from a) physical mixtures and b) smartFilms. The red squares, blue circles, and green triangles indicate values of γ-, α-, and amorphous IM, respectively. The dashed red line represents the linear fit. The dotted lines are a guide-to-the-eye. Note that to achieve a clearer representation in panel b) the green and blue value markers were shifted by +1 % and -1 % in the horizontal direction, respectively. The error bars correspond to the standard deviation of the repeated estimation of the IM content.

For the physical mixtures the conversion of the values of the two fit coefficients reveals that the IM in the physical mixtures was of the γ-form. Furthermore, the estimated amount of the α-form and amorphous IM remains zero within the measurement repeatability, which is indicated by the error bars in the Figure 42. This is again expected since γ-form

was used for preparation of the physical mixtures. In the case of tablets made from smartFilms, the estimation of the crystalline and amorphous forms of IM reveals that for the lowest content of IM, smartFilms maintained IM amorphous. Furthermore, when the amount of IM is increased, the amount of the amorphous IM does not proportionally increase. This indicates that there is a certain loading limit up to which smartFilms can maintain IM amorphous. The data suggests that this limit is at approximately 15 w% for IM loaded into the selected coffee filter paper. For higher content of loaded IM, part of the IM remains amorphous and part of it recrystallizes as the α-form. If the content of the loaded IM is increased even further, the amount of the amorphous IM decreases and the majority of IM recrystallizes as α-IM. The data reveals that increasing the content of the loaded IM can cause initially amorphous IM to recrystallize. Since smartFilms can be considered as a special type of solid dispersions, as discussed in section 3.4, the recrystallization of initially amorphous IM is not unexpected when the amount of IM is additionally increased. The increase of loaded IM content increases the possibility that initially molecularly dispersed IM can interact with the additionally added IM and forms crystalline clusters. Nevertheless, IM loaded into the smartFilms recrystallizes as the α-form, which is better soluble compared to the initially used γ-form. Furthermore, recrystallization of IM after being dissolved in different solvents as well as different sample treatment can result in the formation of different polymorphic forms [223–225]. Therefore, the formation of α-IM can be considered unrelated to the paper matrix of the smartFilms [226].

The tablets made from smartFilms were investigated also one year after they had been prepared. Since for each IM content a tablet was destroyed during an XRD investigation [227], two tablets per loaded IM content remained for the THz TDS investigation one year after the sample preparation. Figure 43 shows the estimated IM content for the samples being stored in a refrigerator at a temperature of approximately 5°C for one year. Additionally, the estimated IM content of the same set of samples few days after preparation is shown for an easier comparison.
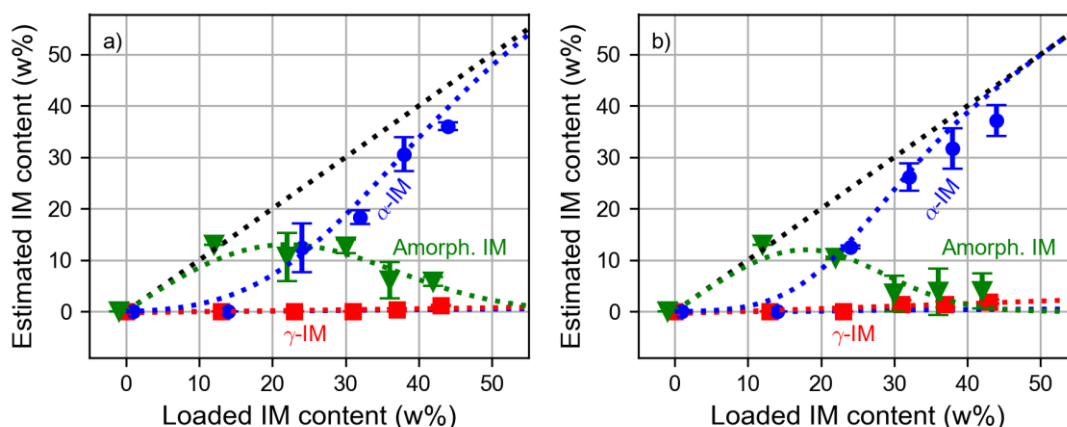
Figure 43. Estimated IM content in tablets made from smartFilms investigated a) few days after being prepared and b) one year after being prepared. The red squares, blue circles, and green triangles indicate values of γ-, α-, and amorphous IM, respectively. The dotted lines are a guide-to-the-eye. Note that only two samples per loaded IM content were considered in the analysis and that the error bars correspond to the estimated IM content difference between the two samples.

To achieve a clearer representation, the green and blue value markers were shifted by +1 % and -1 % in the horizontal direction, respectively.

The estimated IM content in the samples being stored for a year reveals a similar outcome in terms of crystalline and amorphous IM content compared to the investigation a few days after the sample preparation. Especially, for the two lowest loaded IM content (i.e., 13, and 23 w%) the amount of the two crystalline polymorphs as well as amorphous IM seems to remain unchanged during the storage. However, for higher loadings, the data suggests that the amount of crystalline IM increased and consequently the amount of the amorphous IM in the samples decreased. Furthermore, for the loaded IM content exceeding 23 w%, a slight increase in the amount of γ-IM content can be observed. This indicates that with time either α-IM or the remaining amorphous IM tend to recrystallize into the γ-form in the case of higher loaded IM content. However, for the lower loaded IM content, smartFilms seem to efficiently inhibit crystallization of the amorphous IM and transformation of α-IM into γ-IM during the first 12 months after being prepared and stored in a refrigerator.

In summary, THz TDS investigation of IM in tablets made from smartFilms revealed that IM in such formulations remains amorphous up to a content of approximately 15 w%. For higher content of IM, the smartFilms fail to maintain IM completely amorphous, which can be expected since the increased IM content increases the possibility for IM molecules to interact with one another and form crystalline clusters. Nevertheless, the crystallization of IM resulted in the formation of the α-form, which still offers superior solubility compared to the initial γ-form, however, inferior to the amorphous IM [7]. Furthermore, the investigation of the same samples one year after being prepared revealed that for higher IM content the amount of amorphous IM decreased even further. Furthermore, it seems that a small part of the loaded IM transformed into its γ-form. However, for the lower loaded IM content of up to 23 w% the data suggests that the samples did not change in terms of IM crystallinity, which underlines the capability of smartFilms to efficiently inhibit crystallization of amorphous IM up to a certain loading. Finally, the results presented in this chapter reveal that THz TDS is a powerful tool for non-destructive, qualitative and quantitative investigation of the solid state of pharmaceuticals loaded into a paper matrix.

The approach for the crystallinity assessment of IM in the paper matrix introduced in this chapter can be transferred to further APIs which exhibit distinct absorption features. In the following chapter the crystallinity assessment of NIF dispersed into a cellulose matrix is presented.

7   Nifedipine dispersed in a cellulose matrix

NIF is a calcium channel blocker used for treatment of high blood pressure as well as angina [191–193]. Due to its poor aqueous solubility it belongs to the BCS class II. This means that by increasing its solubility, improvement of its bioavailability can be expected. As such, NIF has been widely employed as a model API when considering the solubility advantage of amorphous drugs in pharmaceutical formulations as well as when studying recrystallization of amorphous drugs [193,228–233]. Furthermore, THz TDS has been employed to monitor recrystallization of amorphous NIF dispersed in PVP [110]. Additionally, THz TDS investigation of NIF-isonicotinamide cocrystal formulations [234] and estimation of NIF crystallinity in aqueous suspensions has been demonstrated [235]. NIF exhibits a strong absorption feature centered at 1.2 THz and a weaker absorption peak at approximately 2.2 THz when in crystalline state (see Figure 32) [110,197,235]. Furthermore, when amorphous, it shows a featureless, continuously increasing absorption in the frequency range between 0.3 and 2.5 THz [110,197].

In this chapter the focus lies on the inspection of the solid state of NIF dispersed in a cellulose matrix using THz TDS. The goal is again to maintain the API in its amorphous state, which provides improved aqueous solubility. For this the same smartFilms approach as in the case of IM and LTA (see chapters 4 and 6) is considered. Furthermore, an extended approach combining the idea of loading an API into the paper matrix and dispersing the API in an additional carrier is employed to improve the performance in terms of the amount of the amorphous API in the formulation as well as improved inhibition of recrystallization. Additionally, loading NIF directly into pressed MCC powder instead of using sheets of paper was considered. All these different formulations of dispersed NIF were pressed into tablets and investigated using a THz TDS system in the transmission configuration. For the crystallinity assessment of the different NIF formulations, first the absorption features of NIF were characterized and then physical mixtures with different proportions of NIF and MCC were prepared and analyzed to obtain the conversion factor for the crystallinity assessment. This part is presented in the next section of this chapter.

7.1   THz TDS of NIF and physical mixtures

NIF (abcr GmbH, Germany) powder was used as received to first prepare three tablets for the THz TDS investigation. For each tablet approximately 120 mg were pressed using a manual hydraulic press (Model No. GF-10B Cl. 1.0, Enerpac, Germany) with a force of 30 Kn for 90 s. The obtained biplanar tablets had a diameter of 13 mm and were approximately 700 µm thick. THz measurements were performed under nitrogen atmosphere with a fiber-coupled THz TDS system [30] using a pair of PCAs and four OAPMs. The samples were positioned in the focal plane and measured in the middle of the sample five consecutive times. Prior to the sample measurements, five reference measurements were performed without a sample in the beam path. Additionally, amorphous NIF was prepared by quench-cooling melted NIF. Crystalline NIF was first placed in a metal holder. The holder with NIF was then placed on a hot plate which was set to 183 °C until NIF completely melted. Then the melt was left to cool down in the holder at room temperature. The obtained amorphous NIF sample kept its shape of a biplanar tablet after being extracted from the holder. This way no further processing was

required prior to the THz investigation. The absorption coefficient of all the samples was evaluated using the TeraLyzer software (see subsection 2.1.2). The extracted absorption coefficients for a single crystalline and amorphous NIF samples for the frequency range of 0.6 to 1.7 THz are shown in Figure 44.
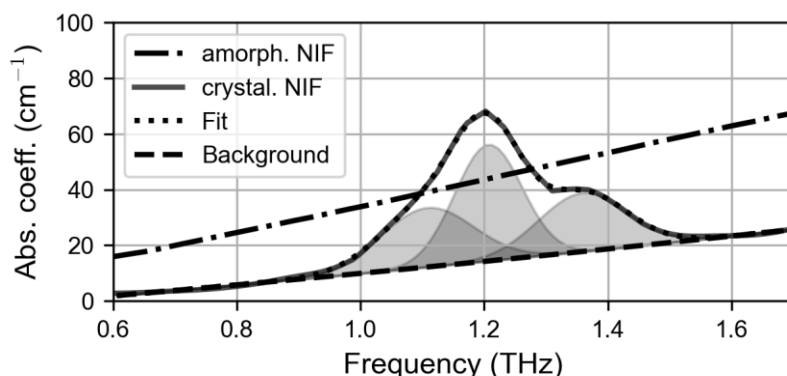
Figure 44. Absorption coefficient of amorphous (dashed-dotted line) and crystalline (solid line) NIF. The absorption spectrum of the crystalline NIF was modeled (dotted line) as the sum of second order polynomial for the background absorption (dashed line) and of three Gaussian peaks (shaded areas).

On the one hand, the amorphous NIF shows a featureless absorption spectrum in the shown frequency range. On the other hand, crystalline NIF shows a broad absorption feature centered approximately at 1.2 THz. This absorption feature can be described by three individual Gaussian peaks and the whole absorption spectrum as a sum of the three Gaussian peaks and second order polynomial The latter is used to describe the continuous background absorption (see section 5.3). Therefore, function described in the equation 5.1 with $N = 3$ was fitted to the absorption spectrum to obtain the absorption peak properties. These are listed in Table 8.

Table 8. The extracted Gaussian peak properties: amplitude (G), peak frequency position (ν_0), and width ($\Delta\nu$) for the individual absorption peaks. The provided deviation of the peak parameters corresponds to the standard deviation calculated from the evaluation of the three crystalline NIF samples.

Peak	G (cm^{-1})	ν_0 (THz)	$\Delta\nu$ (THz)
1	23 ± 4	1.11 ± 0.02	0.08 ± 0.01
2	43 ± 7	1.205 ± 0.003	0.056 ± 0.002
3	20.7 ± 0.3	1.360 ± 0.001	0.069 ± 0.002

Following the characterization of pure NIF samples, physical mixtures of crystalline NIF and MCC (Carl Roth GmbH + Co. KG, Germany) were prepared in different weight proportions. For each weight proportion three tablets were prepared by pressing the powder mixture for 90 s with a force of 30 kN before the THz TDS investigation. The obtained absorption spectra were then individually described as the sum of a second

order polynomial and the sum of the three absorption peaks with the fixed peak properties (see Table 8) multiplied by a coefficient A. The coefficient A was then obtained by fitting the following function to the absorption spectra of the individual tablets made from physical mixtures:

$$f(v) = A \sum_{i=1}^{3} G_i e^{-\frac{(v-v_{0,i})^2}{2\Delta v_i^2}} + O(2),$$ 7.1

where $O(2)$ is the second order polynomial used for describing the background absorption, G_i, $v_{0,i}$, Δv_i are amplitude, frequency position, and width of the i-th absorption peak of the crystalline NIF. The extracted fit coefficient A with respect to the content of crystalline NIF in the physical mixtures is shown in Figure 45.
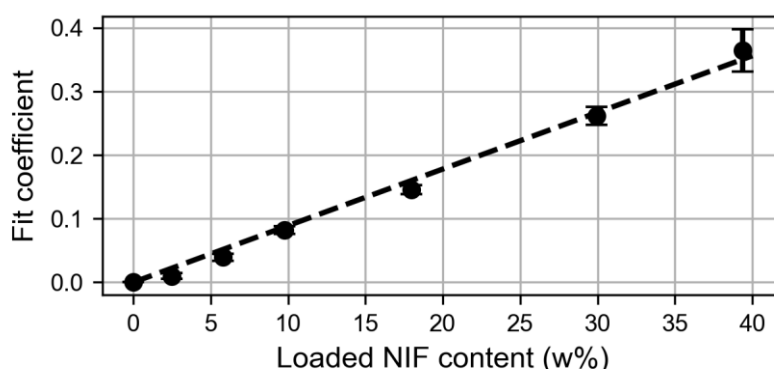
Figure 45. Fit coefficient A as a function of the NIF content in the physical mixtures. The dashed line with slope of 0.0089 (w%)$^{-1}$ corresponds to the linear fit. The error bars correspond to the standard deviation of the fit coefficient extracted individually for the three samples per NIF content.

The extracted values of the fit coefficient A increase linearly with the increasing NIF content. By fitting a linear function to the values shown in Figure 45 a conversion factor between the crystalline NIF content and the fit coefficient A can be determined as the slope of the fitted line. The fit was obtained while considering a fixed intercept at values of fit coefficient and NIF content both being zero. The value of the slope was determined as 0.0089 (w%)$^{-1}$. The obtained conversion factor can be used to estimate the amount of crystalline NIF when dispersed in a cellulose matrix. Since paper mainly consists of cellulose and, therefore, also shows similar absorption properties as cellulose in the investigated frequency range (see Figure 34), the same conversion factor is used for the assessment of the amount of the crystalline NIF in the tablets made from smartFilms. The assessment of crystalline NIF content in the tablets made form smartFilms with and without PVP is presented in the following section.

7.2 NIF in smartFilms with and without PVP

To disperse NIF in a paper matrix and thereby keeping it amorphous two different approaches using coffee filter paper (Filtertüte 1x6/40 naturbraun, Melitta Europa GmbH & Co. KG, Germany) were employed. The first approach follows the common way of preparing smartFilms. First the coffee filter paper was cut into smaller circular pieces with a diameter of 40 mm. Then NIF was dissolved in a 1:1 volume mixture of acetone and

ethanol to obtain a NIF stock solution with concentration of 15 mg/ml. Then three smartFilms with a NIF content of 5 w% were prepared by applying 295 µl of the stock solution per individual sample. To prepare smartFilms with 10 w% and 15 w% NIF content, two and three loading cycles were performed, respectively. In each loading cycle 310 µl of the stock solutions were applied to obtain 10 w% NIF content and 330 µl to obtain 15 w% NIF content. The individual smartFilms were then cut into smaller pieces and pressed into tablets with a hydraulic press (Model No. GF-10B Cl. 1.0, Enerpac, Germany) by applying force of 30 kN for 90 s. The resulting tablets had a diameter of 13 mm and thickness ranging from 480 to 650 µm.

The second approach of dispersing NIF in a paper matrix differed from the conventional way of preparing smartFilms in a way that PVP was used as an additional carrier to improve the performance of the formulation. Stock solution was prepared by dissolving NIF and PVP in the 1:1 acetone-ethanol mixture. The mass ratio of NIF to PVP was 4:1 and the corresponding concentration was 16 and 4 mg/ml, respectively. The 4:1 ration of NIF with respect to PVP was chosen based on previous investigation of dispersing NIF solely in PVP [110]. Again, circular pieces with a diameter of 40 mm were cut from the same coffee filter paper basis. Samples with three different NIF content (5, 10, and 15 w%) were prepared by repeating the loading cycle up to three times by applying an appropriate volume of the stock solution. For each selected NIF content three individual samples were prepared. The NIF content was defined with respect to the total mass of the sample. Therefore, the mass of NIF in these samples is somewhat greater compared to the conventional smartFilms with the same relative NIF content since PVP adds to the total mass of the samples (see Table 9). The loaded paper samples were again cut into smaller pieces and pressed into tablets.

Table 9. Volume of the applied solution (V), mass of loaded NIF (m_{NIF}), and loaded NIF content (c_{NIF}) per loading cycle (N) for samples with and without PVP in the right and left part of the table, respectively. Note that the applied volume could be set in steps of 5 µl according to the resolution of the used pipet.

N	Without PVP			With PVP		
	V (µl)	m_{NIF} (mg)	c_{NIF} (w%)	V (µl)	m_{NIF} (mg)	c_{NIF} (w%)
1	295	4.4	5.0	280	4.5	5.0
2	310	9.3	10.0	300	9.6	10.1
3	330	14.9	15.1	325	15.6	15.2

All tablets were investigated using a THz TDS transmission setup under nitrogen atmosphere the same way as the pure NIF and physical mixture samples in section 7.1. The absorption coefficients of the samples were evaluated using the TeraLyzer software. The same way as for physical mixtures the obtained absorption spectra were described as the sum of a second order polynomial and of the three characteristic absorption peaks for the crystalline NIF. The second order polynomial was again used to describe the continuous background absorption. Since PVP also shows a continuous featureless absorption (see Figure 35), the contribution of the PVP to the absorption of the samples was also included in the second order polynomial. The amplitude of the three absorption peaks was scaled by a coefficient A, which was extracted by fitting the function $f(v)$ (see equation 7.1) to the individual absorption spectra. The obtained fit coefficient was divided

by the conversion factor obtained from the analysis of the physical mixtures (see Figure 45). This way the amount of crystalline NIF in the samples was determined. The amount of crystalline NIF in the samples few days after being prepared is shown in Figure 46.
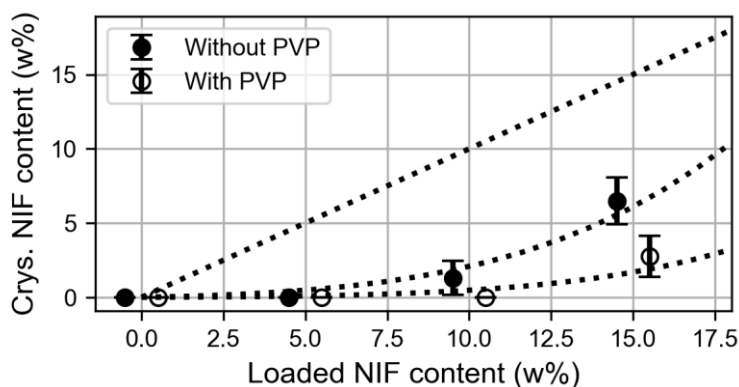
Figure 46. Crystalline NIF content with respect to the loaded NIF content for samples with (empty circles) and samples without (filled circles) PVP. The error bars correspond to the standard deviation calculated based on the crystallinity evaluation of three samples per loaded NIF content. Note that for clearer representation the value markers for samples with and without PVP are artificially shifted for +1 w% and -1 w% in the horizontal direction, respectively. The dotted curves are only guide-to-the-eye. The straight dotted line indicates the expected values if all loaded NIF was crystalline.

The assessment of NIF crystallinity based on the THz TDS investigation reveals that no crystalline NIF was present in the samples without PVP for the lowest loading of 5 w%. This means that the whole loaded NIF remained amorphous in the samples with 5 w% NIF content. For higher loadings part of the NIF recrystallized. When PVP was additionally used in the solution during the loading process, NIF remained amorphous up to the NIF content of 10 w%. For the highest loading it again partially recrystallized. However, the content of crystalline NIF was smaller compared to the samples without PVP. This indicates that addition of PVP into the formulation improved the capability of paper to maintain NIF amorphous. These results reveal that using an additional carrier when loading APIs into the paper matrix can improve the capability of the formulation to maintain the API amorphous without making the loading process more complicated and time consuming. After the initial THz TDS investigation of the prepared samples was completed, the samples were stored in a refrigerator at approximately 5 °C. The samples were then investigated again three and six months after they had been prepared. The evaluation of the crystalline NIF content in the samples after three and six months after the samples had been prepared is shown in Figure 47.
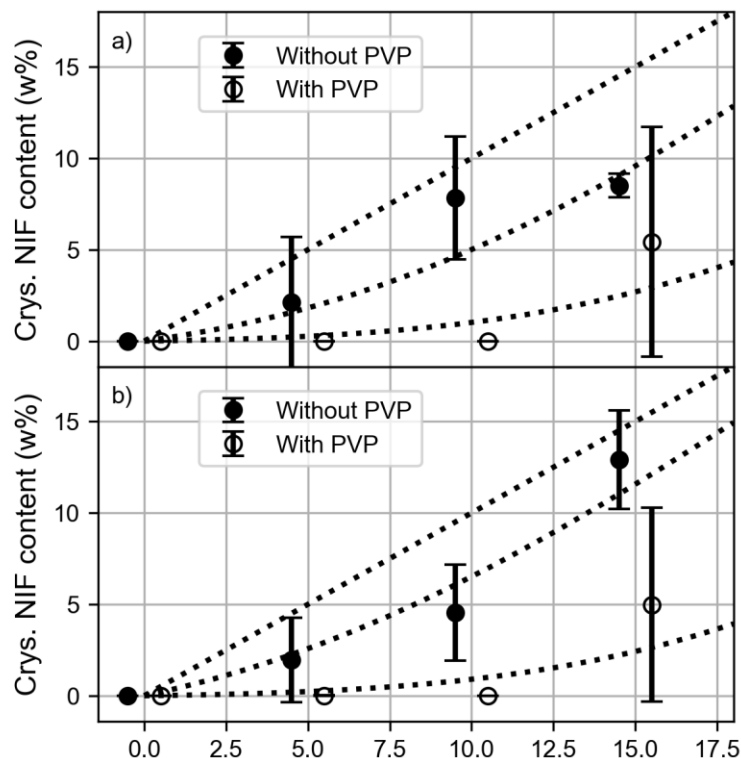
Figure 47. Crystalline NIF content for samples evaluated a) three months and b) six months after they had been prepared for samples with (empty circles) and without (filled circles) PVP. The error bars correspond to the standard deviation calculated based on the crystallinity evaluation of three samples per loaded NIF content. Note that for clearer representation the value markers for samples with and without PVP are artificially shifted for +1 w% and -1 w% in the horizontal direction, respectively. The dotted curves are only guide-to-the-eye. The straight dotted lines indicate the expected values if all loaded NIF was crystalline.

The investigation three months after preparation of the samples revealed that for samples without PVP, crystalline NIF was present also in the samples with the lowest content of loaded NIF (i.e., 5 w%). This means that NIF, which was initially maintained completely amorphous, partially recrystallized during the storage of the samples. For samples with higher loadings the estimated amount of crystalline NIF also increased compared to the freshly prepared samples. For samples with added PVP the data shows that no crystalline NIF was present in the samples with 5 and 10 w% of loaded NIF content. This indicates that the addition of PVP into the formulations improved their capability to inhibit the recrystallization of NIF. However, for samples with the highest loaded NIF content, which already initially contained some crystalline NIF (see Figure 46), the average amount of crystalline NIF also increased. For samples containing crystalline NIF, the evaluation of crystalline content also yielded a greater variation between the individual samples with the same loading resulting in greater error bars compared to the evaluation of fresh samples. This was the case for both sample types (i.e., with and without PVP). The investigation after six months revealed a similar outcome compared to the investigation after three months. In all samples without PVP crystalline NIF was present. For the samples with PVP, this was again the case only for the highest loading of 15 w%, whereas for 5 and 10 w% NIF remained amorphous.

The main message based on the results presented in this section is that the addition of an extra carrier (e.g., PVP) when dispersing an API (e.g., NIF) into a paper matrix can improve the capability of the formulation to maintain the API amorphous. Furthermore, the capability of the formulation to inhibit recrystallization of the amorphous API over a longer time period can be increased this way as well. The presented approach can be simply extended to other APIs and carriers. The main requirement is that the carrier and the API can be sufficiently dissolved in the same solvent, which subsequently evaporates from the paper matrix. Furthermore, the whole process of preparing the formulation with an additional carrier remains relatively straightforward the same way as the preparation of smartFilms. Using an extra carrier, which unlike cellulose readily dissolves after administration, could also provide an additional advantage compared to the conventional smartFilms in terms of inhibiting nucleation and crystal particle growth after the drug dissolution as discussed in subsection 3.4.2. Finally, the non-destructive nature of THz TDS in combination with the presented estimation of crystalline content enables stability testing of the formulations using the same set of samples.

So far in this work coffee filter paper, which mainly consists of cellulose, was used for preparation of samples containing amorphous APIs. In the following section the investigation of MCC pressed into tablets as a potential carrier for amorphous NIF is presented.

7.3 NIF in tablets made from MCC

As discussed in subsection 3.4.2 smartFilms can be considered a special type of a solid dispersion involving porous materials as the carrier. Porous materials offer high surface area per mass ratio, which enables better adsorption of the API molecules to the surface and consequently high drug loading in the amorphous form. This in turn leads to better solubility of the drug and consequently improved bioavailability. For the production of smartFilms conventional paper is used as the carrier, which mainly consists of cellulose. The idea of the investigation presented in this section is to test, if the tablets made directly from cellulose powder can also maintain NIF amorphous. To do so, MCC (Carl Roth GmbH + Co. KG, Germany) was first pressed into tablets, which were subsequently loaded with NIF by applying a NIF solution on the tablets and letting the solvent evaporate. The sample preparation procedure is schematically presented in Figure 48.

In total four tablets loaded with NIF were prepared. For each tablet approximately 120 mg of MCC were inserted into a hydraulic tablet press. Then a force of 10 kN was applied for 90 s. The resulting tablets were approximately 0.8 mm thick and had a diameter of 13 mm. Then the tablets were investigated the same way and by using the same THz TDS transmission setup as discussed in the previous section. The absorption coefficient as well as the tablet thickness were evaluated using the TeraLyzer software (see subsection 2.1.2). After the initial THz investigation, the cellulose tablets were loaded with NIF by applying 40 µl of the stock solution on the flat surface of the tablets. A volume of 40 µl was selected as it was sufficient to wet the whole tablet and at the same time the tablets were capable to entirely soak this volume of pure solvent. The stock solution was prepared by dissolving NIF in acetone to a concentration of 0.13 g/ml. Applying 40 µl of the stock solution, therefore, resulted in approximately 5.2 mg of NIF loaded into the tablet per loading cycle. It is worth noting that also the stock solution wetted the whole

tablets as the whole surface including the opposite flat part of the tablet became wet. Furthermore, the surface of initially white tablets became yellow, which is the color of NIF.
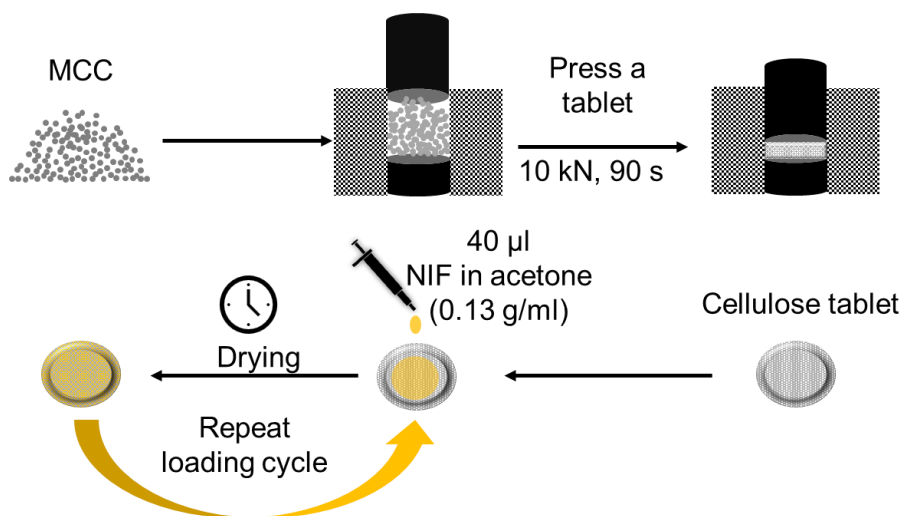
Figure 48. Sample preparation procedure. Before and after each loading cycle samples were investigated using THz TDS.

After applying the solution individually on all four tablets, the tablets were left to dry at room temperature. After being dry, the loaded tablets were again investigated using the THz TDS setup. Then the loading cycle was repeated by again applying 40 µl of the stock solution onto the flat side of the tablets. However, this time the solution was applied onto the opposite flat side of the tablets. After being dry, the THz TDS investigation of the tablets was repeated. The whole loading cycle was repeated in total four times. Note that for every loading cycle the solution was applied to the opposite flat tablet surface compared to the previous loading cycle. Furthermore, the tablets were weighted (Kern ARS 220-4, Kern & Sohn GmbH, Germany) before and after each loading cycle to control the mass of the loaded NIF.

From the obtained absorption spectra, the amount of crystalline NIF was assessed. This was done in the same way as for tablets made from smartFilms as discussed in section 7.2. Figure 49 shows the results of the THz investigation in terms of the amount of crystalline NIF in the cellulose tablets and the increase of tablet thickness determined based on the TeraLyzer thickness evaluation.
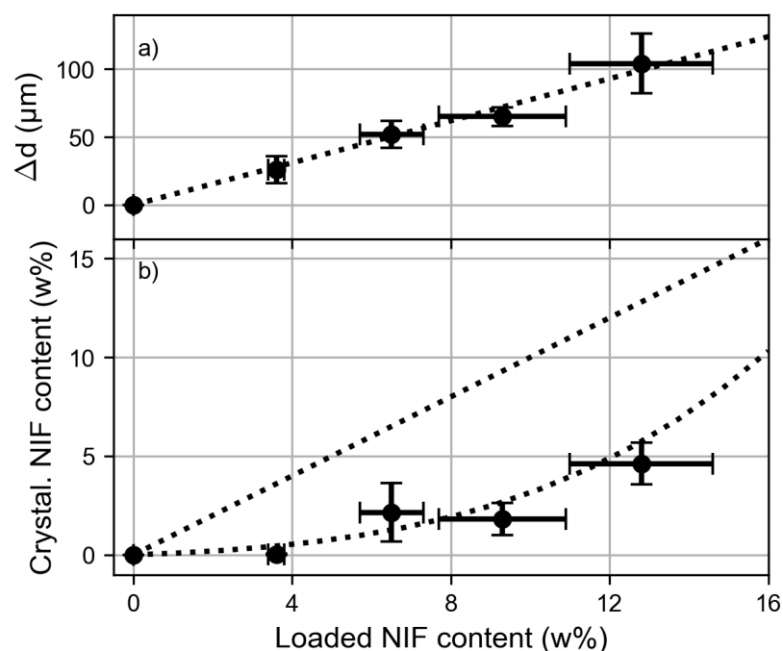
Figure 49. a) Sample thickness difference after each loading cycle. b) Estimated crystalline NIF content for cellulose tablets loaded with NIF. The dotted lines are a guide-to-the-eye. The straight dotted line in b) indicates the expected values if all loaded NIF was crystalline. Note that the difference between the loaded and crystalline NIF content corresponds to the content of the amorphous NIF.

For the lowest NIF content of approximately 4 w% no crystalline NIF was present in the samples. This means that the cellulose tablets were able to maintain NIF amorphous. For higher loadings NIF partially recrystallized and part of it remained amorphous. This outcome is quite similar to the results observed for tablets made from smartFilms loaded only with NIF without using PVP as an additional carrier (see Figure 46). Furthermore, the extracted sample thickness from the analysis of the THz data revealed that the thickness of the cellulose tablets increased with the amount of loaded NIF (Figure 49 a)). Since the amount of NIF in the tablets was increased gradually by repeating the loading cycle on the same set of tablets, the resulting increase in tablet thickness is directly related to the loading procedure. The thickness increase is in general not unexpected, since additional material is being loaded into the samples with every loading cycle unless one would expect that the material fills potential air gaps within the sample. On the one hand, the increase in tablet thickness could also mean that an additional layer of NIF was formed on the surface of the tablets. On the other hand, the thickness increase could be a consequence of tablet swelling due to the wetting. To test the latter hypothesis, a set of fresh cellulose tablets was prepared in the same way as schematically depicted in Figure 48. However, instead of applying a NIF solution, 40 µl of pure acetone were used to only wet the tablets. Again, the four cycles were repeated with THz TDS investigation being performed before and after each cycle. The results of thickness investigation as well as NIF crystalline content for these control samples are shown in Figure 50.
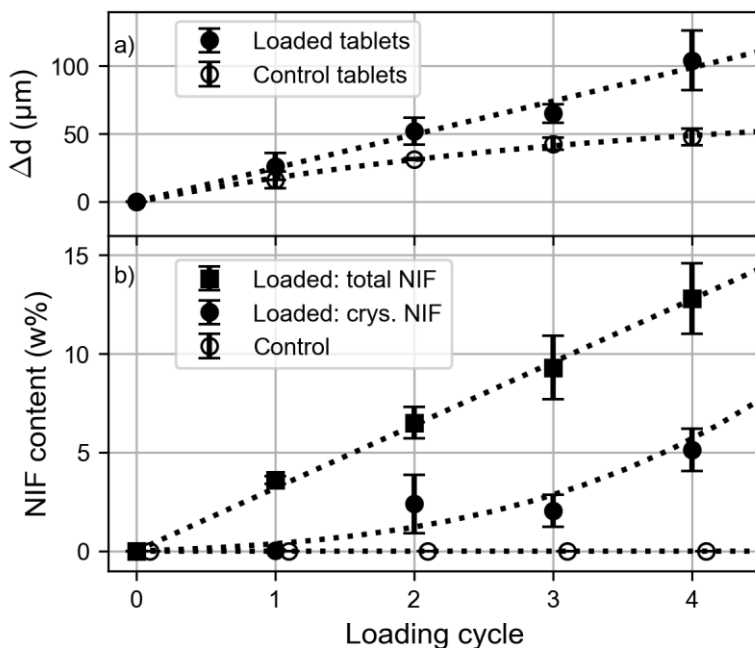
Figure 50. a) Sample thickness difference after each loading cycle. Filled and empty circles correspond to the loaded and control samples, respectively. The dotted curves are a guide-to-the-eye. b) Estimated crystalline NIF content for cellulose tablets loaded with NIF (filled circles) and control samples (empty circles) with respect to the loading cycle. Filled squares correspond to the total content of loaded NIF determined from mass difference before and after the loading. Note that the difference between the total loaded NIF and the crystalline NIF content corresponds to the content of the amorphous NIF. Control samples were only wetted with acetone which means that no NIF was loaded. Value markers for control samples in panel b) are artificially shifted to the right to avoid overlapping.

For the control samples, the evaluation of the crystalline NIF content resulted in 0 w% of crystalline NIF in the samples regardless of the loading cycle. This is expected since only pure acetone was applied onto the control samples, which means that no NIF was present in the samples after the loading. A more interesting outcome can be observed in terms of the thickness difference for the control samples. The analysis of the THz TDS investigation revealed that the thickness of the control samples increased with every loading cycle. However, the increase in thickness is smaller compared to the cellulose tablets loaded with NIF. Furthermore, the trend of the increasing thickness is also different. In the case of control tablets, the trend is non-linear and seems to be reaching a plateau, whereas for the cellulose tablets the thickness seems to be linearly increasing with the number of loading cycles. This difference between the control samples and cellulose tablets loaded with NIF suggests that the thickness increase for the cellulose tablets loaded with NIF is not only due to the swelling of the tablets, but it could also be a consequence of NIF forming an extra layer on the surface of the tablets. To check, whether an extra NIF layer was formed, the tablets were cut using a scalpel and the cross-section was visually investigated using a microscope (Leica M50, Leica Microsystems GmbH, Germany) with an installed digital camera (Moticam X Wi-Fi, MoticEurope, S.L.U., Spain). In Figure 51 photos of one of the tablets and its cross-section as well as microscope images of the cross-section are shown.
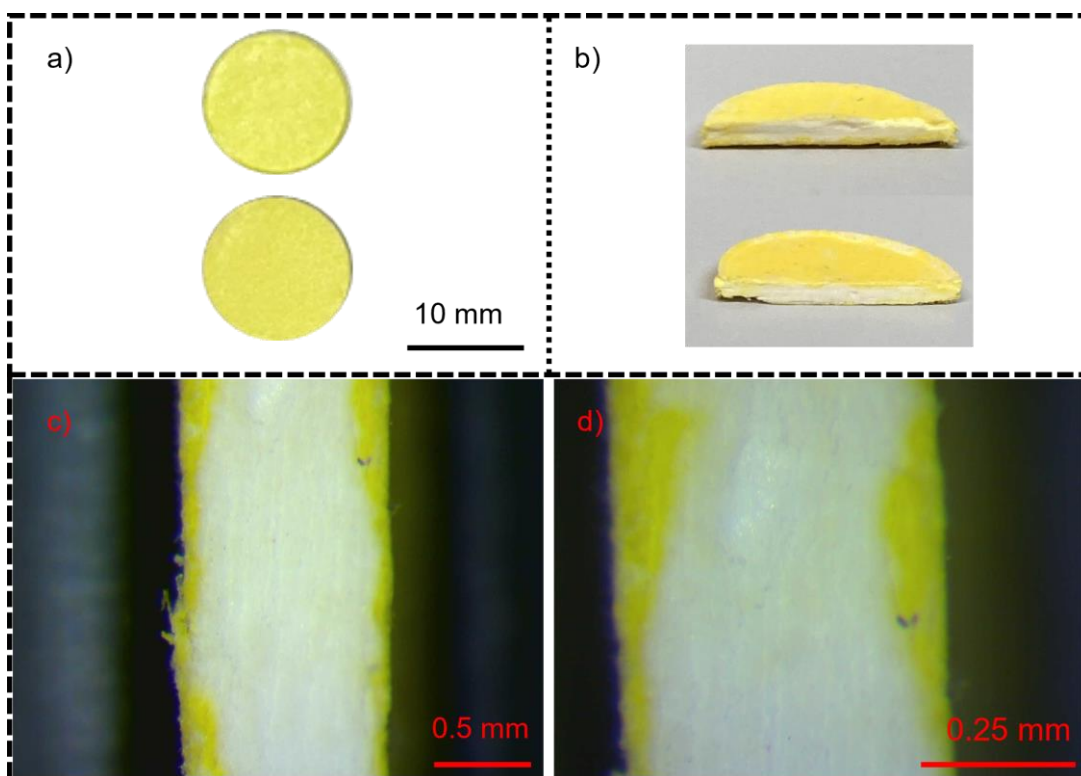
Figure 51. Photos of the a) two flat surfaces of the tablet loaded with NIF and b) its cross-section. c-d) Microscope images of the cross-section. Note that MCC is white and NIF is yellow.

The visual investigation of the cross-section of the samples revealed that the edges of the samples, which correspond to the surface of the tablets, were of yellow color, which is the color of NIF. In the middle part of the tablets the prevailing color was white, which is the color of MCC. However, light yellow regions and lines could be observed in the middle part of the cross-section, indicating that NIF most likely entered the inner parts of the tablets. Nevertheless, a clear difference in colors can be observed between the tablet surface and the inner part of the tablets indicating that NIF mainly stuck to the surface and formed an extra layer. Formation of such layers on the surface and the limited ability to penetrate the interior of the tablets could be a limiting factor for the performance of the cellulose tablets to maintain NIF amorphous. Formation of a drug layer on the surface of smartFilms might also be expected due to the similar loading procedure, which might also limit the capability of smartFilms to maintain the drug amorphous.

In this chapter, the successful application of THz TDS to investigate crystallinity of NIF dispersed in a cellulose matrix was presented. In the next chapter the whole presented work focusing on THz TDS of poorly soluble pharmaceuticals is summarized.

8 Summary and outlook

Most newly developed drugs are poorly soluble, which can lead to poor bioavailability of the drug and, therefore, to a limited success of patient treatment. The solubility of an API can be improved by transforming the API from its stable crystalline state into its amorphous state. However, amorphous APIs are instable and tend to recrystallize, which can lead to unpredictable patient treatment, if the recrystallization takes place during the shelf-life time of the product. Therefore, approaches inhibiting the recrystallization of the amorphous drugs as well as techniques to inspect the solid state of the drug in a formulation, preferably in a non-destructive way, are needed. SmartFilms represent a novel approach, which employs ordinary paper to maintain APIs amorphous with the goal of improving its solubility. The objective of this work is to exploit and explore the potential of THz TDS for the inspection of the solid state of pharmaceuticals loaded into smartFilms and tablets made from them.

To first test the potential of THz TDS to inspect the solid state of pharmaceuticals loaded into smartFilms LTA was chosen as the model drug. LTA is a pharmaceutically non-active ingredient, which is also well soluble in water. However, it is a well-studied chemical in the THz range, which exhibits a strong absorption peak at 1.1 THz when in crystalline state. This makes identification of crystalline LTA straightforward considering that the amorphous materials in this frequency range exhibit featureless absorption. THz TDS investigation of smartFilms and physical mixtures containing LTA revealed that smartFilms can maintain LTA amorphous up to 23 w% of LTA content. The same results were obtained with an XRD analysis of the prepared samples. Furthermore, converting smartFilms into the tablets did not trigger the recrystallization of LTA. These results (see chapter 4) confirm the potential of THz TDS for non-destructive inspection of the solid state of APIs in smartFilms and tablets made from them.

The key aspect of the study involving smartFilms loaded with LTA was the identification of the absorption peak which is indicative of the crystalline state. This approach can be generally extended to APIs which exhibit distinct absorption features in the THz range. Therefore, different poorly soluble drugs were chosen and their absorption properties were investigated in the THz range. They all show absorption features, some more pronounced than others (see section 5.1). Furthermore, a set of excipients, i.e., pharmaceutically non-active ingredients, was also investigated. Some of the selected excipients also show pronounced absorption features in the THz range (see section 5.2). Therefore, the presence of such excipients in the final formulation can make investigation of the solid state of the API more complicated. The absorption peaks identified in the absorption spectra of the selected pharmaceuticals were further characterized by fitting a function consisting of a sum of second order polynomial and a set of Gaussian functions to the individual absorption spectra. The second order polynomial was used to describe the continuous background absorption, whereas the Gaussian functions were used to describe the identified absorption peaks and obtain the properties of the absorption peaks in terms of amplitude, frequency position and width (see section 5.3).

To exploit the potential of THz TDS to inspect the solid state of APIs as well as to assess its crystallinity in tablets made from smartFilms, IM was chosen as a model drug (chapter 6). IM is a BCS class II drug, which has been previously studied in the THz range in its crystalline as well as amorphous state. THz absorption spectra of two polymorphs, the

commonly used γ-IM and metastable α-IM, have been reported. They both show distinct absorption features (see Figure 39), which were further characterized in terms of peak amplitude, frequency position and width (see Table 6). The results of the THz TDS investigation revealed that smartFilms can maintain IM amorphous up to an IM content of approximately 15 w% (see Figure 42). For a higher IM content smartFilms were not able to maintain the entire loaded IM amorphous. Part of the loaded IM recrystallized as α-IM, which is still better soluble than the initially used γ-form. Furthermore, with the increasing amount of loaded IM, the amount of amorphous IM decreased. This indicates that when an additional amount of an API is loaded into smartFilms the initially amorphous API also partially recrystallizes. Finally, the THz TDS investigation of tablets made from smartFilms was repeated one year after the samples had been prepared. The results revealed that IM remained amorphous up to the amount of approximately 15 w%. However, for higher content of the loaded IM, the amount of amorphous IM decreased compared to the freshly prepared samples (see Figure 43). Furthermore, the data suggests that a small amount of γ-IM was present in the samples after one year which indicates that either initially amorphous IM or α-IM partially transformed into the γ-form during storage.

The investigation of tablets made from smartFilms loaded with IM revealed the potential of THz TDS to quantify the crystalline and amorphous fractions of APIs in such formulations. This approach was applied to NIF, which is also a BCS class II drug with pronounced absorption features in the THz range (see section 7.1). In addition to the conventional smartFilms containing NIF, modified smartFilms containing an additional carrier (i.e., PVP) were prepared and their ability to maintain NIF amorphous was compared (see section 7.2). A THz TDS investigation of the two sample types revealed that PVP improves the capability of smartFilms to maintain NIF amorphous (see Figure 46). An investigation of the samples three and six months after preparing them revealed that the addition of PVP also improves the capability of smartFilms to maintain NIF amorphous during storage (see Figure 47). THz TDS was also employed to investigate the solid state of NIF after directly loading it into tablets made from MCC (see section 7.3). The results revealed a similar capability of cellulose tablets to maintain NIF amorphous as the conventional smartFilms. Furthermore, the evaluation of the thickness of the cellulose tablets before and after each loading cycle revealed a gradual increase in sample thickness after each loading cycle. By preparing and investigating additional control samples (see Figure 50) as well as by cutting the tablets loaded with NIF and inspecting their cross-section under a microscope (see Figure 51), the increasing thickness could be attributed to the swelling of the tablets as well as to the formation of an additional NIF layer on the surface of the tablets. Formation of such a surface layer and the limited ability of NIF to penetrate the interior of the tablets could potentially limit the capability of such formulations to maintain NIF amorphous.

The results presented in this work demonstrate the ability of THz TDS for the investigation of the solid state of APIs in smartFilms and tablets made from them. Based on these results THz TDS can be applied to studies of different types of pharmaceutical solid dosage forms in the future. For example, solid dispersions employing different carrier materials or being prepared with different techniques could be inspected using THz TDS. Their ability to maintain APIs amorphous could then be directly compared. Different paper types for preparation of smartFilms as well as additional processing steps

such as paper granulation, which would be needed in a large-scale production process, should be also considered in the future. Furthermore, stability of amorphous APIs in different formulations could be investigated by continuously monitoring a set of samples during accelerated aging at elevated temperatures. Also, inspection of more complex and realistic formulations consisting of an API and several excipients including tablet coating should be considered in the future. In addition to the inspection of the solid state of the API in tablets, the simultaneous assessment of tablet porosity based on the performed THz TDS transmission measurements can be considered. Porosity plays an important role in the disintegration of tablets as well as the drug release. Furthermore, the dissolution and solubility advantage of formulations containing amorphous APIs should be studied and compared to the formulations with crystalline drugs. Finally, the approach presented here for the investigation of the solid state of the APIs relies on the identification and quantification of pronounced absorption features which are related to the crystallinity of the API. So far only information about the absorption coefficient of the samples has been exploited for this task. Since THz TDS investigation of samples allows simultaneous extraction of absorption coefficient and refractive index, refractive index values could be considered in the evaluation. Furthermore, the approach presented in this work is limited to APIs with pronounced absorption features in the detectable THz range. To potentially overcome this problem, combining such APIs with other active or inactive pharmaceuticals, which show pronounced absorption features, could be considered. By forming co-amorphous complexes and potentially even combining them with the concept of smartFilms, improved solubility could be achieved. Furthermore, the additional pharmaceutical with pronounced absorption features in the THz range could be used as an indicator for potential recrystallization of the co-amorphous complex.

9 Zusammenfassung und Ausblick

Die meisten neu entwickelten Arzneimittel sind nur schwer löslich, was zu einer schlechten Bioverfügbarkeit des Arzneimittels und damit zu einem begrenzten Erfolg der Patientenbehandlung führen kann. Die Löslichkeit eines Wirkstoffs kann verbessert werden, indem der Wirkstoff von seinem stabilen kristallinen Zustand in seinen amorphen Zustand überführt wird. Amorphe Wirkstoffe sind jedoch instabil und neigen zur Rekristallisation, was zu einer unvorhersehbaren Patientenbehandlung führen kann, wenn die Rekristallisation während der Haltbarkeitsdauer des Produkts stattfindet. Daher werden Ansätze benötigt, die die Rekristallisation amorpher Arzneimittel verhindern, sowie Techniken zur Überprüfung der molekularen Ordnung des Arzneimittels (engl.: solid state of the drug) in einer Formulierung, vorzugsweise auf zerstörungsfreie Weise. SmartFilms sind ein neuartiger Ansatz, bei dem gewöhnliches Papier verwendet wird, um Wirkstoffe amorph zu halten, mit dem Ziel, ihre Löslichkeit zu verbessern. Ziel dieser Arbeit ist die Nutzung und Erforschung des Potenzials von Terahertz-(THz)-Zeitbereichsspektroskopie (TDS) für die Prüfung der molekularen Ordnung von Arzneimitteln, die in smartFilms und daraus hergestellten Tabletten enthalten sind.

Um zunächst das Potenzial von THz-TDS für die Untersuchung der molekularen Ordnung von in smartFilms geladenen Arzneimitteln zu testen, wurde LTA als Modellarzneimittel ausgewählt. Dieses ist kein Wirkstoff und löst sich leicht in Wasser auf. Es handelt sich jedoch um eine gut untersuchte Chemikalie im THz-Bereich, die im kristallinen Zustand einen starken Absorptionspeak bei 1,1 THz aufweist, was die Identifizierung von kristallinem LTA vereinfacht, da amorphe Materialien in diesem Frequenzbereich eine unauffällige Absorption aufweisen. Die THz-TDS-Untersuchung von smartFilms und physikalischen Mischungen, die LTA enthalten, ergab, dass smartFilms LTA bis zu einem LTA-Gehalt von 23 Gew.-% amorph halten können. Die gleichen Ergebnisse wurden mit einer XRD-Analyse der hergestellten Proben erzielt. Darüber hinaus führte die Umwandlung von smartFilms in Tabletten nicht zur Rekristallisation von LTA. Diese Ergebnisse (siehe Kapitel 4) bestätigen das Potenzial der THz-TDS für die zerstörungsfreie Prüfung der molekularen Ordnung von Wirkstoffen in smartFilms und daraus hergestellten Tabletten.

Der Schlüsselaspekt der Studie über mit LTA beladenen smartFilms war die Identifizierung des Absorptionspeaks, der auf den kristallinen Zustand hinweist. Dieser Ansatz kann allgemein auf Wirkstoffe ausgedehnt werden, die deutliche Absorptionsmerkmale im THz-Bereich aufweisen. Daher wurden verschiedene schwerlösliche Arzneimittel ausgewählt und ihre Absorptionseigenschaften im THz-Bereich untersucht. Sie alle zeigen Absorptionsmerkmale, einige davon ausgeprägter als andere (siehe Abschnitt 5.1). Darüber hinaus wurde auch eine Reihe von Hilfsstoffen untersucht. Einige der ausgewählten Hilfsstoffe zeigen ebenfalls ausgeprägte Absorptionsmerkmale im THz-Bereich (siehe Abschnitt 5.2). Daher kann das Vorhandensein solcher Hilfsstoffe in der endgültigen Formulierung die Untersuchung der molekularen Ordnung des Wirkstoffs erschweren. Die in den Absorptionsspektren der ausgewählten Arzneimittel identifizierten Absorptionspeaks wurden weiter charakterisiert, indem eine Funktion, bestehend aus einer Summe von einem Polynom zweiter Ordnung und eines Satzes von Gauß-Funktionen, an die einzelnen Absorptionsspektren angepasst wurde. Das Polynom zweiter Ordnung diente zur

Beschreibung der kontinuierlichen Hintergrundabsorption, während die Gauß-Funktionen zur Beschreibung der identifizierten Absorptionspeaks verwendet wurden. Anhand der Anpassung wurden die Eigenschaften der Absorptionspeaks in Bezug auf Amplitude, Frequenzposition und -breite bestimmt (siehe Abschnitt 5.3).

Um das Potenzial der THz-TDS zur Untersuchung der molekularen Ordnung von Wirkstoffen sowie zur Bewertung ihrer Kristallinität in aus smartFilms hergestellten Tabletten zu nutzen, wurde IM als Modellarzneimittel ausgewählt (Kapitel 6). IM ist ein Arzneimittel der BCS-Klasse II, das zuvor im THz-Bereich sowohl im kristallinen als auch im amorphen Zustand untersucht wurde. Es wurden THz-Absorptionsspektren von zwei Polymorphen, dem allgemein verwendeten γ-IM und dem metastabilen α-IM, berichtet. Beide zeigen deutliche Absorptionsmerkmale (siehe Abbildung 39), die in Bezug auf Peakamplitude, Frequenzposition und -breite weiter charakterisiert wurden (siehe Tabelle 6). Die Ergebnisse der THz-TDS-Untersuchung zeigten, dass smartFilms IM bis zu einem IM-Gehalt von etwa 15 Gew.-% amorph halten können (siehe Abbildung 42). Bei einem höheren IM-Gehalt waren die smartFilms nicht in der Lage, das gesamte beladene IM amorph zu halten. Ein Teil des geladenen IMs rekristallisierte als α-IM, das immer noch besser löslich ist als die ursprünglich verwendete γ-Form. Darüber hinaus nahm mit zunehmender Menge an geladenem IM die Menge an amorphem IM ab. Dies deutet darauf hin, dass der ursprünglich amorphe Wirkstoff auch teilweise rekristallisiert, wenn die smartFilms mit einer höheren Menge Wirkstoff beladen werden. Schließlich wurde die THz-TDS-Untersuchung der aus smartFilms hergestellten Tabletten ein Jahr nach der Herstellung der Proben wiederholt. Die Ergebnisse zeigten, dass IM bis zu einem Anteil von etwa 15 Gew.-% amorph blieb. Bei höheren Gehalten an geladenem IM nahm die Menge an amorphem IM im Vergleich zu den frisch hergestellten Proben jedoch ab (siehe Abbildung 43). Darüber hinaus deuten die Daten darauf hin, dass in den Proben nach einem Jahr eine geringe Menge an γ-IM vorhanden war, was darauf hindeutet, dass sich entweder das ursprünglich amorphe IM oder das α-IM während der Lagerung teilweise in die γ-Form umgewandelt hat.

Die Untersuchung von Tabletten, die aus mit IM beladenen smartFilms hergestellt wurden, zeigte das Potenzial der THz-TDS für die zerstörungsfreie Inspektion und Quantifizierung der Kristallinität und Amorphie von Wirkstoffen in solchen Formulierungen. Dieser Ansatz wurde auf NIF angewandt, das ebenfalls ein Arzneimittel der BCS-Klasse II mit ausgeprägten Absorptionsmerkmalen im THz-Bereich ist (siehe Abschnitt 7.1). Zusätzlich zu den konventionellen smartFilms, die NIF enthalten, wurden modifizierte smartFilms mit PVP als einem zusätzlichen Träger hergestellt und ihre Fähigkeit, NIF amorph zu halten, verglichen (siehe Abschnitt 7.2). Die THz-TDS-Untersuchung der beiden Probentypen ergab, dass PVP die Fähigkeit der smartFilms verbessert, NIF amorph zu halten (siehe Abbildung 46). Die Untersuchung der Proben drei und sechs Monate nach ihrer Herstellung ergab, dass der Zusatz von PVP auch die Fähigkeit der smartFilms verbessert, die NIF während der Lagerung amorph zu halten (siehe Abbildung 47). THz-TDS wurde auch eingesetzt, um die molekulare Ordnung von NIF zu untersuchen, nachdem es direkt in Tabletten aus MCC geladen wurde (siehe Abschnitt 7.3). Die Ergebnisse zeigten, dass die Zellulosetabletten ähnlich gut in der Lage sind, NIF amorph zu halten wie die herkömmlichen smartFilms. Darüber hinaus ergab die Auswertung der Dicke der Zellulosetabletten vor und nach jedem Ladezyklus eine allmähliche Zunahme der Probendicke nach jedem Ladezyklus. Durch die

Herstellung und Untersuchung zusätzlicher Kontrollproben (siehe Abbildung 50) sowie durch das Aufschneiden der mit NIF beladenen Tabletten und die Untersuchung ihres Querschnitts unter dem Mikroskop (siehe Abbildung 51) konnte die zunehmende Dicke auf die Quellung der Tabletten sowie die Bildung einer zusätzlichen NIF-Schicht auf der Oberfläche der Tabletten zurückgeführt werden. Die Bildung einer solchen Oberflächenschicht und die begrenzte Fähigkeit von NIF, in das Innere der Tabletten einzudringen, könnten die Fähigkeit solcher Formulierungen, NIF amorph zu halten, möglicherweise einschränken.

Die in dieser Arbeit vorgestellten Ergebnisse bestätigen das Potenzial der THz-TDS für die Untersuchung der molekularen Ordnung von Wirkstoffen in smartFilms und daraus hergestellter Tabletten. Auf der Grundlage dieser Ergebnisse kann THz-TDS in Zukunft für Untersuchungen verschiedener Arten von festen pharmazeutischen Darreichungsformen eingesetzt werden. Zum Beispiel könnten feste Dispersionen (engl.: solid dispersions), die verschiedene Trägermaterialien verwenden oder mit verschiedenen Techniken hergestellt werden, mit THz-TDS untersucht werden, und ihre Fähigkeit, Wirkstoffe amorph zu halten, könnte direkt verglichen werden. Verschiedene Papiersorten für die Herstellung von smartFilms sowie zusätzliche Verarbeitungsschritte wie die Papiergranulierung, die in einem Produktionsprozess im großen Maßstab erforderlich wären, sollten in Zukunft ebenfalls in Betracht gezogen werden. Außerdem könnte die Stabilität solcher Formulierungen durch kontinuierliche Überwachung einer Reihe von Proben während der beschleunigten Alterung bei erhöhten Temperaturen untersucht werden. Auch die Prüfung komplexerer und realistischerer Formulierungen, die aus einem Wirkstoff und mehreren Hilfsstoffen einschließlich Tablettenüberzug bestehen, sollte in Betracht gezogen werden. Zusätzlich zur Prüfung der molekularen Ordnung des Wirkstoffs in Tabletten kann eine gleichzeitige Bewertung der Tablettenporosität auf der Grundlage der durchgeführten THz-TDS-Transmissionsmessungen in Betracht gezogen werden. Die Porosität spielt eine wichtige Rolle beim Zerfall der Tabletten sowie bei der Freisetzung des Wirkstoffs. Darüber hinaus sollten die Auflösungs- und Löslichkeitsvorteile von Formulierungen mit amorphen Wirkstoffen untersucht und mit denen von Formulierungen mit kristallinen Wirkstoffen verglichen werden. Schließlich beruht der hier vorgestellte Ansatz zur Untersuchung der molekularen Ordnung der Wirkstoffe auf der Identifizierung und Quantifizierung ausgeprägter Absorptionsmerkmale, die mit der Kristallinität des Wirkstoffs in Zusammenhang stehen. Bislang wurden für diese Aufgabe nur Informationen über den Absorptionskoeffizienten der Proben genutzt. Da die THz-TDS-Untersuchung von Proben die gleichzeitige Extraktion des Absorptionskoeffizienten und des Brechungsindexes ermöglicht, könnten die Werte des Brechungsindexes bei der Auswertung berücksichtigt werden. Außerdem ist der in dieser Arbeit vorgestellte Ansatz auf Wirkstoffe beschränkt, die ausgeprägte Absorptionsmerkmale im unteren THz-Bereich aufweisen. Um dieses Problem möglicherweise zu überwinden, könnten Wirkstoffe, denen ausgeprägte Absorptionslinien fehlen, mit anderen aktiven oder inaktiven Arzneimitteln, die ausgeprägte Absorptionsmerkmale aufweisen, in Betracht gezogen werden. Durch die Bildung koamorpher Komplexe und möglicherweise sogar durch die Kombination mit dem Konzept der smartFilms könnte eine verbesserte Löslichkeit erreicht werden. Darüber hinaus könnte das zusätzliche Arzneimittel mit ausgeprägten Absorptionsmerkmalen im THz-Bereich als Indikator für eine mögliche Rekristallisation des gesamten koamorphen Komplexes verwendet werden.

Bibliography

1. H. J. Heppner, C. C. Sieber, A. S. Esslinger, and J. Trögner, "Arzneimittelformen und arzneimittelverabreichung in der geriatrie," Ther. Umschau **63**(6), 419–422 (2006).

2. N. Drumond and S. Stegemann, "Better Medicines for Older Patients: Considerations between Patient Characteristics and Solid Oral Dosage Form Designs to Improve Swallowing Experience," Pharmaceutics **13**(1), 32 (2020).

3. H. Zhong, G. Chan, Y. Hu, H. Hu, and D. Ouyang, "A comprehensive map of FDA-approved pharmaceutical products," Pharmaceutics **10**(4), 1–19 (2018).

4. G. L. Amidon, H. Lennernäs, V. P. Shah, and J. R. Crison, "A Theoretical Basis for a Biopharmaceutic Drug Classification: The Correlation of in Vitro Drug Product Dissolution and in Vivo Bioavailability," Pharm. Res. An Off. J. Am. Assoc. Pharm. Sci. **12**(3), 413–420 (1995).

5. I. Nikolakakis and I. Partheniadis, "Self-Emulsifying Granules and Pellets: Composition and Formation Mechanisms for Instant or Controlled Release," Pharmaceutics **9**(4), 50 (2017).

6. S. Stegemann, F. Leveiller, D. Franchi, H. de Jong, and H. Lindén, "When poor solubility becomes an issue: From early stage to proof of concept," Eur. J. Pharm. Sci. **31**(5), 249–261 (2007).

7. B. C. Hancock and M. Parks, "What is the true solubility advantage for amorphous pharmaceuticals?," Pharm. Res. **17**(4), 397–404 (2000).

8. C. M. Lemke, Stefan; Strätling, Ernst-Josef; Welzel, Hans-Peter; Keck, "Cellulosefaserbasierte Trägermatrices (smartFilms) zur Applikation von Inhaltsstoffen sowie deren Herstellung," U.S. patent DE102016000541A1 (2017).

9. C. M. Lemke, Stefan; Strätling, Ernst-Josef; Welzel, Hans-Peter; Keck, "Cellulose fibre based support matrices for layered products for oral and peroral application and their preparation," U.S. patent EP3192499A1 (2017).

10. D. M. Mittleman, "Perspective: Terahertz science and technology," J. Appl. Phys. **122**(23), (2017).

11. P. F. Taday, D. Van Der Weide, K. Wood, M. Chamberlain, H. Roskos, C. Phillips, D. Newnham, M. Towrie, and I. Appelquist, "Applications of terahertz spectroscopy to pharmaceutical sciences," Philos. Trans. R. Soc. A Math. Phys. Eng. Sci. **362**(1815), 351–364 (2004).

12. M. Walther, B. M. Fischer, and P. U. Jepsen, "Noncovalent intermolecular forces in polycrystalline and amorphous saccharides in the far infrared," Chem. Phys. **288**(2–3), 261–268 (2003).

13. D. Markl, M. T. Ruggiero, and J. A. Zeitler, "Pharmaceutical applications of terahertz spectroscopy and imaging," Eur. Pharm. Rev. **21**(4), 45–50 (2016).

14. T. Kleine-Ostmann, R. Wilk, F. Rutz, M. Koch, H. Niemann, B. Güttler, K. Brandhorst, and J. Grunenberg, "Probing noncovalent interactions in biomolecular crystals with terahertz spectroscopy," ChemPhysChem **9**(4), 544–547 (2008).

15. B. Fischer, M. Hoffmann, H. Helm, G. Modjesch, and P. U. Jepsen, "Chemical recognition in terahertz time-domain spectroscopy and imaging," Semicond. Sci.

Technol. **20**(7), 246–253 (2005).

16. C. J. Strachan, T. Rades, D. A. Newnham, K. C. Gordon, M. Pepper, and P. F. Taday, "Using terahertz pulsed spectroscopy to study crystallinity of pharmaceutical materials," Chem. Phys. Lett. **390**(1–3), 20–24 (2004).

17. P. F. Taday, I. V. Bradley, D. D. Arnone, and M. Pepper, "Using Terahertz pulse spectroscopy to study the crystalline structure of a drug: A case study of the polymorphs of ranitidine hydrochloride," J. Pharm. Sci. **92**(4), 831–838 (2003).

18. V. P. Wallace, P. F. Taday, A. J. Fitzgerald, R. M. Woodward, J. Cluff, R. J. Pye, and D. D. Arnone, "Terahertz pulsed imaging and spectroscopy for biomedical and pharmaceutical applications," Faraday Discuss. **126**(1), 255–263 (2004).

19. J. A. Zeitler, D. A. Newnham, P. F. Taday, T. L. Threlfall, R. W. Lancaster, R. W. Berg, C. J. Strachan, M. Pepper, K. C. Gordon, and T. Rades, "Characterization of Temperature-Induced Phase Transitions in Five Polymorphic Forms of Sulfathiazole by Terahertz Pulsed Spectroscopy and Differential Scanning Calorimetry," J. Pharm. Sci. **95**(11), 2486–2498 (2006).

20. S. N. Taraskin, S. I. Simdyankin, S. R. Elliott, J. R. Neilson, and T. Lo, "Universal features of terahertz absorption in disordered materials," Phys. Rev. Lett. **97**(5), 1–4 (2006).

21. T. Idehara, T. Saito, I. Ogawa, S. Mitsudo, Y. Tatematsu, and S. Sabchevski, "The potential of the gyrotrons for development of the sub-terahertz and the terahertz frequency range - A review of novel and prospective applications," Thin Solid Films **517**(4), 1503–1506 (2008).

22. P. R. Smith, D. H. Auston, and M. C. Nuss, "Subpicosecond photoconducting dipole antennas," IEEE J. Quantum Electron. **24**(2), 255–260 (1988).

23. M. van Exter, C. Fattinger, and D. Grischkowsky, "Terahertz time-domain spectroscopy of water vapor," Opt. Lett. **14**(20), 1128 (1989).

24. R. A. Lewis, "A review of terahertz sources," J. Phys. D. Appl. Phys. **47**(37), (2014).

25. B. A. Knyazev, G. N. Kulipanov, and N. A. Vinokurov, "Novosibirsk terahertz free electron laser: instrumentation development and experimental achievements," Meas. Sci. Technol. **21**(5), (2010).

26. T. Idehara and S. P. Sabchevski, "Gyrotrons for High-Power Terahertz Science and Technology at FIR UF," J. Infrared, Millimeter, Terahertz Waves **38**(1), 62–86 (2017).

27. I. Mehdi, J. V. Siles, C. Lee, and E. Schlecht, "THz diode technology: Status, prospects, and applications," Proc. IEEE **105**(6), 990–1007 (2017).

28. G. Dodel, "On the history of far-infrared (FIR) gas lasers: Thirty-five years of research and application," Infrared Phys. Technol. **40**(3), 127–139 (1999).

29. P. U. Jepsen, D. G. Cooke, and M. Koch, "Terahertz spectroscopy and imaging - Modern techniques and applications," Laser Photonics Rev. **5**(1), 124–166 (2011).

30. N. Vieweg, F. Rettich, A. Deninger, H. Roehle, R. Dietz, T. Göbel, and M. Schell, "Terahertz-time domain spectrometer with 90 dB peak dynamic range," J.

Infrared, Millimeter, Terahertz Waves **35**(10), 823–832 (2014).

31. P. Y. Han and X. C. Zhang, "Coherent, broadband midinfrared terahertz beam sensors," Appl. Phys. Lett. **73**(21), 3049–3051 (1998).

32. R. Huber, A. Brodschelm, F. Tauser, and A. Leitenstorfer, "Generation and field-resolved detection of femtosecond electromagnetic pulses tunable up to 41 THz," Appl. Phys. Lett. **76**(22), 3191–3193 (2000).

33. E. R. Brown, K. A. McIntosh, F. W. Smith, M. J. Manfra, and C. L. Dennis, "Measurements of optical-heterodyne conversion in low-temperature-grown GaAs," Appl. Phys. Lett. **62**(11), 1206–1208 (1993).

34. R. Wilk, F. Breitfeld, M. Mikulics, and M. Koch, "Continuous wave terahertz spectrometer as a noncontact thickness measuring device," Appl. Opt. **47**(16), 3023 (2008).

35. M. Naftaly, N. Vieweg, and A. Deninger, "Industrial applications of terahertz sensing: State of play," Sensors **19**(19), (2019).

36. B. Globisch, R. J. B. Dietz, T. Göbel, M. Schell, W. Bohmeyer, R. Müller, and A. Steiger, "Absolute terahertz power measurement of a time-domain spectroscopy system," Opt. Lett. **40**(15), 3544 (2015).

37. N. M. Burford and M. O. El-Shenawee, "Review of terahertz photoconductive antenna technology," Opt. Eng. **56**(1), (2017).

38. C. Fattinger and D. Grischkowsky, "Terahertz beams," Appl. Phys. Lett. **54**(6), 490–492 (1989).

39. Y. Cai, I. Brener, J. Lopata, J. Wynn, L. Pfeiffer, and J. Federici, "Design and performance of singular electric field terahertz photoconducting antennas," Appl. Phys. Lett. **71**(15), 2076–2078 (1997).

40. M. Bieler, G. Hein, K. Pierz, U. Siegner, and M. Koch, "Spatial pattern formation of optically excited carriers in photoconductive switches," Appl. Phys. Lett. **77**(7), 1002–1004 (2000).

41. E. Castro-Camus, J. Lloyd-Hughes, and M. B. Johnston, "Three-dimensional carrier-dynamics simulation of terahertz emission from photoconductive switches," Phys. Rev. B - Condens. Matter Mater. Phys. **71**(19), 1–7 (2005).

42. E. Castro-Camus and M. Alfaro, "Photoconductive devices for terahertz pulsed spectroscopy: a review [Invited]," Photonics Res. **4**(3), A36 (2016).

43. M. van Exter and D. R. Grischkowsky, "Characterization of an optoelectronic terahertz beam system," IEEE Trans. Microw. Theory Tech. **38**(11), 1684–1691 (1990).

44. A. Abdul-Munaim, J. Ornik, M. Koch, and D. Watson, "Terahertz Time Domain Spectroscopy to Detect Different Oxidation Levels of Diesel Engine Oil," Lubricants **7**(2), 18 (2019).

45. J. Ornik, J. Lehr, M. Reuter, D. Jahn, F. Beltran-Mejia, J. Balzer, T. Kleine-Ostmann, and M. Koch, "Repeatability of material parameter extraction of liquids from transmission terahertz time-domain measurements," Opt. Express **28**(19), 28178–28189 (2020).

46. G. Klatt, R. Gebs, H. Schäfer, M. Nagel, C. Janke, A. Bartels, and T. Dekorsy, "High-Resolution Terahertz Spectrometer," IEEE J. Sel. Top. Quantum Electron. **17**(1), 159–168 (2011).

47. R. J. B. Dietz, N. Vieweg, T. Puppe, A. Zach, B. Globisch, T. Göbel, P. Leisching, and M. Schell, "All fiber-coupled THz-TDS system with kHz measurement rate based on electronically controlled optical sampling," Opt. Lett. **39**(22), 6482 (2014).

48. R. J. B. Dietz, B. Globisch, M. Gerhard, A. Velauthapillai, D. Stanze, H. Roehle, M. Koch, T. Göbel, and M. Schell, "64 µ W pulsed terahertz emission from growth optimized InGaAs/InAlAs heterostructures with separated photoconductive and trapping regions," Appl. Phys. Lett. **103**(6), 061103 (2013).

49. R. B. Kohlhaas, S. Breuer, S. Nellen, L. Liebermeister, M. Schell, M. P. Semtsiv, W. T. Masselink, and B. Globisch, "Photoconductive terahertz detectors with 105 dB peak dynamic range made of rhodium doped InGaAs," Appl. Phys. Lett. **114**(22), 221103 (2019).

50. S. P. Mickan, J. Xu, J. Munch, X.-C. Zhang, and D. Abbott, "The limit of spectral resolution in THz time-domain spectroscopy," Photonics Des. Technol. Packag. **5277**, 54 (2004).

51. W. Withayachumnankul and M. Naftaly, "Fundamentals of measurement in terahertz time-domain spectroscopy," J. Infrared, Millimeter, Terahertz Waves **35**(8), 610–637 (2014).

52. F. J. Harris, "On the use of windows for harmonic analysis with the discrete Fourier transform," Proc. IEEE **66**(1), 51–83 (1978).

53. J. Vázquez-Cabo, P. Chamorro-Posada, F. J. Fraile-Peláez, Ó. Rubiños-López, J. M. López-Santos, and P. Martín-Ramos, "Windowing of THz time-domain spectroscopy signals: A study based on lactose," Opt. Commun. **366**, 386–396 (2016).

54. M. Naftaly and R. Dudley, "Methodologies for determining the dynamic ranges and signal-to-noise ratios of terahertz time-domain spectrometers," Opt. Lett. **34**(8), 1213 (2009).

55. I. Pupeza, R. Wilk, and M. Koch, "Highly accurate optical material parameter determination with THz time-domain spectroscopy," Opt. Express **15**(7), 4335 (2007).

56. P. U. Jepsen and B. M. Fischer, "Dynamic range in terahertz time-domain transmission and reflection spectroscopy," Opt. Lett. **30**(1), 29 (2005).

57. C. Rønne, L. Thrane, P. O. Åstrand, A. Wallqvist, K. V. Mikkelsen, and S. R. Keiding, "Investigation of the temperature dependence of dielectric relaxation in liquid water by THz reflection spectroscopy and molecular dynamics simulation," J. Chem. Phys. **107**(14), 5319–5331 (1997).

58. W. Withayachumnankul, B. M. Fischer, and D. Abbott, "Numerical removal of water vapour effects from terahertz time-domain spectroscopy measurements," Proc. R. Soc. A Math. Phys. Eng. Sci. **464**(2097), 2435–2456 (2008).

59. M. Mikerov, J. Ornik, and M. Koch, "Removing Water Vapor Lines From THz-TDS Data Using Neural Networks," IEEE Trans. Terahertz Sci. Technol. **10**(4), 397–403 (2020).

60. D. Grischkowsky, S. Keiding, M. van Exter, and C. Fattinger, "Far-infrared time-domain spectroscopy with terahertz beams of dielectrics and semiconductors," J. Opt. Soc. Am. B **7**(10), 2006 (1990).

61. B. E. A. Saleh and M. C. Teich, *Fundamentals of Photonics* (Wiley, 2007).

62. P. U. Jepsen, "Phase Retrieval in Terahertz Time-Domain Measurements: a "how to" Tutorial," J. Infrared, Millimeter, Terahertz Waves (January), 395–411 (2019).

63. W. Withayachumnankul, H. Lin, S. P. Mickan, B. M. Fischer, and D. Abbott, "Analysis of measurement uncertainty in THz-TDS," **6593**, 659326 (2007).

64. W. Withayachumnankul, B. M. Fischer, H. Lin, and D. Abbott, "Uncertainty in terahertz time-domain spectroscopy measurement," J. Opt. Soc. Am. B **25**(6), 1059 (2008).

65. L. Duvillaret, F. Garet, and J. L. Coutaz, "A reliable method for extraction of material parameters in terahertz time-domain spectroscopy," IEEE J. Sel. Top. Quantum Electron. **2**(3), 739–745 (1996).

66. L. Duvillaret, F. Garet, and J.-L. Coutaz, "Highly precise determination of optical constants and sample thickness in terahertz time-domain spectroscopy," Appl. Opt. **38**(2), 409 (1999).

67. R. Wilk, I. Pupeza, R. Cernat, and M. Koch, "Highly accurate THz time-domain spectroscopy of multilayer structures," IEEE J. Sel. Top. Quantum Electron. **14**(2), 392–398 (2008).

68. M. Scheller, C. Jansen, and M. Koch, "Analyzing sub-100-µm samples with transmission terahertz time domain spectroscopy," Opt. Commun. **282**(7), 1304–1306 (2009).

69. P. Kužel, H. Němec, F. Kadlec, and C. Kadlec, "Gouy shift correction for highly accurate refractive index retrieval in time-domain terahertz spectroscopy," Opt. Express **18**(15), 15338 (2010).

70. J. Dai, J. Zhang, W. Zhang, and D. Grischkowsky, "Terahertz time-domain spectroscopy characterization of the far-infrared absorption and index of refraction of high-resistivity, float-zone silicon," J. Opt. Soc. Am. B **21**(7), 1379 (2004).

71. B. Globisch, R. J. B. Dietz, R. B. Kohlhaas, S. Nellen, M. Kleinert, T. Göbel, and M. Schell, "Fiber-coupled transceiver for terahertz reflection measurements with a 4.5 THz bandwidth," Opt. Lett. **41**(22), 5262 (2016).

72. U. Møller, D. G. Cooke, K. Tanaka, and P. U. Jepsen, "Terahertz reflection spectroscopy of Debye relaxation in polar liquids [Invited]," J. Opt. Soc. Am. B **26**(9), A113 (2009).

73. P. U. Jepsen, U. Møller, and H. Merbold, "Investigation of aqueous alcohol and sugar solutions with reflection terahertz time-domain spectroscopy," Opt. Express **15**(22), 14717 (2007).

74. T. Probst, S. Sommer, A. Soltani, E. Kraus, B. Baudrit, G. E. Town, and M. Koch, "Monitoring the Polymerization of Two-Component Epoxy Adhesives Using a Terahertz Time Domain Reflection System," J. Infrared, Millimeter, Terahertz Waves **36**(6), 569–577 (2015).

75. E.-M. Stubling, N.-A. Staats, B. Globisch, M. Schell, H. D. Portsteffen, and M.

Koch, "Investigating the Layer Structure and Insect Tunneling on a Wooden Putto Using Robotic-Based THz Tomography," IEEE Trans. Terahertz Sci. Technol. **10**(4), 343–347 (2020).

76. H. Hirori, K. Yamashita, M. Nagai, and K. Tanaka, "Attenuated total reflection spectroscopy in time domain using terahertz coherent pulses," Japanese J. Appl. Physics, Part 2 Lett. **43**(10 A), 43–46 (2004).

77. D. A. Newnham and P. F. Taday, "Pulsed Terahertz attenuated total reflection spectroscopy," Appl. Spectrosc. **62**(4), 394–398 (2008).

78. A. Soltani, D. Jahn, L. Duschek, E. Castro-Camus, M. Koch, and W. Withayachumnankul, "Attenuated Total Reflection Terahertz Time-Domain Spectroscopy: Uncertainty Analysis and Reduction Scheme," IEEE Trans. Terahertz Sci. Technol. **6**(1), 32–39 (2016).

79. N. Palka, M. Szala, and E. Czerwinska, "Characterization of prospective explosive materials using terahertz time-domain spectroscopy," Appl. Opt. **55**(17), 4575 (2016).

80. M. Nagai, H. Yada, T. Arikawa, and K. Tanaka, "Terahertz time-domain attenuated total reflection spectroscopy in water and biological solution," Int. J. Infrared Millimeter Waves **27**(4), 505–515 (2006).

81. A. Nakanishi, Y. Kawada, T. Yasuda, K. Akiyama, and H. Takahashi, "Terahertz time domain attenuated total reflection spectroscopy with an integrated prism system," Rev. Sci. Instrum. **83**(3), (2012).

82. I. A. Azarov, Y. Y. Choporova, V. A. Shvets, and B. A. Knyazev, "An Ellipsometric Technique with an ATR Module and a Monochromatic Source of Radiation for Measurement of Optical Constants of Liquids in the Terahertz Range," J. Infrared, Millimeter, Terahertz Waves **40**(2), 200–209 (2019).

83. T. I. Jeon and D. Grischkowsky, "Characterization of optically dense, doped semiconductors by reflection THz time domain spectroscopy," Appl. Phys. Lett. **72**(23), 3032–3034 (1998).

84. L. Thrane, R. H. Jacobsen, P. Uhd Jepsen, and S. R. Keiding, "THz reflection spectroscopy of liquid water," Chem. Phys. Lett. **240**(4), 330–333 (1995).

85. D. M. Mittleman, S. Hunsche, L. Boivin, and M. C. Nuss, "T-ray tomography," Opt. Lett. **22**(12), 904 (1997).

86. J. Dong, X. Wu, A. Locquet, and D. S. Citrin, "Terahertz Superresolution Stratigraphic Characterization of Multilayered Structures Using Sparse Deconvolution," IEEE Trans. Terahertz Sci. Technol. **7**(3), 260–267 (2017).

87. K. Krügener, J. Ornik, L. M. Schneider, A. Jäckel, C. L. Koch-Dandolo, E. Castro-Camus, N. Riedl-Siedow, M. Koch, and W. Viöl, "Terahertz inspection of buildings and architectural art," Appl. Sci. **10**(15), 1–17 (2020).

88. K. Krugener, J. Ornik, M. Schneider, A. Jackel, E. Castro-Camus, M. Koch, and W. Viol, "On-site inspection of conservation works using THz TDS," in *2019 44th International Conference on Infrared, Millimeter, and Terahertz Waves (IRMMW-THz)* (IEEE, 2019), pp. 1–2.

89. F. E. M. Lambert, E. S. Reyes-Reyes, G. G. Hernandez-Cardoso, A. M. Gomez-Sepulveda, and E. Castro-Camus, "In situ Determination of the State of

Conservation of Paint Coatings on the Kiosk of Guadalajara Using Terahertz Time-Domain Spectroscopy," J. Infrared, Millimeter, Terahertz Waves **41**(4), 355–364 (2020).

90. C. L. Koch Dandolo, M. Picollo, C. Cucci, and P. U. Jepsen, "Fra Angelico's painting technique revealed by terahertz time-domain imaging (THz-TDI)," Appl. Phys. A Mater. Sci. Process. **122**(10), 1–8 (2016).

91. C. L. Koch Dandolo, M. Picollo, C. Cucci, M. Ginanni, E. Prandi, M. Scudieri, and P. U. Jepsen, "Insights on the Side Panels of the Franciscan Triptych by Fra Angelico Using Terahertz Time-Domain Imaging (THz-TDI)," J. Infrared, Millimeter, Terahertz Waves **38**(4), 413–424 (2017).

92. J. L. M. van Mechelen, A. Frank, and D. J. H. C. Maas, "Thickness sensor for drying paints using THz spectroscopy," Opt. Express **29**(5), 7514 (2021).

93. E. Castro-Camus, M. Koch, and D. M. Mittleman, "Recent advances in terahertz imaging: 1999 to 2021," Appl. Phys. B **128**(1), 12 (2022).

94. A. J. Fitzgerald, B. E. Cole, and P. F. Taday, "Nondestructive analysis of tablet coating thicknesses using Terahertz pulsed imaging," J. Pharm. Sci. **94**(1), 177–183 (2005).

95. J. A. Zeitler, Y. Shen, C. Baker, P. F. Taday, M. Pepper, and T. Rades, "Analysis of Coating Structures and Interfaces in Solid Oral Dosage Forms by Three Dimensional Terahertz Pulsed Imaging," J. Pharm. Sci. **96**(2), 330–340 (2007).

96. M. Haaser, K. Naelapää, K. C. Gordon, M. Pepper, J. Rantanen, C. J. Strachan, P. F. Taday, J. A. Zeitler, and T. Rades, "Evaluating the effect of coating equipment on tablet film quality using terahertz pulsed imaging," Eur. J. Pharm. Biopharm. **85**(3 PART B), 1095–1102 (2013).

97. Y. C. Shen, P. F. Taday, and M. Pepper, "Elimination of scattering effects in spectral measurement of granulated materials using terahertz pulsed spectroscopy," Appl. Phys. Lett. **92**(5), 1–4 (2008).

98. M. Franz, B. M. Fischer, and M. Walther, "The Christiansen effect in terahertz time-domain spectra of coarse-grained powders," Appl. Phys. Lett. **92**(2), (2008).

99. E. P. Parrott, J. A. Zeitler, and L. F. Gladden, "Accurate determination of optical coefficients from chemical samples using terahertz time-domain spectroscopy and effective medium theory," Opt. Lett. **34**(23), 3722 (2009).

100. M. Helliwell and D. Taylor, "Solid oral dosage forms," Prof. Nurse **8**(5), 313–317 (1993).

101. P. Bawuah and J. A. Zeitler, "Advances in terahertz time-domain spectroscopy of pharmaceutical solids: A review," TrAC - Trends Anal. Chem. **139**, 116272 (2021).

102. M. T. Ruggiero, J. J. Sutton, S. J. Fraser-Miller, A. J. Zaczek, T. M. Korter, K. C. Gordon, and J. A. Zeitler, "Revisiting the Thermodynamic Stability of Indomethacin Polymorphs with Low-Frequency Vibrational Spectroscopy and Quantum Mechanical Simulations," Cryst. Growth Des. **18**(11), 6513–6520 (2018).

103. M. Takahashi, "Terahertz Vibrations and Hydrogen-Bonded Networks in Crystals," crystals **4**(2), 74–103 (2014).

104. M. T. Ruggiero, "Invited Review: Modern Methods for Accurately Simulating the

Terahertz Spectra of Solids," J. Infrared, Millimeter, Terahertz Waves **41**(5), 491–528 (2020).

105. E. P. J. Parrott, J. A. Zeitler, T. Friščić, M. Pepper, W. Jones, G. M. Day, and L. F. Gladden, "Testing the sensitivity of terahertz spectroscopy to changes in molecular and supramolecular structure: A study of structurally similar cocrystal," Cryst. Growth Des. **9**(3), 1452–1460 (2009).

106. D. M. Charron, K. Ajito, J. Y. Kim, and Y. Ueno, "Chemical mapping of pharmaceutical cocrystals using terahertz spectroscopic imaging," Anal. Chem. **85**(4), 1980–1984 (2013).

107. C. J. Strachan, P. F. Taday, D. A. Newnham, K. C. Gordon, J. A. Zeitler, M. Pepper, and T. Rades, "Using terahertz pulsed spectroscopy to quantify pharmaceutical polymorphism and crystallinity," J. Pharm. Sci. **94**(4), 837–846 (2005).

108. A. I. McIntosh, B. Yang, S. M. Goldup, M. Watkinson, and R. S. Donnan, "Crystallization of amorphous lactose at high humidity studied by terahertz time domain spectroscopy," Chem. Phys. Lett. **558**, 104–108 (2013).

109. F. S. Vieira and C. Pasquini, "Determination of cellulose crystallinity by terahertz-time domain spectroscopy," Anal. Chem. **86**(8), 3780–3786 (2014).

110. I. Takeuchi, K. Shimakura, H. Kuroda, T. Nakajima, S. Goto, and K. Makino, "Estimation of Crystallinity of Nifedipine-Polyvinylpyrrolidone Solid Dispersion by Usage of Terahertz Time-Domain Spectroscopy and of X-Ray Powder Diffractometer," J. Pharm. Sci. **104**(12), 4307–4313 (2015).

111. J. A. Zeitler, K. Kogermann, J. Rantanen, T. Rades, P. F. Taday, M. Pepper, J. Aaltonen, and C. J. Strachan, "Drug hydrate systems and dehydration processes studied by terahertz pulsed spectroscopy," Int. J. Pharm. **334**(1–2), 78–84 (2007).

112. H. Liu and X.-C. Zhang, "Dehydration kinetics of D-glucose monohydrate studied using THz time-domain spectroscopy," Chem. Phys. Lett. **429**(1–3), 229–233 (2006).

113. J. A. Zeitler, P. F. Taday, M. Pepper, and T. Rades, "Relaxation and Crystallization of Amorphous Carbamazepine Studied by Terahertz Pulsed Spectroscopy," J. Pharm. Sci. **96**(10), 2703–2709 (2007).

114. J. Sibik, M. J. Sargent, M. Franklin, and J. A. Zeitler, "Crystallization and phase changes in paracetamol from the amorphous solid to the liquid phase," Mol. Pharm. **11**(4), 1326–1334 (2014).

115. G. Smith, A. Hussain, N. I. Bukhari, and I. Ermolina, "Quantification of residual crystallinity in ball milled commercially sourced lactose monohydrate by thermo-analytical techniques and terahertz spectroscopy," Eur. J. Pharm. Biopharm. **92**, 180–191 (2015).

116. J. Sibik, S. R. Elliott, and J. A. Zeitler, "Thermal decoupling of molecular-relaxation processes from the vibrational density of states at terahertz frequencies in supercooled hydrogen-bonded liquids," J. Phys. Chem. Lett. **5**(11), 1968–1972 (2014).

117. J. Sibik, K. Löbmann, T. Rades, and J. A. Zeitler, "Predicting Crystallization of Amorphous Drugs with Terahertz Spectroscopy," Mol. Pharm. **12**(8), 3062–3068 (2015).

118. J. A. Zeitler and J. Sibik, "Terahertz spectroscopy for predicting stability of amorphous drugs," U.S. patent US 9,683,934 B2 (2017).

119. Y.-C. Shen and P. F. Taday, "Development and Application of Terahertz Pulsed Imaging for Nondestructive Inspection of Pharmaceutical Tablet," IEEE J. Sel. Top. Quantum Electron. **14**(2), 407–415 (2008).

120. D. Alves-Lima, J. Song, X. Li, A. Portieri, Y. Shen, J. A. Zeitler, and H. Lin, "Review of terahertz pulsed imaging for pharmaceutical film coating analysis," Sensors **20**(5), 1–16 (2020).

121. D. Brock, J. Axel Zeitler, A. Funke, K. Knop, and P. Kleinebudde, "Evaluation of critical process parameters for inter-tablet coating uniformity of active-coated GITS using Terahertz Pulsed Imaging," Eur. J. Pharm. Biopharm. **88**(2), 434–442 (2014).

122. H. Lin, R. K. May, M. J. Evans, S. Zhong, L. F. Gladden, Y. Shen, and J. A. Zeitler, "Impact of Processing Conditions on Inter-tablet Coating Thickness Variations Measured by Terahertz In-Line Sensing," J. Pharm. Sci. **104**(8), 2513–2522 (2015).

123. L. Ho, R. Müller, M. Römer, K. C. Gordon, J. Heinämäki, P. Kleinebudde, M. Pepper, T. Rades, Y. C. Shen, C. J. Strachan, P. F. Taday, and J. A. Zeitler, "Analysis of sustained-release tablet film coats using terahertz pulsed imaging," J. Control. Release **119**(3), 253–261 (2007).

124. V. Malaterre, M. Pedersen, J. Ogorka, R. Gurny, N. Loggia, and P. F. Taday, "Terahertz pulsed imaging, a novel process analytical tool to investigate the coating characteristics of push-pull osmotic systems," Eur. J. Pharm. Biopharm. **74**(1), 21–25 (2010).

125. W. Momose, H. Yoshino, Y. Katakawa, K. Yamashita, K. Imai, K. Sako, E. Kato, A. Irisawa, E. Yonemochi, and K. Terada, "Applying terahertz technology for nondestructive detection of crack initiation in a film-coated layer on a swelling tablet," Results Pharma Sci. **2**(1), 29–37 (2012).

126. L. Ho, R. Müller, K. C. Gordon, P. Kleinebudde, M. Pepper, T. Rades, Y. Shen, P. F. Taday, and J. A. Zeitler, "Applications of terahertz pulsed imaging to sustained-release tablet film coating quality assessment and dissolution performance," J. Control. Release **127**(1), 79–87 (2008).

127. L. Ho, R. Müller, K. C. Gordon, P. Kleinebudde, M. Pepper, T. Rades, Y. Shen, P. F. Taday, and J. A. Zeitler, "Monitoring the Film Coating Unit Operation and Predicting Drug Dissolution Using Terahertz Pulsed Imaging," J. Pharm. Sci. **98**(12), 4866–4876 (2009).

128. J. A. Spencer, Z. Gao, T. Moore, L. F. Buhse, P. F. Taday, D. A. Newnham, Y. Shen, A. Portieri, and A. Husain, "Delayed Release Tablet Dissolution Related to Coating Thickness by Terahertz Pulsed Image Mapping," J. Pharm. Sci. **97**(4), 1543–1550 (2008).

129. R. K. May, M. J. Evans, S. Zhong, I. Warr, L. F. Gladden, Y. Shen, and J. A. Zeitler, "Terahertz In-Line Sensor for Direct Coating Thickness Measurement of Individual Tablets During Film Coating in Real-Time," J. Pharm. Sci. **100**(4), 1535–1544 (2011).

130. C. Pei, H. Lin, D. Markl, Y. C. Shen, J. A. Zeitler, and J. A. Elliott, "A quantitative

comparison of in-line coating thickness distributions obtained from a pharmaceutical tablet mixing process using discrete element method and terahertz pulsed imaging," Chem. Eng. Sci. **192**, 34–45 (2018).

131. H. Lin, Y. Dong, D. Markl, B. M. Williams, Y. Zheng, Y. Shen, and J. A. Zeitler, "Measurement of the Intertablet Coating Uniformity of a Pharmaceutical Pan Coating Process With Combined Terahertz and Optical Coherence Tomography In-Line Sensing," J. Pharm. Sci. **106**(4), 1075–1084 (2017).

132. S. Zhong, Y. C. Shen, L. Ho, R. K. May, J. A. Zeitler, M. Evans, P. F. Taday, M. Pepper, T. Rades, K. C. Gordon, R. Mller, and P. Kleinebudde, "Non-destructive quantification of pharmaceutical tablet coatings using terahertz pulsed imaging and optical coherence tomography," Opt. Lasers Eng. **49**(3), 361–365 (2011).

133. I. S. Russe, D. Brock, K. Knop, P. Kleinebudde, and J. A. Zeitler, "Validation of terahertz coating thickness measurements using X-ray microtomography," Mol. Pharm. **9**(12), 3551–3559 (2012).

134. K. Knop and P. Kleinebudde, "PAT-tools for process control in pharmaceutical film coating applications," Int. J. Pharm. **457**(2), 527–536 (2013).

135. J. A. Zeitler, P. F. Taday, D. A. Newnham, M. Pepper, K. C. Gordon, and T. Rades, "Terahertz pulsed spectroscopy and imaging in the pharmaceutical setting - a review," J. Pharm. Pharmacol. **59**(2), 209–223 (2007).

136. M. Haaser, K. C. Gordon, C. J. Strachan, and T. Rades, "Terahertz pulsed imaging as an advanced characterisation tool for film coatings - A review," Int. J. Pharm. **457**(2), 510–520 (2013).

137. S. Yassin, D. J. Goodwin, A. Anderson, J. Sibik, D. I. Wilson, L. F. Gladden, and J. A. Zeitler, "The Disintegration Process in Microcrystalline Cellulose Based Tablets, Part 1: Influence of Temperature, Porosity and Superdisintegrants," J. Pharm. Sci. **104**(10), 3440–3450 (2015).

138. M. Al-Sharabi, D. Markl, T. Mudley, P. Bawuah, A.-P. Karttunen, C. Ridgway, P. Gane, J. Ketolainen, K.-E. Peiponen, T. Rades, and J. A. Zeitler, "Simultaneous investigation of the liquid transport and swelling performance during tablet disintegration," Int. J. Pharm. **584**, 119380 (2020).

139. M. Riippi, J. Yliruusi, T. Niskanen, and J. Kiesvaara, "Dependence between dissolution rate and porosity of compressed erythromycin acistrate tablets," Eur. J. Pharm. Biopharm. **46**(2), 169–175 (1998).

140. M. Delalonde and T. Ruiz, "Dissolution of pharmaceutical tablets: The influence of penetration and drainage of interstitial fluids," Chem. Eng. Process. Process Intensif. **47**(3), 370–376 (2008).

141. D. Markl and J. A. Zeitler, "A Review of Disintegration Mechanisms and Measurement Techniques," Pharm. Res. **34**(5), 890–917 (2017).

142. D. Markl, A. Strobel, R. Schlossnikl, J. Bøtker, P. Bawuah, C. Ridgway, J. Rantanen, T. Rades, P. Gane, K.-E. Peiponen, and J. A. Zeitler, "Characterisation of pore structures of pharmaceutical tablets: A review," Int. J. Pharm. **538**(1–2), 188–214 (2018).

143. M. Juuti, H. Tuononen, T. Prykäri, V. Kontturi, M. Kuosmanen, E. Alarousu, J. Ketolainen, R. Myllylä, and K. E. Peiponen, "Optical and terahertz measurement techniques for flat-faced pharmaceutical tablets: A case study of gloss, surface

roughness and bulk properties of starch acetate tablets," Meas. Sci. Technol. **20**(1), (2009).

144. P. Bawuah, D. Markl, D. Farrell, M. Evans, A. Portieri, A. Anderson, D. Goodwin, R. Lucas, and J. A. Zeitler, "Terahertz-Based Porosity Measurement of Pharmaceutical Tablets: a Tutorial," J. Infrared, Millimeter, Terahertz Waves **41**(4), 450–469 (2020).

145. P. Bawuah, P. Silfsten, T. Ervasti, J. Ketolainen, J. A. Zeitler, and K. E. Peiponen, "Non-contact weight measurement of flat-faced pharmaceutical tablets using terahertz transmission pulse delay measurements," Int. J. Pharm. **476**(1), 16–22 (2014).

146. P. Bawuah, T. Ervasti, N. Tan, J. A. Zeitler, J. Ketolainen, and K. E. Peiponen, "Noninvasive porosity measurement of biconvex tablets using terahertz pulses," Int. J. Pharm. **509**(1–2), 439–443 (2016).

147. D. Markl, P. Wang, C. Ridgway, A. P. Karttunen, M. Chakraborty, P. Bawuah, P. Pääkkönen, P. Gane, J. Ketolainen, K. E. Peiponen, and J. A. Zeitler, "Characterization of the Pore Structure of Functionalized Calcium Carbonate Tablets by Terahertz Time-Domain Spectroscopy and X-Ray Computed Microtomography," J. Pharm. Sci. **106**(6), 1586–1595 (2017).

148. D. Markl, P. Bawuah, C. Ridgway, S. van den Ban, D. J. Goodwin, J. Ketolainen, P. Gane, K.-E. Peiponen, and J. A. Zeitler, "Fast and non-destructive pore structure analysis using terahertz time-domain spectroscopy," Int. J. Pharm. **537**(1–2), 102–110 (2018).

149. C. Ridgway, P. Bawuah, D. Markl, J. A. Zeitler, J. Ketolainen, K. E. Peiponen, and P. Gane, "On the role of API in determining porosity, pore structure and bulk modulus of the skeletal material in pharmaceutical tablets formed with MCC as sole excipient," Int. J. Pharm. **526**(1–2), 321–331 (2017).

150. P. Pawar, Y. Wang, G. Keyvan, G. Callegari, A. Cuitino, and F. Muzzio, "Enabling real time release testing by NIR prediction of dissolution of tablets made by continuous direct compression (CDC)," Int. J. Pharm. **512**(1), 96–107 (2016).

151. R. B. Shah, M. A. Tawakkul, and M. A. Khan, "Process Analytical Technology: Chemometric Analysis of Raman and Near Infra-Red Spectroscopic Data for Predicting Physical Properties of Extended Release Matrix Tablets," J. Pharm. Sci. **96**(5), 1356–1365 (2007).

152. P. Bawuah, D. Markl, A. Turner, M. Evans, A. Portieri, D. Farrell, R. Lucas, A. Anderson, D. J. Goodwin, and J. A. Zeitler, "A Fast and Non-destructive Terahertz Dissolution Assay for Immediate Release Tablets," J. Pharm. Sci. **110**(5), 2083–2092 (2021).

153. D. Markl, M. Warman, M. Dumarey, E. L. Bergman, S. Folestad, Z. Shi, L. F. Manley, D. J. Goodwin, and J. A. Zeitler, "Review of real-time release testing of pharmaceutical tablets: State-of-the art, challenges and future perspective," Int. J. Pharm. **582**(January), 119353 (2020).

154. X. Lu, H. Sun, T. Chang, J. Zhang, and H. L. Cui, "Terahertz detection of porosity and porous microstructure in pharmaceutical tablets: A review," Int. J. Pharm. **591**, 120006 (2020).

155. R. A. Bader and D. A. Putnam, *Engineering Polymer Systems for Improved Drug*

Delivery (John Wiley & Sons, Inc., 2013).

156. T. Takagi, C. Ramachandran, M. Bermejo, S. Yamashita, L. X. Yu, and G. L. Amidon, "A Provisional Biopharmaceutical Classification of the Top 200 Oral Drug Products in the United States, Great Britain, Spain, and Japan," Mol. Pharm. **3**(6), 631–643 (2006).

157. M. U. Mehta, R. S. Uppoor, D. P. Conner, P. Seo, J. Vaidyanathan, D. A. Volpe, E. Stier, D. Chilukuri, A. Dorantes, T. Ghosh, H. Mandula, K. Raines, P. Dhanormchitphong, J. Woodcock, and L. X. Yu, "Impact of the US FDA "biopharmaceutics Classification System" (BCS) Guidance on Global Drug Development," Mol. Pharm. **14**(12), 4334–4338 (2017).

158. FDA, "M9 Biopharmaceutics Classification System-Based Biowaivers Guidance for Industry," (2021).

159. Y. Tsume, D. M. Mudie, P. Langguth, G. E. Amidon, and G. L. Amidon, "The Biopharmaceutics Classification System: Subclasses for in vivo predictive dissolution (IPD) methodology and IVIVC," Eur. J. Pharm. Sci. **57**(1), 152–163 (2014).

160. N. A. Kasim, M. Whitehouse, C. Ramachandran, M. Bermejo, H. Lennernäs, A. S. Hussain, H. E. Junginger, S. A. Stavchansky, K. K. Midha, V. P. Shah, and G. L. Amidon, "Molecular Properties of WHO Essential Drugs and Provisional Biopharmaceutical Classification," Mol. Pharm. **1**(1), 85–96 (2004).

161. O. Wolk, R. Agbaria, and A. Dahan, "Provisional in-silico biopharmaceutics classification (BCS) to guide oral drug product development," Drug Des. Devel. Ther. **8**, 1563–1575 (2014).

162. J.-M. delMoral-Sanchez, I. Gonzalez-Alvarez, M. Gonzalez-Alvarez, A. Navarro, and M. Bermejo, "Classification of WHO Essential Oral Medicines for Children Applying a Provisional Pediatric Biopharmaceutics Classification System," Pharmaceutics **11**(11), 567 (2019).

163. L. Z. Benet, "The role of BCS (biopharmaceutics classification system) and BDDCS (biopharmaceutics drug disposition classification system) in drug development," J. Pharm. Sci. **102**(1), 34–42 (2013).

164. C. Y. Wu and L. Z. Benet, "Predicting drug disposition via application of BCS: Transport/absorption/ elimination interplay and development of a biopharmaceutics drug disposition classification system," Pharm. Res. **22**(1), 11–23 (2005).

165. H. D. Williams, N. L. Trevaskis, S. A. Charman, R. M. Shanker, W. N. Charman, C. W. Pouton, and C. J. H. Porter, "Strategies to address low drug solubility in discovery and development," Pharmacol. Rev. **65**(1), 315–499 (2013).

166. K. C. Johnson and A. C. Swindell, "Guidance in the setting of drug particle size specifications to minimize variability in absorption," Pharm. Res. **13**(12), 1795–1798 (1996).

167. F. Sardari and A. Jouyban, "Solubility of Nifedipine in Ethanol + Water and Propylene Glycol + Water Mixtures at 293.2 to 313.2 K," Ind. Eng. Chem. Res. **52**(40), 14353–14358 (2013).

168. A. A. Noyes and W. R. Whitney, "THE RATE OF SOLUTION OF SOLID SUBSTANCES IN THEIR OWN SOLUTIONS.," J. Am. Chem. Soc. **19**(12), 930–

934 (1897).

169. A. Martin, *Physical Pharmacy*, 4th ed. (B.I. Waverly Pvt Ltd, 1993).

170. J. Bauer, S. Spanton, R. Henry, J. Quick, W. Dziki, W. Porter, and J. Morris, "Ritonavir: An Extraordinary Example of Conformational Polymorphism," Pharm. Res. **18**, 859–866 (2001).

171. S. B. Murdande, M. J. Pikal, R. M. Shanker, and R. H. Bogner, "Solubility advantage of amorphous pharmaceuticals: I. A thermodynamic analysis," J. Pharm. Sci. **99**(3), 1254–1264 (2010).

172. R. B. Chavan, R. Thipparaboina, D. Kumar, and N. R. Shastri, "Co amorphous systems: A product development perspective," Int. J. Pharm. **515**(1–2), 403–415 (2016).

173. G. C. Viscomi, M. Campana, M. Barbanti, F. Grepioni, M. Polito, D. Confortini, G. Rosini, P. Righi, V. Cannata, and D. Braga, "Crystal forms of rifaximin and their effect on pharmaceutical properties," CrystEngComm **10**(8), 1074 (2008).

174. K. E. N. K. Qian and R. H. Bogner, "Application of Mesoporous Silicon Dioxide and Silicate in Oral Amorphous Drug Delivery Systems," J. Pharm. Sci. **101**(2), 444–463 (2012).

175. S. Chaudhari and A. Gupte, "Mesoporous Silica as a Carrier for Amorphous Solid Dispersion," Br. J. Pharm. Res. **16**(6), 1–19 (2017).

176. J. Ornik, D. Knoth, M. Koch, and C. M. Keck, "Terahertz-spectroscopy for non-destructive determination of crystallinity of L-tartaric acid in smartFilms® and tablets made from paper," Int. J. Pharm. **581**, 119253 (2020).

177. F. Stumpf and C. M. Keck, "Tablets made from paper," Int. J. Pharm. **548**(2), 812–819 (2018).

178. F. Stumpf, "Tabletten aus Papier – tablets made from paper – zur oralen Applikation schwerlöslicher Wirkstoffe," PhD Thesis, Philipps-Universität Marburg (2019).

179. R. W. Eckert, S. Wiemann, and C. M. Keck, "Improved Dermal and Transdermal Delivery of Curcumin with SmartFilms and Nanocrystals," Molecules **26**(6), 1633 (2021).

180. R. Nishikiori, M. Yamaguchi, K. Takano, T. Enatsu, M. Tani, U. C. de Silva, N. Kawashita, T. Takagi, S. Morimoto, M. Hangyo, and M. Kawase, "Application of Partial Least Square on Quantitative Analysis of L-, D-, and DL-Tartaric Acid by Terahertz Absorption Spectra," Chem. Pharm. Bull. (Tokyo). **56**(3), 305–307 (2008).

181. A. Soltani, D. Gebauer, L. Duschek, B. M. Fischer, H. Cölfen, and M. Koch, "Crystallization Caught in the Act with Terahertz Spectroscopy: Non-Classical Pathway for l-(+)-Tartaric Acid," Chem. - A Eur. J. **23**(57), 14128–14132 (2017).

182. E. M. Witko and T. M. Korter, "Investigation of the low-frequency vibrations of crystalline tartaric acid using terahertz spectroscopy and solid-state density functional theory," J. Phys. Chem. A **115**(35), 10052–10058 (2011).

183. S. P. Velaga, D. Nikjoo, and P. R. Vuddanda, "Experimental Studies and Modeling of the Drying Kinetics of Multicomponent Polymer Films," AAPS PharmSciTech

19(1), 425–435 (2018).

184. "THz Spectral Database for Pharmaceuticals, TSDBP (Absorbance)," https://www.rie.shizuoka.ac.jp/~thz/shizuoka_univ_sasaki_lab_database/group_ absorbance_index.html.

185. "Terahertz Database," http://thzdb.org/.

186. K. Löbmann, R. Laitinen, H. Grohganz, K. C. Gordon, C. Strachan, and T. Rades, "Coamorphous drug systems: Enhanced physical stability and dissolution rate of indomethacin and naproxen," Mol. Pharm. **8**(5), 1919–1928 (2011).

187. A. A. Somani, K. Thelen, S. Zheng, M. N. Trame, K. Coboeken, M. Meyer, K. Schnizler, I. Ince, S. Willmann, and S. Schmidt, "Evaluation of changes in oral drug absorption in preterm and term neonates for Biopharmaceutics Classification System (BCS) class i and II compounds," Br. J. Clin. Pharmacol. **81**(1), 137–147 (2016).

188. J. Patterson, A. Bary, and T. Rades, "Physical stability and solubility of the thermotropic mesophase of fenoprofen calcium as pure drug and in a tablet formulation," Int. J. Pharm. **247**(1–2), 147–157 (2002).

189. S. J. Jung, S. O. Choi, S. Y. Um, J. Il Kim, H. Y. P. Choo, S. Y. Choi, and S. Y. Chung, "Prediction of the permeability of drugs through study on quantitative structure–permeability relationship," J. Pharm. Biomed. Anal. **41**(2), 469–475 (2006).

190. I. Kovačević, J. Parojčić, I. Homšek, M. Tubić-Grozdanis, and P. Langguth, "Justification of Biowaiver for Carbamazepine, a Low Soluble High Permeable Compound, in Solid Dosage Forms Based on IVIVC and Gastrointestinal Simulation," Mol. Pharm. **6**(1), 40–47 (2009).

191. E. M. Sorkin, S. P. Clissold, and R. N. Brogden, "Nifedipine A Review of Its Pharmacodynamic and Pharmacokinetic Properties, and Therapeutic Efficacy, in Ischaemic Heart Disease, Hypertension and Related Cardiovascular Disorders," Drugs **30**(3), 182–274 (1985).

192. A. M. Nader, S. K. Quinney, H. M. Fadda, and D. R. Foster, "Effect of Gastric Fluid Volume on the In Vitro Dissolution and In Vivo Absorption of BCS Class II Drugs: a Case Study with Nifedipine," AAPS J. **18**(4), 981–988 (2016).

193. P. J. Marsac, H. Konno, and L. S. Taylor, "A comparison of the physical stability of amorphous felodipine and nifedipine systems," Pharm. Res. **23**(10), 2306–2316 (2006).

194. M. J. Mora, R. Onnainty, and G. E. Granero, "Comparative Oral Drug Classification Systems: Acetazolamide, Azithromycin, Clopidogrel, and Efavirenz Case Studies," Mol. Pharm. **15**(8), 3187–3196 (2018).

195. S. A. Breda, A. F. Jimenez-Kairuz, R. H. Manzo, and M. E. Olivera, "Solubility behavior and biopharmaceutical classification of novel high-solubility ciprofloxacin and norfloxacin pharmaceutical derivatives," Int. J. Pharm. **371**(1–2), 106–113 (2009).

196. J. Shen, G. Wang, D. Jiang, L. Liang, and X. Xu, "Terahertz spectroscopic investigations of caffeine and 3-acetylmorphine," Optik (Stuttg). **121**(18), 1712–1716 (2010).

197. A. Nakanishi, K. Akiyama, S. Hayashi, H. Satozono, and K. Fujita, "Spectral imaging of pharmaceutical materials with a compact terahertz difference-frequency generation semiconductor source," Anal. Methods **13**(46), 5549–5554 (2021).

198. M. D. King, W. D. Buchanan, and T. M. Korter, "Understanding the Terahertz Spectra of Crystalline Pharmaceuticals: Terahertz Spectroscopy and Solid-State Density Functional Theory Study of (S)-(+)-Ibuprofen and (RS)-Ibuprofen," J. Pharm. Sci. **100**(3), 1116–1129 (2011).

199. W. Liu, Y. Liu, J. Huang, Z. Lin, X. Pan, X. Zeng, M. Lamy de la Chapelle, Y. Zhang, and W. Fu, "Identification and investigation of the vibrational properties of crystalline and co-amorphous drugs with Raman and terahertz spectroscopy," Biomed. Opt. Express **10**(8), 4290 (2019).

200. Y. Long, B. Li, and H. Liu, "Analysis of fluoroquinolones antibiotic residue in feed matrices using terahertz spectroscopy," Appl. Opt. **57**(3), 544–550 (2018).

201. M. Mazik, "Promising Therapeutic Approach for SARS-CoV-2 Infections by Using a Rutin-Based Combination Therapy," ChemMedChem **17**(11), (2022).

202. S. J. Dengale, S. S. Hussen, B. S. M. Krishna, P. B. Musmade, G. Gautham Shenoy, and K. Bhat, "Fabrication, solid state characterization and bioavailability assessment of stable binary amorphous phases of Ritonavir with Quercetin," Eur. J. Pharm. Biopharm. **89**, 329–338 (2015).

203. M. Chen, C. Xie, and L. Liu, "Solubility of Hesperetin in Various Solvents from (288.2 to 323.2) K," J. Chem. Eng. Data **55**(5297–5298), 1649–1650 (2010).

204. M. K. Anwer, R. Al-Shdefat, S. Jamil, P. Alam, M. S. Abdel-Kader, and F. Shakeel, "Solubility of Bioactive Compound Hesperidin in Six Pure Solvents at (298.15 to 333.15) K," J. Chem. Eng. Data **59**(6), 2065–2069 (2014).

205. M. Xiao, Y. Shao, W. Yan, and Z. Zhang, "Measurement and correlation of solubilities of apigenin and apigenin 7-O-rhamnosylglucoside in seven solvents at different temperatures," J. Chem. Thermodyn. **43**(3), 240–243 (2011).

206. K. Bisht, K. H. Wagner, and A. C. Bulmer, "Curcumin, resveratrol and flavonoids as anti-inflammatory, cyto- and DNA-protective dietary compounds," Toxicology **278**(1), 88–100 (2010).

207. A. E. Rotelli, T. Guardia, A. O. Juárez, N. E. De La Rocha, and L. E. Pelzer, "Comparative study of flavonoids in experimental models of inflammation," Pharmacol. Res. **48**(6), 601–606 (2003).

208. H. Parhiz, A. Roohbakhsh, F. Soltani, R. Rezaee, and M. Iranshahi, "Antioxidant and Anti-Inflammatory Properties of the Citrus Flavonoids Hesperidin and Hesperetin: An Updated Review of their Molecular Mechanisms and Experimental Models," Phyther. Res. **29**(3), 323–331 (2015).

209. S. Hewlings and D. Kalman, "Curcumin: A Review of Its Effects on Human Health," Foods **6**(10), 92 (2017).

210. G. N. Kalinkova, "Studies of beneficial interactions between active medicaments and excipients in pharmaceutical formulations," Int. J. Pharm. **187**(1), 1–15 (1999).

211. G. Thoorens, F. Krier, B. Leclercq, B. Carlin, and B. Evrard, "Microcrystalline

cellulose, a direct compression binder in a quality by design environment - A review," Int. J. Pharm. **473**(1–2), 64–72 (2014).

212. L. Hu, Y. Shi, J. H. Li, N. Gao, J. Ji, F. Niu, Q. Chen, X. Yang, and S. Wang, "Enhancement of Oral Bioavailability of Curcumin by a Novel Solid Dispersion System," AAPS PharmSciTech **16**(6), 1327–1334 (2015).

213. K. E. Bowe, "Recent advances in sugar-based excipients," Pharm. Sci. Technol. Today **1**(4), 166–173 (1998).

214. H. K. Srivastava, S. Wolfgang, and J. D. Rodriguez, "Expanding the analytical toolbox for identity testing of pharmaceutical ingredients: Spectroscopic screening of dextrose using portable Raman and near infrared spectrometers," Anal. Chim. Acta **914**, 91–99 (2016).

215. T. Alzoubi, G. P. Martin, D. J. Barlow, and P. G. Royall, "Stability of α-lactose monohydrate: The discovery of dehydration triggered solid-state epimerization," Int. J. Pharm. **604**, 120715 (2021).

216. S. Wang, J. Li, X. Lin, Y. Feng, X. Kou, S. Babu, and R. Panicucci, "Novel coprocessed excipients composed of lactose, HPMC, and PVPP for tableting and its application," Int. J. Pharm. **486**(1–2), 370–379 (2015).

217. N. Baber, L. D. C. Halliday, W. J. A. Van Den Heuvel, R. W. Walker, R. Sibeon, J. P. Keenan, T. Littler, and M. L. Orme, "Indomethacin in rheumatoid arthritis: clinical effects, pharmacokinetics, and platelet studies in responders and nonresponders," Ann. Rheum. Dis. **38**(2), 128–136 (1979).

218. S. Lucas, "The Pharmacology of Indomethacin," Headache J. Head Face Pain **56**(2), 436–446 (2016).

219. C. J. Strachan, T. Rades, and K. C. Gordon, "A theoretical and spectroscopic study of γ-crystalline and amorphous indometacin," J. Pharm. Pharmacol. **59**(2), 261–269 (2007).

220. M. Yoshioka, B. C. Hancock, and G. Zografi, "Crystallization of indomethacin from the amorphous state below and above its glass transition temperature," J. Pharm. Sci. **83**(12), 1700–1705 (1994).

221. V. Andronis and G. Zografi, "Crystal nucleation and growth of indomethacin polymorphs from the amorphous state," J. Non. Cryst. Solids **271**(3), 236–248 (2000).

222. N. KANENIWA, M. OTSUKA, and T. HAYASHI, "Physicochemical characterization of indomethacin polymorphs and the transformation kinetics in ethanol," Chem. Pharm. Bull. **33**(8), 3447–3455 (1985).

223. S. Hellstén, H. Qu, and M. Louhi-Kultanen, "Screening of Binary Solvent Mixtures and Solvate Formation of Indomethacin," Chem. Eng. Technol. **34**(10), 1667–1674 (2011).

224. T. Watanabe, N. Wakiyama, F. Usui, M. Ikeda, T. Isobe, and M. Senna, "Stability of amorphous indomethacin compounded with silica," Int. J. Pharm. **226**(1–2), 81–91 (2001).

225. C. R. Malwade and H. Qu, "Cooling Crystallization of Indomethacin: Effect of Supersaturation, Temperature, and Seeding on Polymorphism and Crystal Size Distribution," Org. Process Res. Dev. **22**(6), 697–706 (2018).

226. J. Ornik, L. Heidrich, R. Schesny, E. Castro-Camus, C. M. Keck, and M. Koch, "Non-destructive crystallinity assessment of indomethacin in tablets made from smartFilms® using terahertz time-domain spectroscopy," Sci. Rep. **12**(1), 6099 (2022).

227. J. Ornik, L. Heidrich, R. Schesny, C. M. Keck, E. Castro-Camus, and M. Koch, "THz TDS of SmartFilms® Loaded with Indomethacin," in *International Conference on Infrared, Millimeter, and Terahertz Waves, IRMMW-THz* (IEEE, 2021).

228. H. Ishida, T. Wu, and L. Yu, "Sudden Rise of Crystal Growth Rate of Nifedipine near Tg without and with Polyvinylpyrrolidone," J. Pharm. Sci. **96**(5), 1131–1138 (2007).

229. Y. Sun, J. Tao, G. G. Z. Zhang, and L. Yu, "Solubilities of Crystalline Drugs in Polymers: An Improved Analytical Method and Comparison of Solubilities of Indomethacin and Nifedipine in PVP, PVP/VA, and PVAc," J. Pharm. Sci. **99**(9), 4023–4031 (2010).

230. A. Alqurshi, K. L. Andrew Chan, and P. G. Royall, "In-situ freeze-drying-forming amorphous solids directly within capsules: An investigation of dissolution enhancement for a poorly soluble drug," Sci. Rep. **7**(1), 1–16 (2017).

231. S. Ayyoubi, J. R. Cerda, R. Fernández-García, P. Knief, A. Lalatsa, A. M. Healy, and D. R. Serrano, "3D printed spherical mini-tablets: Geometry versus composition effects in controlling dissolution from personalised solid dosage forms," Int. J. Pharm. **597**(December 2020), 120336 (2021).

232. E. O. Kissi, H. Grohganz, K. Löbmann, M. T. Ruggiero, J. A. Zeitler, and T. Rades, "Glass-Transition Temperature of the β-Relaxation as the Major Predictive Parameter for Recrystallization of Neat Amorphous Drugs," J. Phys. Chem. B **122**(10), 2803–2808 (2018).

233. S. A. Sánchez-Guirales, N. Jurado, A. Kara, A. Lalatsa, and D. R. Serrano, "Understanding Direct Powder Extrusion for Fabrication of 3D Printed Personalised Medicines: A Case Study for Nifedipine Minitablets," Pharmaceutics **13**(10), (2021).

234. P. Wang, J. Zhao, Y. Zhang, Z. Zhu, L. Liu, H. Zhao, X. Yang, X. Yang, X. Sun, and M. He, "The fingerprints of nifedipine/isonicotinamide cocrystal polymorph studied by terahertz time-domain spectroscopy," Int. J. Pharm. **620**, 121759 (2022).

235. G. Takebe, Y. Kawada, K. Akiyama, H. Takahashi, H. Takamoto, and M. Hiramatsu, "Evaluation of drug crystallinity in aqueous suspension using terahertz time-domain attenuated total reflection spectroscopy," J. Pharm. Sci. **102**(11), 4065–4071 (2013).

Scientific contributions

Here the contributions to the results presented in this work are acknowledged.

Dr. Daniel Knoth prepared the smartFilms loaded with LTA and the physical mixtures presented in section 4.2. He also performed the XRD and DSC measurements presented in chapter 4. Osama Farooqui helped with the THz TDS measurements presented in section 4.2.

Prof. Cornelia M. Keck provided part of the APIs presented in chapter 5.

Lara Heidrich, who I supervised during her time as a master's student in the group, prepared the tablets made from smartFilms loaded with IM and prepared physical mixtures presented in chapter 6 with help of Robert Schesny. She also helped with the THz TDS measurements of the samples and the extraction of the absorption coefficient. She prepared the recrystallized sample and conducted the DSC measurements presented in chapter 6 with the help of Philipp Kahler and Sebastian Inacker. Dr. Abhishek K. Singh was involved in the discussion of the DSC results.

Prof. Enrique Castro-Camus initialized the concept of the quantitative analysis and helped with the interpretation of the results presented in chapter 6.

Prof. Martin Koch and Prof. Cornelia M. Keck helped with the interpretation of the results presented in chapters 4 and 6.

Lara Heidrich prepared tablets made from smartFilms with and without PVP, conducted the THz TDS measurements, and helped with the data analysis of the results presented in section 7.2.

Prof. Martin Koch supervised the whole work.

List of publications

Publications in peer-reviewed scientific journals:

1. F. E. M. Lambert, J. Ornik, N.-A. Staats, A. Jäckel, G. G. Hernandez-Cardoso, J. Taiber, E.-M. Stübling, B. Rudolph, O. Mack, H. Portsteffen, E. Castro-Camus, and M. Koch, "Layer separation mapping and consolidation evaluation of a fifteenth century panel painting using terahertz time-domain imaging," Sci. Rep. **12**(1), 21038 (2022).

2. A. Jäckel, D. Ulm, T. Kleine-Ostmann, E. Castro-Camus, M. Koch, and J. Ornik, "Achromatic Quarter-Waveplate for the Terahertz Frequency Range Made by 3D Printing," J. Infrared, Millimeter, Terahertz Waves **43**(7–8), 573–581 (2022).

3. J. Ornik, L. Heidrich, R. Schesny, E. Castro-Camus, C. M. Keck, and M. Koch, "Non-destructive crystallinity assessment of indomethacin in tablets made from smartFilms® using terahertz time-domain spectroscopy," Sci. Rep. **12**(1), 6099 (2022).

4. J. Deng, F. Taleb, J. Ornik, E. Ding, M. Koch, and E. Castro-Camus, "Quantitative Assessment of Rock-Coal Powder Mixtures by Terahertz Time Domain Spectroscopy," J. Infrared, Millimeter, Terahertz Waves **42**(7), 742 (2021).

5. J. Ornik, M. Sakaki, M. Koch, J. C. Balzer, and N. Benson, "3D Printed Al_2O_3 for Terahertz Technology," IEEE Access **9**, 5986 (2021).

6. E. Castro-Camus, J. Ornik, C. Mach, G. Hernandez-Cardoso, B. Savalia, J. Taiber, A. Ruiz-Marquez, K. Kesper, S. Konde, C. Sommer, J. Wiener, D. Geisel, F. Hüppe, G. Kräling, P. Mross, J. Nguyen, T. Wiesmann, B. Beutel, and M. Koch, "Simple Ventilators for Emergency Use Based on Bag-Valve Pressing Systems: Lessons Learned and Future Steps," Appl. Sci. **10**(20), 7229 (2020).

7. J. Deng, J. Ornik, K. Zhao, E. Ding, M. Koch, and E. Castro-Camus, "Recognition of coal from other minerals in powder form using terahertz spectroscopy," Opt. Express **28**(21), 30943 (2020).

8. J. Ornik, J. Lehr, M. Reuter, D. Jahn, F. Beltran-Mejia, J. Balzer, T. Kleine-Ostmann, and M. Koch, "Repeatability of material parameter extraction of liquids from transmission terahertz time-domain measurements," Opt. Express **28**(19), 28178 (2020).

9. K. Krügener, J. Ornik, L. M. Schneider, A. Jäckel, C. L. Koch-Dandolo, E. Castro-Camus, N. Riedl-Siedow, M. Koch, and W. Viöl, "Terahertz inspection of buildings and architectural art," Appl. Sci. **10**(15), 1 (2020).

10. S. Konde, J. Ornik, J. A. Prume, J. Taiber, and M. Koch, "Exploring the potential of photoluminescence spectroscopy in combination with Nile Red staining for microplastic detection," Mar. Pollut. Bull. **159**, 111475 (2020).

11. M. Mikerov, J. Ornik, and M. Koch, "Removing Water Vapor Lines From THz-TDS Data Using Neural Networks," IEEE Trans. Terahertz Sci. Technol. **10**(4), 397 (2020).

12. J. Ornik, D. Knoth, M. Koch, and C. M. Keck, "Terahertz-spectroscopy for non-destructive determination of crystallinity of L-tartaric acid in smartFilms® and tablets made from paper," Int. J. Pharm. **581**, 119253 (2020).

13. J. Ornik, S. Sommer, S. Gies, M. Weber, C. Lott, J. C. Balzer, and M. Koch, "Could photoluminescence spectroscopy be an alternative technique for the detection of microplastics? First experiments using a 405 nm laser for excitation," Appl. Phys. B **126**(1), 15 (2020).

14. K. Krügener, J. Ornik, R. Jachim, B. Kietz, K. Petersen, D. M. Mittleman, M. Koch, and W. Viöl, "Monitoring fungus infestation of common beech wood using terahertz radiation," Holzforschung **74**(7), 635 (2020).

15. M. Taherkhani, R. A. Sadeghzadeh, J. Taiber, J. Ornik, and M. Koch, "The Effect of Humidity and Temperature on Dielectric Fibre–Bound THz Transmission," J. Infrared, Millimeter, Terahertz Waves **40**(11–12), 1092 (2019).

16. A. Abdul-Munaim, J. Ornik, M. Koch, and D. Watson, "Terahertz Time Domain Spectroscopy to Detect Different Oxidation Levels of Diesel Engine Oil," Lubricants **7**(2), 18 (2019).

17. J. Ornik, L. Gomell, S. F. Busch, M. Hermans, and M. Koch, "High quality terahertz glass wave plates," Opt. Express **26**(25), 32631 (2018).

Conference contributions:

1. J. Ornik, L. Heidrich, C. M. Keck, E. Castro-Camus, and M. Koch, "THz TDS of Nifedipine in Tablets Made from Cellulose," in International Conference on Infrared, Millimeter, and Terahertz Waves, IRMMW-THz (IEEE, 2022).

2. L. Heidrich, J. Ornik, C. M. Keck, E. Castro-Camus, and M. Koch, " Terahertz spectroscopy for non-destructive investigation of crystalline Nifedipine in tablets made from smartFilms®," in International Conference on Infrared, Millimeter, and Terahertz Waves, IRMMW-THz (IEEE, 2022).

3. F. E. M. Lambert, J. Ornik, N. Staats, A. Jäckel1, J. Taiber, G. G. Hernandez, E. Stübling, B. Rudolph, O. Mack, H. Portsteffen, E. Castro-Camus, and M. Koch, "Paint layer delamination mapping before and after consolidation of a 15th century painting using THz-TDI," in International Conference on Infrared, Millimeter, and Terahertz Waves, IRMMW-THz (IEEE, 2022).

4. A. Jäckel, D. Ulm, T. Kleine-Ostmann, E. Castro-Camus, M. Koch, and J. Ornik, " Three-dimensional printed achromatic λ/4 waveplate for the THz

frequnecy range," in International Conference on Infrared, Millimeter, and Terahertz Waves, IRMMW-THz (IEEE, 2022).

5. J. Ornik, L. Heidrich, R. Schesny, D. Knoth, C. M. Keck, E. Castro-Camus, and M. Koch, "Inspecting the solid state of pharmaceuticals dispersed in a paper matrix using THz TDS (invited)," in IEEE Summer Topicals Meeting Series (IEEE, 2022).

6. J. Ornik, L. Heidrich, R. Schesny, C. M. Keck, E. Castro-Camus, and M. Koch, "THz TDS of SmartFilms® Loaded with Indomethacin," in International Conference on Infrared, Millimeter, and Terahertz Waves, IRMMW-THz (IEEE, 2021).

7. J. Ornik, M. Sakaki, M. Koch, J. C. Balzer, and N. Benson, "Dielectric Properties of 3D Printed Alumina in the THz Range," in International Conference on Infrared, Millimeter, and Terahertz Waves, IRMMW-THz (IEEE, 2021).

8. J. Ornik, D. Knoth, C. M. Keck, and M. Koch, "Potential of THz-TDS for Crystallinity State Inspection of Active Pharmaceutical Ingredients in SmartFilms®," in International Conference on Infrared, Millimeter, and Terahertz Waves, IRMMW-THz (IEEE, 2020).

9. J. Ornik, N. A. Staats, E. M. Stubling, H. D. Portsteffen, and M. Koch, "Using THz-TDI for Identification of Paint Layer Delamination and Control of its Consolidation," in International Conference on Infrared, Millimeter, and Terahertz Waves, IRMMW-THz (IEEE, 2020).

10. D. Knoth, J. Ornik, M. Koch, and C. M. Keck, "Terahertz spectroscopy for crystallinity investigation of smartFilms®", in Spanish-Portuguese Conference on Controlled Drug Delivery (2020)

11. J. Ornik, Y. Zhang, M. Schneider, M. Taherkhani, H. Alaboz, and M. Koch, "THz gratings produced by laser cutting," in International Conference on Infrared, Millimeter, and Terahertz Waves, IRMMW-THz (IEEE, 2019).

12. M. Mikerov, J. Ornik, and M. Koch, "Deep Learning Approach for Removal of Water Vapor Effects from THz-TDS Signals," in International Conference on Infrared, Millimeter, and Terahertz Waves, *IRMMW-THz* (IEEE, 2019).

13. K. Krugener, J. Ornik, M. Schneider, A. Jackel, E. Castro-Camus, M. Koch, and W. Viol, "On-site inspection of conservation works using THz TDS," in International Conference on Infrared, Millimeter, and Terahertz Waves, IRMMW-THz (IEEE, 2019).

14. D. Knoth, J. Ornik, F. Stumpf, M. Koch, C. M. Keck, "Terahertz spectroscopy for crystallinity investigation of hesperitin smartFilms®," in Annual Meeting of the Controlled Release Society (2019).

15. D. Knoth, J. Ornik, M. Koch, C. M. Keck, "Terahertz Spectroscopy in pharmaceutical sciences – Crystallinity investigation of smartFilms®," in European Conference on Pharmaceutics. (2019).

16. J. Ornik, D. Knoth, C. M. Keck, M. Koch, "Inspecting the crystallinity state of an active substance deposited on a paper using terahertz time-domain

spectroscopy," in International Conference on Optical Terahertz Science and Technology, OTST (2019).

17. J. Ornik, M. Mikerov and M. Koch, "Removal of water vapor absorption lines from terahertz time-domain signals using neural networks," in International Conference on Optical Terahertz Science and Technology, OTST (2019).

18. H. Alaboz, M. Schneider, J. Ornik, E. Stübling, D. Jahn, and M. Koch, „A laser cut THz metal mesh bandpass filter with high transmission," in EOS Topical Meeting on Terahertz Science and Technology, (2018).

19. J. Ornik, L. Gomell, S.F. Busch, M. Hermans, and M. Koch, „High quality terahertz wave plate made from glass," in EOS Topical Meeting on Terahertz Science and Technology, (2018).

20. J. Ornik, S. Sommer, R. Gente, M. Koch, J. C. Balzer, K. Fey, and T. Pillich, "THz Spectroscopy Inside a Climate Chamber," in International Conference on Infrared, Millimeter, and Terahertz Waves, IRMMW-THz (IEEE, 2018).

21. Srumika Konde, J. Ornik, J. A. Prume, J. Taiber, and M. Koch, „Inter-study comparison of Nile-Red-based staining protocol for the detection of microplastics in environmental samples," *Microplastics 2018*, (2018).

22. J. Ornik, S. Sommer, M. Weber, C. Lott , J. C. Balzer, S. Gies, and M. Koch, "Detecting Microplastics via Photoluminescence: First Experiments," *Microplastics 2018*, (2018).

23. J. Ornik, D. G. Watson, J. C. Balzer, and M. Koch, "Experimental characterization of dielectric parameter extraction uncertainty for low absorbing liquids using THz TDS," in International Conference on Infrared, Millimeter, and Terahertz Waves, IRMMW-THz (IEEE, 2017).

Wissenschaftlicher Werdegang